

**Mapping Non-lake Thermokarst Landforms on the Tibetan
Plateau Using Remote Sensing and Deep Learning**

HUANG, Lingcao

A Thesis Submitted in Partial Fulfilment
of the Requirements for the Degree of
Doctor of Philosophy
in
Earth and Atmospheric Sciences

The Chinese University of Hong Kong
August 2019

Thesis Assessment Committee

Professor HUI Pak Ming (Chair)

Professor LIU Lin (Thesis Supervisor)

Professor HUANG Bo (Committee Member)

Professor GROSSE Guido (External Examiner)

Abstract of thesis entitled:

Mapping Non-lake Thermokarst Landforms on the Tibetan Plateau Using Remote Sensing and Deep Learning
Submitted by HUANG, Lingcao
for the degree of Doctor of Philosophy
at The Chinese University of Hong Kong in August 2019

Thawing of ice-rich permafrost can result in distinct landforms on the surface, known as thermokarst landforms. The number and extent of thermokarst landforms in permafrost areas have increased in the recent decades. However, their distribution and temporal changes, especially the non-lake ones on the Tibetan Plateau are poorly understood or quantified. This knowledge gap is because (1) most of them are in the remote and inaccessible areas and (2) their diverse characteristics and similarity to the surroundings on satellite images make the automatic mapping extremely challenging.

To map non-lake thermokarst landforms and obtain their distribution on the Tibetan Plateau, I apply geographic object-based image analysis (GEOBIA) and state-of-the-art deep learning algorithms to high-resolution remote sensing images. I innovatively develop a strategy (including delineating training polygons, preparing training images, merging inference results, and polygonising) to utilize deep learning in the processing of remote sensing images. Then I apply the methods to two local studies on the Tibetan Plateau: thermo-erosion gullies on the Eboling Mountain and retrogressive thaw slumps in the Beiluhe region. I utilized images from Google Earth and unmanned aerial vehicle (UAV) images for the Eboling case study, and Planet CubeSat images for the Beiluhe region.

In the Eboling area, the GEOBIA results on UAV and Google images show that this method can detect the locations of these landforms but fails to delineate their boundaries and extents. Moreover, the GEOBIA results contain many false positives, which leads to a low accuracy. In contrast, the method based on a deep learning algorithm (i.e., DeepLab) has much better performance and the mapped boundaries are comparable to manual delineation. It allows us to delineate all the 16 thermo-erosion gullies with an F1 score of 0.74. Further analysis shows that these gullies are narrow and co-located with stream vectors, which implies a strong influence of surface streams on their initiation and development.

In the Beiluhe case study, the deep-learning-based method delineates 196 retrogressive thaw slumps (RTSs), with an F1 score of 0.829. The further analysis shows that (1) most of the RTSs are concentrated in the northwest of the study area with north-facing slopes, (2) these RTSs are small (areas < eight ha and perimeters < 2000 m), and (3) they preferentially developed in the gentle slopes (four to eight degrees) and in areas lower than the surroundings. Multi-temporal images from Google Earth and SPOT-5 satellites show abrupt slope disturbances from 2010 to 2012, which can be attributed to abnormally longer snow-cover periods in winter suggested by MODIS snow products.

In summary, by combining deep learning and remote sensing, I successfully map small and irregular non-lake thermokarst landforms on the Tibetan Plateau. Furthermore, I can extend the method to a large area by collecting corresponding training data and remote sensing images. Products from this study and extended work will improve observations and understanding of permafrost degradation and its environmental and socio-economic impacts.

摘要

富冰多年凍土退化，會在地表上形成一些獨特地貌，即熱喀斯特地貌。近些年調查研究顯示，熱喀斯特地貌的數量和範圍呈現增加的趨勢。然而，在青藏高原上，人們對這些地貌的空間分佈以及時間變化知之甚少，尤其是其中的非湖泊類型熱喀斯特地貌。主要原因有（1）這些地貌分佈在遙遠、人類難以到達的地區；（2）它們的特徵多樣性以及與周圍環境的相似性，使得在衛星影像上對它們進行自動提取非常困難。

為了自動提取青藏高原上非湖泊類型熱喀斯特地貌，並且分析它們的空間分佈特徵，本文以高分辨率遙感影像為輸入，分別嘗試了面向對象影像分析和最新的深度學習算法。本文創新性地提出一種影像處理策略，使得能夠將深度學習算法應用到遙感影像上。該策略包含訓練多邊形選取，準備訓練數據，合併推斷結果以及柵格矢量化等步驟。為了對算法進行驗證，本文選取青藏高原上的俄博嶺和北麓河兩個區域。在俄博嶺，採用了谷歌地球和無人機的影像，在北麓河地區，則使用了Planet微小衛星獲取的影像。

在俄博嶺地區，主要的非湖泊類型熱喀斯特地貌是熱侵蝕溝。面向對象影像分析的方法在谷歌地球影像和無人機影像上都能檢測到熱侵蝕溝的位置，但無法獲取完整的邊界。基於深度學習的方法具有良好的性能，不僅能提取熱侵蝕溝的邊界，而且提取結果與實地測量的非常接近。該方法成功提取了研究區域內16個熱侵蝕溝的邊界，精度（F1 score）為0.74。進一步的分析顯示，這些熱侵蝕溝形狀狹窄，空間分佈與地表徑流有很大的相關性，說明地表徑流對熱侵蝕溝的形成和發展具有一定的影響。

在北麓河地區，主要的非湖泊類型熱喀斯特地貌是後退型熱融滑塌和活動層邊坡坍塌。基於深度學習的方法，成功自動提取了196個後退型熱融滑塌的邊界，其精度（F1 score）為0.83。進一步的分析表明，大部分的地貌分佈在研究區域的西北部、朝北的斜坡上，而且坡度較緩（大部分在4到8度）；覆蓋面積較小：大部分面積小於8公頃，週長小於2000米；並且形成於比周邊低的位置。基於谷歌地球以及SPOT-5衛星的多時相的影像分析表明，該地區在2010到2012年之間，有密集的非

湖泊類型熱喀斯特地貌發展活動。基於MODIS積雪產品的分析表明，可能誘發因素是2008到2011年之間冬季積雪異常偏多。

總體而言，本文提出基於深度學習的地貌提取算法，能夠在高分辨率遙感影像上自動提取面積小、形狀不規則的非湖泊類型熱喀斯特地貌。對於更大的研究區域，如果有訓練數據和高分辨率遙感影像，本文的方法同樣適用。本文提取的結果以及其他區域的應用，將有效增強多年凍土退化的觀測，提升多年凍土退化對環境、社會經濟影響的理解。

Acknowledgement

Throughout my PhD study and completing this dissertation, I have received a lot of support and guidance. First, I am profoundly grateful to my advisor, Lin LIU. Without your encouragement, support, and guidance, this dissertation would not have been possible. I joined Lin's group as a research assistant in 2015 when I had been an employee in Xiamen for two years. With Lin's encouragement and support, then I started pursuing my PhD in Earth science. It was a delightful and fulfilling period working with Lin, applying cutting edge algorithms to address unanswered questions on the Tibetan Plateau.

I want to thank the committee members of my dissertation: Pak Ming HUI, Bo HUANG, and Guido GROSSE for generously offering your time to review this document and serving as examiners in my oral defense. Your support, constructive as well as insightful comments, and invaluable suggestions make this dissertation better.

I have received much help from many collaborators, especially those offer support and help during the fieldwork on the Tibetan Plateau. Thanks Liming Jiang and his group member: Zhiwei Zhou, Yafei Sun, Dewei Li, and Daan Li, Linlin Liang, Yuxing Chen in Institute of Geodesy and Geophysics, Chinese Academy of Sciences for collaboration and collecting data on Eboling Mountain. Thanks Tingjun Zhang and his group members including Wanwan Shao, Wen Zhong, Cuicui Mu, GuanXin Wang, Wen Sun, and Chengyan Fan at Lanzhou University for discussion, suggestions and support during the fieldwork on Eboling Mountain. I would like to thanks Jing Luo, Zhanju Lin, and Fujun Niu in Northwest Institute of Eco-Environment and Resources, Chi-

nese Academy of Sciences for their collaboration and support in the Beiluhe fieldwork. Thanks Simon Gascoin in France for collecting the SPOT-5 images, and Ingmar Nitze as well as Frank Guenther at Alfred Wegener Institute Helmholtz Centre for Polar and Marine Research, for discussion on mapping permafrost disturbances using remote sensing. I also would like to thanks Thian Yew Gan for hosting my visit to University of Alberta for six months. I gained many insight and knowledge in the discussion with you as well as your lectures, which may benefit my research in the future.

There were many happy and memorable moments during the journey of pursuing my PhD. Thanks my group mates: Enze Zhang, Yan Hu, Jie Chen, Xiyu Chen, and Jiahua Zhang for the support and help. Thanks for the friendships with many EASC members, including Fanbao Meng, Mac SADEKE, Lang Wang, Guoyan Jiang, Jilong Chen, Alan LIM, Roc Wang, Xiang Chen, Han Chen, Shirley Liu, Suli Yao, Pengcheng Zhou, Gaohua Zhu, and others. Thanks teaching staffs at ESSC for broadening my view in Earth and Atmospheric Sciences, especially Teng-fong Wong, for involving me in a rock physics project, which is quite interesting. Also thanks Eric, Sally, Joyce, Elaine, and Siulam for the help. The time of playing badminton is the most enjoyable moment, I would like to thanks many players at CUHK and in Edmonton for that.

I am grateful to my parents. My dad and mom always give me the freedom to explore what I am interested in. Their support means a lot to me.

Contents

Abstract	i
摘要	iii
Acknowledgement	v
1 Introduction	1
1.1 Background	1
1.1.1 Permafrost and its spatial distribution	1
1.1.2 Permafrost warming and degradation	2
1.1.3 Thermokarst landforms	3
1.2 Motivation	5
1.3 Objectives	7
1.4 Road map of dissertation	7
1.5 Innovative merits and potential impacts	8
2 Mapping Thermo-Erosion Gullies Using Geographic Object-Based Image Analysis	10
2.1 Introduction	11
2.2 Materials and methods	12
2.2.1 Study area and high-resolution imagery	12
2.2.2 Methods	15

2.3	Results	21
2.4	Discussion	24
2.4.1	Factors that influence gully detection	24
2.4.2	Technical challenges of GEOBIA	25
2.4.3	Erroneous features from the ground truth	26
2.4.4	Future work	26
2.5	Summary	27
3	Mapping Thermo-Erosion Gullies Using Deep Learning	29
3.1	Introduction	30
3.2	Study area	30
3.3	Methods	32
3.3.1	Collection of UAV images and creation of digital orthophoto map	32
3.3.2	Collection of ground truth polygons	34
3.3.3	Preparation of training data	34
3.3.4	Mapping of thermo-erosion gullies using DeepLab	41
3.3.5	Post-processing	42
3.3.6	Validation	42
3.4	Results	43
3.5	Discussion	48
3.5.1	Spatial distribution of the thermo-erosion gullies	48
3.5.2	Delineation accuracies of the true positives	49
3.5.3	Possible causes of false positives	49
3.5.4	Mapping of thermo-erosion gullies on the UAV-based DEM	50
3.5.5	Advantages and limitations of deep learning for mapping thermokarst landforms	50
3.5.6	Prospects and future work for mapping thermokarst landforms in a large area	54

3.6	Summary	54
4	Mapping Retrogressive Thaw Slumps in Beiluhe Using Deep Learning	56
4.1	Introduction	56
4.2	Study area	59
4.3	Methods	60
4.3.1	Collection and pre-processing of Planet images	60
4.3.2	Collection of ground truth polygons	61
4.3.3	Automatic mapping of RTSs	62
4.3.4	Quantification of RTS characteristics and terrain factors	68
4.4	Performance of the automatic mapping method	69
4.4.1	Robustness of the method	69
4.4.2	Mapped polygons and their accuracies	70
4.4.3	Improvement due to data augmentation	72
4.4.4	Other combinations of the four bands of Planet images	77
4.4.5	Factors affecting the accuracies	78
4.5	Characteristics of RTSs and their terrain factors	81
4.5.1	Geometric characteristics of RTSs	81
4.5.2	Terrain factors of RTSs	82
4.5.3	Spatial distribution and the terrain controlling factors	85
4.6	Discussion	87
4.6.1	Advantages and limitations of using Planet CubeSat images . .	87
4.6.2	Advantages and limitations of the automatic mapping method for RTSs	88
4.6.3	Comparison between the mapped polygons and ground truths .	89
4.6.4	Future work	90
4.7	Summary	91

5 Temporal Changes of Active Layer Detachments and Retrogressive Thaw Slumps in Beiluhe	92
5.1 Introduction	92
5.2 Data and methods	94
5.2.1 Study area	94
5.2.2 Collecting and processing remote sensing images	95
5.2.3 Identifying the development of RTSs	97
5.2.4 MODIS snow cover products and meteorological data	97
5.3 Preliminary results	98
5.4 Summary and future work	101
6 Conclusions	103
6.1 Summary and conclusions	103
6.2 Future directions	104
Bibliography	106
A Supplementary tables for Chapter 4	124
B Glossary of abbreviations	130

List of Figures

1.1	Schematic picture of permafrost thermal regime. The blue and red lines show the minimum and maximum ground temperature during the year, respectively. The circle shows the shallowest depth where annual amplitude of ground temperature is negligible (French, 2017; Biskaborn et al., 2019).	2
1.2	Permafrost map on the Tibetan Plateau (Zou et al., 2017). The red points and stars indicate three cities and two study areas, respectively.	3
1.3	Ground photos of thermokarst landforms on the Tibetan Plateau. (a)–(c) are an active layer detachment, retrogressive thaw slump, and thermo-erosion gully, respectively.	4
2.1	Study area and location: (a) is the Google image of our study area. The yellow polygon denotes the extent of Figure 2.2 and 2.6. The black polygon is a gully boundary we outlined in the field in July 2016. The red star in (b) indicates the location of our study area in the northeastern Tibetan Plateau. (c) is a ground photo of a fraction of the thermo-erosion gully, marked by the black polygon in (a).	13

2.2	The Digital Orthophoto Map (DOM) and a subset of the Google image. (a) is the DOM constructed from the UAV images. The yellow rectangle denotes the extent of Figure 2.4. (b) is a subset of the Google image with the same extent of (a). The yellow circle marks a gully that will be discussed in Section 2.4.1	14
2.3	Flowchart of our GEOBIA method for gully detection.	16
2.4	Examples of intermediate and final results of our GEOBIA method: (a) is a patch of the DOM; (b) shows the segmentation results. The white polygons denote the segmented image objects; (c) shows the edge features; (d) shows the pixel shape index (PSI) (see more in the text). A brighter color means a greater PSI value. (e) shows the classified gully and non-gully objects with red and white polygons, respectively; (f) shows the final detection results. Only the gully polygons are kept.	17
2.5	(a) Thermo-erosion gullies detected from the Google image: the red poly- gons are true detections; the white polygons are false detections; the ground truth polygons are outlined in black. (b) and (c) show the two ground truth polygons that we failed to detect from the Google image. (d) is an example of the true detection.	22
2.6	Detection results using the DOM (a) and the subset of the Google image (b). The red polygons are true detections; the white polygons are false detections; the ground truth polygons are outlined in black. The yellow circle marks a false detection that we will discuss in Section 2.4.1.	23

3.1	Digital Orthophoto Map (DOM) of the study area. The white polygons are the ground truth polygons. The red triangles and yellow uppercase letters indicate the positions and the names of ground photos shown in Figure 3.2, respectively. The black rectangles with lowercase letters indicate the extents of the DOM subsets shown in Figure 3.5. The red star in the inset shows the location of our study area on the Tibetan Plateau.	31
3.2	Ground photos (a–d); and their corresponding DOMs (e–h) of different land covers or landforms in the study area. In (e–h), the red triangles indicate the camera positions and the yellow arrows indicate the looking directions.	31
3.3	Map of the ground truth polygons and their obtaining methods. Nine of them were collected in the field using GPS Real-Time Kinematic. Seven of them were manually delineated (digitizing) on the DOM.	35
3.4	Distribution of the training polygons: 15 of them are non-gullies; seven were collected from field GPS measurements; and four were from manual delineation (digitizing).	36
3.5	Examples of the DOM subsets used for training: (a,d) examples of sub-images containing non-gully land covers; (b,c) examples of sub-images containing gullies; and (a-L–d-L) their corresponding label images. The white pixels in (a-L–d-L) indicate gullies, while non-gully pixels appear as light blue. A label image appears entirely light blue (e.g., (a-L,d-L)) if the corresponding sub-image does not contain a gully.	37
3.6	Flowchart of our mapping method based on DeepLab.	38

3.7	The grid for subdividing a sub-image (same as Figure 3.5c). The yellow number in each black square is the ID of the subdivided image patch. The yellow square is an example showing how we extend the boundary of a subdivided image patch (#8) from the black square to the yellow square. The yellow arrows in #52 and #27 indicate the patch width and height, respectively.	40
3.8	Data augmentation: (a) the patch marked by the yellow square in Figure 3.7; and (b–d) the patches after blurring, flipping left and right, and rotating 90° clockwise, respectively.	40
3.9	Distribution of the mapped gully polygons (the red and yellow ones are true and false positives, respectively). The blue lines are the simulated surface streams (see Section 3.5.1). The boxes (a)–(d) denote the extents of the subfigures in Figure 3.10.	44
3.10	Zoomed-in comparisons between the gully polygons (red) and ground truth polygons (white). The yellow ones are false positives (same as in Figure 3.9). The extents of (a)–(d) are marked in Figure 3.9. See more discussion in Sections 3.5.2 and 3.5.3.	45
3.11	Topographical statistics of the mapped thermo-erosion gullies. (a) and (b) are statistics of mean elevation and mean slope, respectively.	47
3.12	Geometric statistics of the mapped thermo-erosion gullies. (a), (b), and (c) are statistics of circularity, area, and perimeter, respectively.	47
3.13	Scatter plot between the IOU values of the mapped gullies (the true positives) and their areas.	48
3.14	Distribution of mapped gully polygons (the red and yellow ones are true and false positives, respectively) solely using the UAV-based digital elevation model.	51

3.15 Comparison between the DeepLab-based results and those obtained from a supervised classification using support vector machine (SVM), which is a key step of GEOBIA described in Chapter 2. The mapped gullies are marked by filled red polygons on all sub-figures. (a) and (c) are the results of SVM, which contain numerous false positives. (b) and (d) are the results of DeepLab, which only contain a few false positives. The white boundary in (c) and (d) is a ground truth polygon.	53
4.1 The ground photo (a) and Planet image (b) of a retrogressive thaw slump (RTS) whose central location is 92.912 °E, 34.848 °N. In (b), the black polygon outlines the RTS, the yellow arrow indicates the facing direction of the ground photo, and the inset shows the location of our study area on the Tibetan Plateau.	60
4.2 Flowchart of the automatic mapping method based on deep learning algorithms.	62
4.3 Distribution and extent of training polygons and sub-images. The red and yellow polygons are positive and negative training polygons, respectively. The red and yellow rectangles with dot lines are the corresponding sub-images. (a) and (b) are the zoom in of two small areas marked on the main figure.	64
4.4 The mosaic of positive sub-images which are derived from positive training polygons.	65
4.5 The mosaic of negative sub-images which are derived from negative training polygons.	66
4.6 Precision-recall curves of the top five average precision (AP) in experiments of data augmentation (labeled as “imgAugX”, where X is the experiment number).	72

4.7	Precision-recall curves of five repeating tests applying 5-fold cross-validation. (labeled as “5fold_X_tY”, indicating that the #Y experiment with the Xth fold as validation data).	73
4.8	Precision-recall curves of five repeating tests applying 10-fold cross-validation. (labeled as “10fold_X_tY”, indicating that the #Y experiment with the Xth fold as validation data).	74
4.9	IOU histogram of the mapped polygons in experiment #16.	75
4.10	Automatically mapped retrogressive thaw slumps (red polygons) versus manual delineation (black polygons) on Planet images. The red polygons are true positives of the mapped polygons in Experiment #16. (a)–(c) are extents of the figures in Figure 4.11. The grey gap is due to the lack of Planet scenes.	75
4.11	Amplifications of mapping results. (a)–(c) are amplifications of three regions marked by black rectangles in Figure 4.10. The two rectangles marked are discussed in sections 4.4.2 and 4.6.2.	76
4.12	Scatter plot between the IOU values and areas of the mapped polygons (the true and false positives) based on experiment #16.	79
4.13	Scatter plot between the IOU values and perimeters of the mapped poly-gons (the true and false positives) based on experiment #16.	79
4.14	Scatter plot between the IOU values and circularities of the mapped polygons (the true and false positives) based on experiment #16. . . .	80
4.15	Scatter plot between the IOU values of the mapped polygons (the true and false positives) based on experiment #16 and the corresponding count of adjacent RTSs.	80
4.16	Geometric statistics of the RTSs based on mapped RTSs of experiment #16 in Table 4.1. One RTS whose area is 34.6 ha not shown in (a), and two RTSs, whose perimeters are 6924 meters and 8226 meters, respec-tively, are not shown in (b) because they are out of range.	82

4.17 Geometric statistics of the RTSs based on manual delineation (i.e., ground truths)	82
4.18 Statistics of RTS terrain factors based on automatic mapping results (#16 in Table 4.1). Landscape refers to the entire study area.	83
4.19 Statistics of RTS terrain factors based on manual delineation (i.e., ground truths)	84
4.20 DEM and RTSs in the study area.	86
5.1 The red rectangle and triangle indicate the extent of our study area and the location of the nearest meteorological station (93.083°E, 35.217°N), respectively. The background is the Google image. The yellow rectangle and circle indicate the extent of Figure 5.2 and a lake that will be discussed in section 5.3, respectively.	94
5.2 The comparison between Google images acquired on 2010-03-27 and 2012-11-16 shows that abrupt changes of non-lake thermokarst landforms. The red arrow indicates the headwall shadow. (c) and (d) zoom into the blue boxes in (a) and (b), respectively.	96
5.3 ALDs and RTSs in the study area. The red and blue polygons are RTS boundaries delineated using the 2012 Google image and ALD boundaries derived from the 2010 Google image, respectively. (a) and (b) show these boundaries on a hillshade image and on the 2012 Google image, respectively. The extent of (b) is marked by the yellow rectangle in (a).	99
5.4 Mean daily air temperature at the meteorological station (as shown in Figure 5.1) from 2002 to 2012.	100
5.5 Annual and monthly precipitation at the meteorological station (as shown in Figure 5.1) from 2002 to 2012.	100

5.6 Seasonal snow cover days from 2002 to 2012. The hot spot in the north-eastern of the study area is due to the misclassification of a lake (marked by the yellow circle in Figure 5.1) in MODIS snow products. 102

List of Tables

3.1	Parameters and settings of the Trimble Inpho UASmaster software for producing the digital elevation model and digital orthophoto map	33
3.2	Delineation accuracies obtained with different IOU thresholds	44
3.3	Accuracies of experiments using varying combinations of training polygons. .	46
4.1	Selected experiments of data augmentations: without data augmentation (#0), the top five (#16, 4, 2, 13, and 6) and bottom five (#24, 9, 23, 25, and 20) based on AP	71
4.2	Statistics of accuracies based on different data augmentation methods. .	77
4.3	Accuracies of other band combinations.	78
5.1	List of high-resolution images in the order of acquisition dates	95
5.2	The number of RTS initiation in different years	98
5.3	The number of RTS development in different years.	99
A.1	Accuracies of the mapping results with different data augmentation methods. Options refer to Augmentation Methods. The meaning of each column is described in Table 4.1.	124
A.2	Accuracies of the mapping results without removing small polygons by applying different data augmentation methods. Options refer to Augmentation Methods. The meaning of each column is described in Table 4.1.	127

Chapter 1

Introduction

1.1 Background

1.1.1 Permafrost and its spatial distribution

Defined based on temperature, permafrost refers to the ground at or below 0 °C for two or more consecutive years (French, 2017). As shown in Figure 1.1, the layer above permafrost that thaws in summer and freezes in winter is called the active layer. Thickness of active layer ranges from a few decimeters to several meters depending on controls such as ambient air temperature, topography, vegetation, snow cover, soil/rock type, and water content (French, 2017). Permafrost is a combination of soil, rock, sediment, and ground ice. Among these, ground ice is common but not always present. In particular, the permafrost containing excess ice (the ice volume exceeds the total pore volume of the natural unfrozen ground) is known as ice-rich permafrost. The thickness of permafrost can range from a few meters to around one thousand meters (French, 2017). On the Tibetan Plateau, permafrost is shallow (thinner than 100 m) and warm (higher than –2 °C) (Zhou et al., 2000; Wu et al., 2010).

Permafrost areas occupy about 22% to 25% of the exposed land of the Northern Hemisphere (Brown et al., 1997; Obu et al., 2019). Most permafrost is in high latitude or elevation regions: about 70% of permafrost is distributed between 45° N and 67° N

and $\sim 10\%$ occurs above 3000 m a.s.l. (Zhang et al., 1999). As shown in Figure 1.2, permafrost on the Tibetan Plateau occurs over a total area of $1.06 \times 10^6 \text{ km}^2$ or 40% of the plateau's area (Ran et al., 2012; Zou et al., 2017).

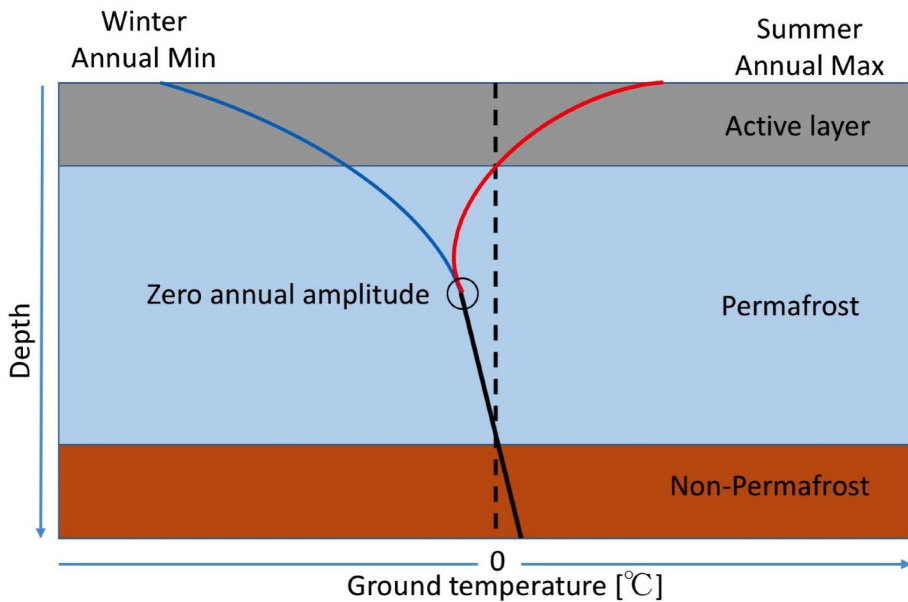


Figure 1.1: Schematic picture of permafrost thermal regime. The blue and red lines show the minimum and maximum ground temperature during the year, respectively. The circle shows the shallowest depth where annual amplitude of ground temperature is negligible (French, 2017; Biskaborn et al., 2019).

1.1.2 Permafrost warming and degradation

Field measurements have revealed that permafrost is warming globally. From 2007 to 2016, global permafrost temperature near the depth of zero annual amplitude increased by $0.29 \pm 0.12 \text{ }^\circ\text{C}$ (Biskaborn et al., 2019). Along the Qinghai-Tibetan Highway, an average increase of permafrost temperature at 6.0 m depth by $\sim 0.43 \text{ }^\circ\text{C}$ from 1996 to 2006 was recorded (Wu and Zhang, 2008). Permafrost warming is mainly attributed to air temperature increase in the Northern Hemisphere. Moreover, increase of snow thickness and cover days in winter also contributes to the warming, especially in mountain areas (Ling and Zhang, 2003; Wu and Zhang, 2008; Ran et al., 2018; Biskaborn et al., 2019). Human activities and natural disturbances, such as building infrastruc-

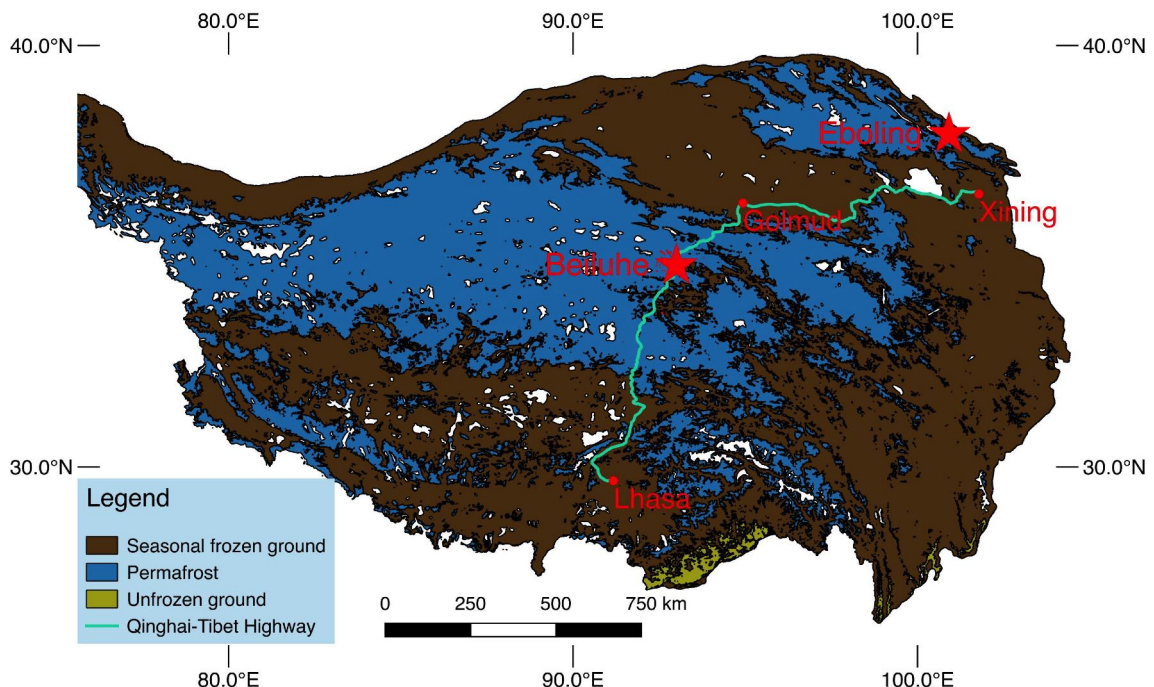


Figure 1.2: Permafrost map on the Tibetan Plateau (Zou et al., 2017). The red points and stars indicate three cities and two study areas, respectively.

ture, removing vegetation cover, and fires, also lead to the warming of permafrost in a local area (Jin et al., 2000; Tchebakova et al., 2009; Niu et al., 2015).

Due to warming, permafrost undergoes degradation, manifested in active layer deepening, thinning of permafrost thickness, disappearance of sporadic permafrost, and formation of thermokarst landforms (Czudek and Demek, 1970; Jorgenson and Osterkamp, 2005; Osterkamp, 2007; Åkerman and Johansson, 2008; Zhao et al., 2010). Furthermore, permafrost degradation can cause damage to infrastructure, release greenhouse gases from decayed carbon stored in permafrost, and significantly alter the local ecosystem (Tong and Wu, 1996; Yang et al., 2010; Bowden, 2010; Grosse et al., 2011; Vonk et al., 2015; Schuur et al., 2015; Olefeldt et al., 2016; Schuster et al., 2018; Hjort et al., 2018). Permafrost also contains a significant amount of mercury (Schuster et al., 2018) which may break the balance of mercury cycle in the biosphere as permafrost continues to degrade.

1.1.3 Thermokarst landforms

Melting of ground ice in ice-rich permafrost can lead to irregular and depressed topography, known as thermokarst landforms (Czudek and Demek, 1970; Jorgenson et al., 2006; Osterkamp, 2007). More than 20 kinds of thermokarst landforms (such as thermokarst lakes, thermo-erosion gullies, active layer detachments, and retrogressive thaw slumps) are identified in permafrost areas (Jorgenson, 2013). As examples, three of them on the Tibetan Plateau are shown in Figure 1.3.

Thermokarst processes are associated with abrupt permafrost degradation and would strongly affect the local environment. Compared with top-down thawing of permafrost, which is a gradual process taking a few thousand years (French, 2017), thermokarst can happen in a few hours or years. Formation of thermokarst lakes and thermo-erosion gullies can significantly change the local hydrology (Smith et al., 2005; Andresen and Lougheed, 2015; Godin et al., 2014). Frozen carbon and mercury would be released to the atmosphere and downstream via development of thermokarst landforms (Serikova et al., 2019; Pierre et al., 2018).

Thermokarst landforms are widespread in permafrost areas but are localized disturbances on the surface. According to an estimation, thermokarst landforms occur in $\sim 20\%$ northern circumpolar permafrost areas (Olefeldt et al., 2016). Many studies also have shown that the number of thermokarst landforms increased in recent decades (Jorgenson et al., 2006; Krieger, 2012; Luo et al., 2015; Patton et al., 2019; Jones et al., 2019; Lewkowicz and Way, 2019). The development of thermokarst landforms is related to controlling factors including ice content, topography, hydrology, vegetation, precipitation, and soil type. However, these factors vary spatially, which leads to the isolated distribution of thermokarst landforms (Jorgenson, 2013).

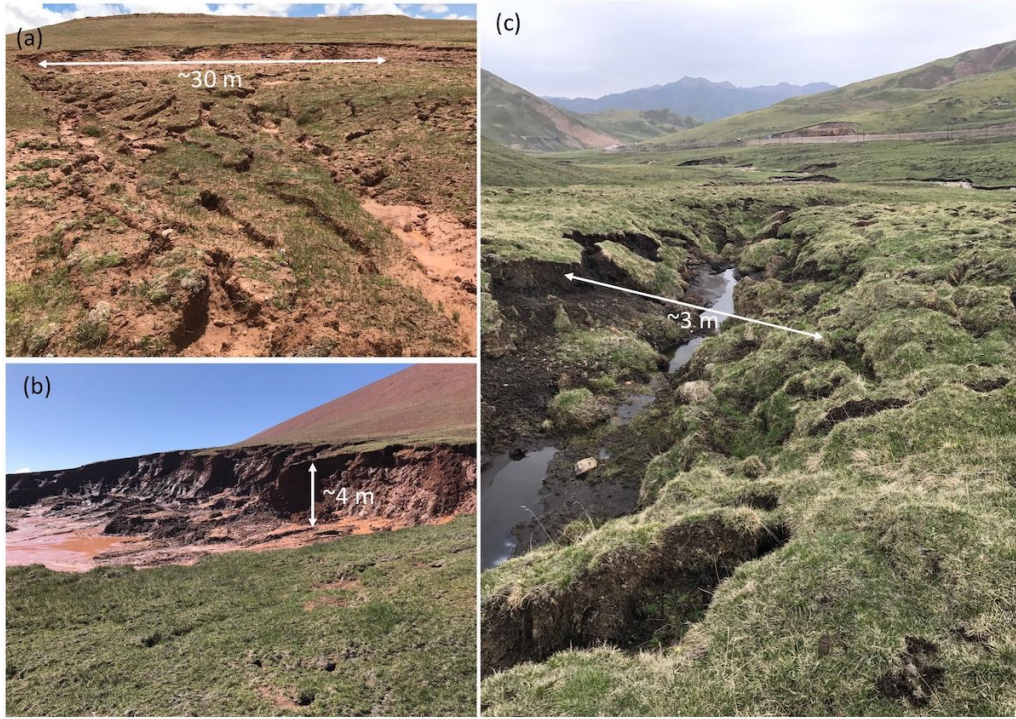


Figure 1.3: Ground photos of thermokarst landforms on the Tibetan Plateau. (a)–(c) are an active layer detachment, retrogressive thaw slump, and thermo-erosion gully, respectively.

1.2 Motivation

The spatial distribution of thermokarst landforms is essential for understanding permafrost degradation and the corresponding impacts. However, large portions of thermokarst landforms remain unmapped because (1) they spread in remote and inaccessible areas and (2) their diverse characteristics and similarity to the surroundings on remote sensing images make the mapping of them challenging.

Various methods, including mapping in the field, manual delineation on remote sensing images, and automatic mapping on images, have been used to map thermokarst landforms. Mapping in the field using Global Positioning System (GPS) or other geodetic instruments is prevalent when studies focused on specific landforms in a local area. For instance, Niu et al. (2012) mapped a thaw slump in the field and analyzed its evolution over ten years; Lin et al. (2011) identified a gully in the field and monitored

its influence on roadbeds; Fortier et al. (2007) mapped many thermo-erosion gullies on Bylot Island in northern Canada using GPS. Manual delineation on remote sensing images enables us to map thermokarst landforms in remote and inaccessible areas, and was used in many studies (e.g., Godin and Fortier, 2012; Luo et al., 2015; Niu et al., 2016; Ramage et al., 2017). However, these two methods are labor-intensive and limited to local study areas. Automatic mapping is necessary for mapping thermokarst landforms in a large scale such as the Tibetan Plateau. An automatic processing chain for Landsat images has been developed for mapping permafrost disturbances and applied to the Arctic and subarctic regions (Nitze and Grosse, 2016; Nitze et al., 2017, 2018). However, many thermokarst landforms with small areas may be missed in these results due to the low spatial resolution (30 m) of Landsat images. A few studies used high spatial resolution (< 5 m) remote sensing images to automatically identify thermokarst landforms (Belshe et al., 2013; Rudy et al., 2013), but these targeted at small areas, and the results contain noise. The only study to date on thermokarst landforms at the circumpolar scale was conducted by Olefeldt et al., 2016, but it is an empirical estimation instead of real observation.

On the Tibetan Plateau, there are much fewer studies on thermokarst landforms compared with those in the Arctic and subarctic regions. Several studies focused on individual landforms such as thermo-erosion gullies (Mu et al., 2016b; Liu et al., 2018), thermokarst lakes (Lin et al., 2010), and retrogressive thaw slumps (Niu et al., 2012). A few studies investigated thermokarst lakes or retrogressive thaw slumps in regions along the Qinghai-Tibet Highway (Niu et al., 2014, 2016; Luo et al., 2015; Wang et al., 2017). A large portion of permafrost areas on the Tibetan Plateau remains unmapped.

Compared with thermokarst lakes, non-lake thermokarst landforms, such as retrogressive thaw slumps, thermo-erosion gullies, and active layer detachments, are difficult to automatically delineate on remote sensing images. A non-lake thermokarst landform consists of many parts, and each part has different spectral characteristics due to various land covers such as exposed soil, vegetation, and water-bodies. Moreover, some parts

of a non-lake thermokarst landform are similar to its surroundings, which impedes easy delineation and leads to many false results. The shape and size of non-lake thermokarst landforms also post a challenge for automatic mapping. The shape of a thermo-erosion gully is narrow: its narrowest parts could be only a few meters and difficult to be identified on remote sensing images. Usually, the size of a non-lake thermokarst landform is small (a few hectares or less), and it only shows up on high spatial resolution (< five meters) images. The use of high-resolution images increases the heterogeneity inside non-lake thermokarst landforms.

The accumulation of high-resolution remote sensing images and development of deep learning technology in recent years make it possible to automatically map non-lake thermokarst landforms in large areas. As remote sensing sensors in space become sharper after each generation, the spatial resolution of satellite images increases continuously. The satellite images with the finest spatial resolution (~ 0.5 m) available to the public are sourced from WorldView satellites. Some airborne images can have higher resolution (~ 0.1 m) but their coverages are smaller compared to satellite images and limited to accessible areas. The images from Planet CubeSats, with spatial resolutions of three to five meters, fully cover the global earth surface everyday. These high-resolution images allow us to investigate many small, irregular, and subtle non-lake thermokarst landforms in permafrost areas. Deep learning algorithms have been widely used in many complex scenarios and achieved unprecedented results (e.g., Krizhevsky et al., 2012; LeCun et al., 2015; Silver et al., 2017). In remote sensing applications, deep learning has also achieved outstanding results in poverty estimation, land cover mapping, object detection, and delineation of ice-wedge polygons (Jean et al., 2016; Huang et al., 2018a; Guo et al., 2018; Zhang et al., 2018). By applying deep learning algorithms to high-resolution images, I can delineate boundaries of non-lake thermokarst landforms. Moreover, their boundaries are crucial to quantify the area and temporal changes of non-lake thermokarst landforms.

1.3 Objectives

To provide an effective approach to mapping non-lake thermokarst landforms at local and large scales, I apply cutting-edge algorithms to high-resolution images and conduct two case studies on the Tibetan Plateau. Specifically, the objectives include:

- (1) apply Geographic Object-Based Image Analysis (GEOBIA), which is a commonly-used mapping method for high-resolution images, to high-resolution images cover Eboling;
- (2) apply state-of-the-art deep learning algorithms to images over Eboling and Beiluhe;
- (3) quantify the terrain factors and geometric variables of non-lake thermokarst landforms in Eboling and Beiluhe;
- (4) quantify and investigate temporal changes of retrogressive thaw slumps in Beiluhe.

1.4 Road map of dissertation

In this dissertation, GEOBIA was first applied to high-resolution images cover Eboling because it is commonly-used and outperforms many pixel-based methods (Chapter 2). This method can identify locations of thermo-erosion gullies in Eboling area, but it failed to delineate boundaries of these landforms and contained numerous false results due to their complex characteristics and the intrinsic limitations of the GEOBIA. To accurately delineate non-lake thermokarst landforms, I apply deep learning algorithms to the same gullies on Eboling Mountain (Chapter 3). The results derived from deep learning algorithms well match the boundaries measured in the field. To extend the study area and map other non-lake thermokarst landforms, I also apply deep learning algorithms to high-resolution images covering Beiluhe, where many retrogressive thaw slumps developed (Chapter 4). In Chapter 3 and 4, I also present the geometric characteristics and terrains of non-lake thermokarst landforms in Eboling and Beiluhe, which may provide useful information for other researches. Finally, to understand their

development, I quantify the development of retrogressive thaw slumps in Beiluhe and present the preliminary results in Chapter 5.

1.5 Innovative merits and potential impacts

The quantity of thermokarst landforms increases in recent decades due to global warming. Many thermokarst landforms, especially non-lake ones on the Tibetan Plateau, remain unmapped. To obtain the spatial distribution of non-lake thermokarst landforms, I propose mapping methods based on GEOBIA and deep learning, then apply them to two areas on the Tibetan Plateau. This is the first study to automatically map non-lake thermokarst landforms on the Tibetan Plateau. It will provide an approach to bridge the gap between local and large scale studies of non-lake thermokarst landforms.

This dissertation develops a new application of cutting-edge deep learning algorithms. I propose a mapping method including a strategy for image pre-processing and post-processing, which allows us to utilize the outstanding performance of deep learning. The effectiveness and transferable nature of deep learning ensure that the method can be potentially applied to other, large areas, even other landforms in non-permafrost areas and be a basis for regular monitoring. The codes and trained neural networks are published on Github (github.com/yghlc), which will benefit scientists and engineers in cryosphere, remote sensing, and geomorphology communities.

Inventories of thermo-erosion gullies and retrogressive thaw slumps in two areas on the Tibetan Plateau provide new insights into the regional spatial distributions and characteristics of these landforms. They will also provide a baseline dataset for further studies of permafrost degradation and assessing the risks due to thermokarst development. Quantitative assessment of the temporal changes of retrogressive thaw slumps in Beiluhe is the first regional study on their evolution on the Tibetan Plateau, which can advance the understanding regarding their formation and development.

□ End of chapter.

Chapter 2

Mapping Thermo-Erosion Gullies Using Geographic Object-Based Image Analysis

This chapter focuses on mapping thermo-erosion gullies in Eboling using Geographic Object-Based Image Analysis (GEOBIA). Thermo-erosion gullies are one kind of thermokarst landforms widespread in permafrost areas, but most of them are small and irregular in remote and inaccessible areas. Detecting the locations of thermo-erosion gullies is the first step to monitoring them. Here, GEOBIA was applied to the high-resolution images covering Eboling in the northeastern Tibetan Plateau, aiming to automatically detect thermo-erosion gullies from these images. Validating against the field observations, the locations of 90% of thermo-erosion gullies in the study area were correctly detected. This case study demonstrates that GEOBIA can automatically detect the location of most thermo-erosion gullies from high-resolution remote sensing images. However, due to the limitations of GEOBIA including the challenges of image segmentation and empirical setting of parameters, the results contain many false results, and it is difficult to extend to other or larger areas. Therefore, I utilize other promising methods such as deep learning algorithms in the next chapter.

2.1 Introduction

A thermo-erosion gully is a kind of thermokarst landform (Kokelj and Jorgenson, 2013). The heat exchange between permafrost and the surface or water results in the melting of ground ice, then causes the formation of gullies. For example, surface and subsurface water (from run-off and local melting), controlled by the topographic gradient and ice-wedge polygon network, flowed along specific directions and resulted in the gully landscapes (Fortier et al., 2007). The formation of a thermo-erosion gully is dominated by heat transfer. By contrast, in non-permafrost regions, mechanical erosion (running water sharply erodes into the soil) dominates the development of gullies. That is why the term “thermo-erosion gully” is used for describing the gully landform in permafrost regions (Poesen et al., 2003). Hereafter, “gully” refers to a thermo-erosion gully.

Thermo-erosion gullies play a critical role in ice-rich permafrost degradation. Due to gully formation, ice-rich permafrost is exposed to solar radiation and atmospheric heat. Then a positive feedback (the increase of heat transfer from the environment to the permafrost) expands the gully and accelerates its degradation (Godin and Fortier, 2012). The formation and development of thermo-erosion gullies strongly affect the local environment through interactions between soil texture, slope position, hydrology and vegetation (Niu et al., 2015; Harms et al., 2014; Van Huissteden et al., 2011; Rowland et al., 2010). For example, thermo-erosion gullies increase the export of nitrogen from Arctic tundra to downstream ecosystems (Harms et al., 2014) and have altered the soil properties and carbon emissions in the northern Tibetan Plateau (Mu et al., 2016b).

In this study, we apply GEOBIA to high-resolution images covering Eboling Mountain, Qinghai, China. In recent years, the accumulation of high spatial resolution images provides an unprecedented opportunity for automatically mapping thermo-erosion gullies and studying their spatial-temporal variations. GEOBIA, also termed as OBIA (without “Geographic”) in the literature, is widely-used for land cover classification and urban mapping from high-resolution images (Hay and Castilla, 2008; Blaschke,

2010; Matikainen et al., 2017). Many studies have demonstrated that GEOBIA outperforms pixel-based methods in high-resolution image analysis (Blaschke, 2010; Chen et al., 2012).

The main objective is to develop an automatic GEOBIA algorithm that is specifically for detecting thermo-erosion gullies from both satellite images and aerial photos. To relax the requirement of high-quality source data and computing resources, we only aim to detect the gully locations instead of delineating their boundaries. Employing validation against the field observations, we will show that our GEOBIA algorithm can detect most of the thermo-erosion gullies from high-resolution remote sensing images in the study area. However, the results suffer from some false detections due to limiting factors such as low quality of segmentation and erroneous training data.

The main novelty of this study is that we detected gullies only using RGB remote sensing images. A few studies utilized multi-spectral high-resolution images to identify these landforms (Rudy et al., 2013; Belshe et al., 2013). However, these multi-spectral high-resolution images are typically acquired by commercial satellites and can be expensive. The RGB satellite images we used in this work are freely downloaded from Google Earth. Although they may lose contrast and have lower quality than the commercial images, we will demonstrate their performance for detecting gully locations and discuss their value for large-scale mapping. We also utilized aerial photos collected from our fieldwork and compare their performance with the Google Earth images.

2.2 Materials and methods

2.2.1 Study area and high-resolution imagery

Our study area is located on Eboling Mountain ($100^{\circ} 52' 53''$ E to $100^{\circ} 55' 10''$ E, $37^{\circ} 59' 20''$ N to $38^{\circ} 00' 39''$ N; total area is $\sim 6 \text{ km}^2$), in the upper reaches of the Heihe River basin in the northeastern Tibetan Plateau, Qinghai, China (Figure 2.1a and 2.1b). The mean elevation within the study area is 3600 m a.s.l., and the lowermost permafrost occur-

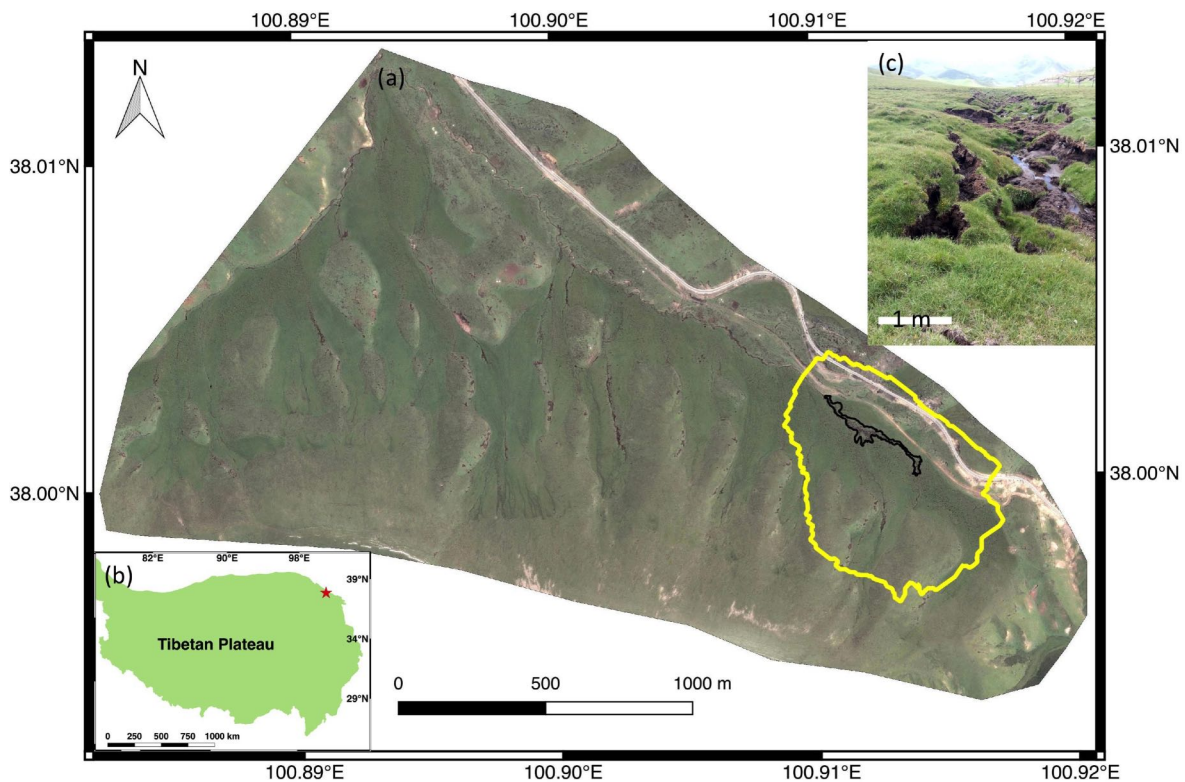


Figure 2.1: Study area and location: (a) is the Google image of our study area. The yellow polygon denotes the extent of Figure 2.2 and 2.6. The black polygon is a gully boundary we outlined in the field in July 2016. The red star in (b) indicates the location of our study area in the northeastern Tibetan Plateau. (c) is a ground photo of a fraction of the thermo-erosion gully, marked by the black polygon in (a).

rence is at 3400 m a.s.l. (Wu et al., 2007). The surface soil is a peat layer that is 0.4–1 m thick (Mu et al., 2015, 2013). The active layer thickness ranges from 0.81 to 2.1 m with a mean of 1.32 m (Cao et al., 2017). The dominant vegetation types are alpine swamp meadow and alpine meadow (Cao et al., 2017; Mu et al., 2016a). Hummocks are common and characterize the microtopography in this region. The mean annual air temperature of this region increased by 0.6–1 °C between 1950 and 2006 (Peng et al., 2013).

Eboling Mountain is underlain by ice-rich permafrost. The study area contains numerous well-developed thermo-erosion gullies (Figure 2.1a and 2.1c). Their lengths range from a few meters to several kilometers, and their widths range from less than

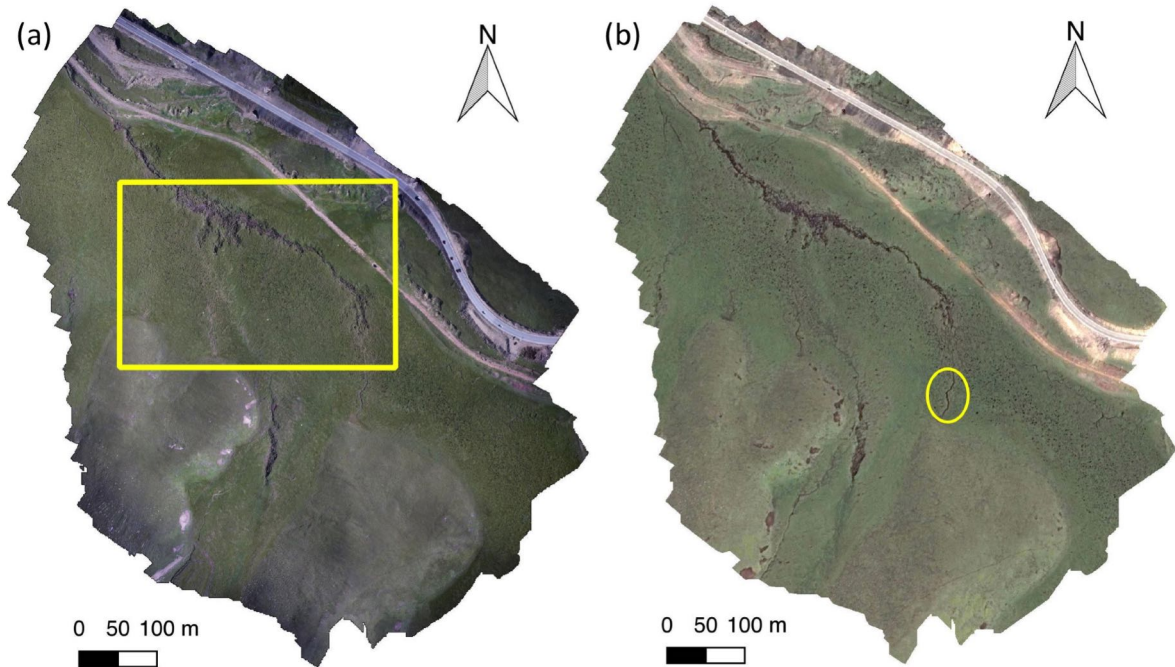


Figure 2.2: The Digital Orthophoto Map (DOM) and a subset of the Google image. (a) is the DOM constructed from the UAV images. The yellow rectangle denotes the extent of Figure 2.4. (b) is a subset of the Google image with the same extent of (a). The yellow circle marks a gully that will be discussed in Section 2.4.1

one meter to nearly one hundred meters. Most of these gullies incise less than two meters on the surface. Google Earth shows that the extent of the gully (Figure 2.1c) remained nearly unchanged over three years (2012–2015). Therefore, we assume that the gullies in this area had similar extents in both 2015 and 2016. Erosional features such as sinkholes, gully heads, tunnels, and collapses are common within the gullies. Since gullies are narrow landforms, most of them appear as dark line segments in the remote sensing images.

The remote sensing datasets we used include one Digital Orthophoto Map (DOM) and high-resolution image. The DOM was constructed from Unmanned Aerial Vehicle (UAV) images, and its spatial resolution is 0.06 m (see more in Section 2.2.2.1). We downloaded image patches from Google Earth using SAS.Planet (www.sasgis.org/sasplanet). The images were acquired by the Pleiades satellite and are freely accessed. We mosaicked them into a single one which is referred to as Google image in

this study. The acquisition time of the Google image is August 2015, and its spatial resolution is 0.6 m. Both the DOM and Google image have red, green, and blue bands. Compared with satellite images, the very high-resolution DOM shows the detailed information of the surface but is limited to a small area (the yellow polygon in Figure 2.1a).

2.2.2 Methods

2.2.2.1 Generating DOM for a small area

We acquired aerial images using an Unmanned Aerial Vehicle (UAV) during our field-work in July 2016. The UAV platform was Trimble UX5, and the camera model was Sony A5100. We used the Trimble Access software to plan the aerial mission, perform the task, and monitor the flight. The flight height was 200 m above ground. Both the overlap of in-flight and cross-flight were 80%. Six ground control points (GCPs) were roughly evenly-distributed in the extent of the DOM (0.4 km^2). We used Global Positioning System (GPS)-Real Time Kinematic (RTK) to measure the coordinates of the GCPs. We used the Trimble Inpho UASMaster software to generate the DOM from the UAV images and the GCPs.

2.2.2.2 Gully detection using GEOBIA

We used GEOBIA to detect thermo-erosion gullies automatically. GEOBIA uses the object, instead of pixels, as the smallest detection unit and incorporates many features such as color, texture, and shape in the classification. Figure 2.3 illustrates the main steps of our GEOBIA method. Below, we will use a patch of the DOM (shown in Figure 2.4a) as an example of the source image to describe each step in further detail.

During the image segmentation step, we partitioned the whole image into multiple objects. Each object is a locally homogeneous region. Image segmentation converts the image elements from pixels into objects. We used the mean shift algorithm for image

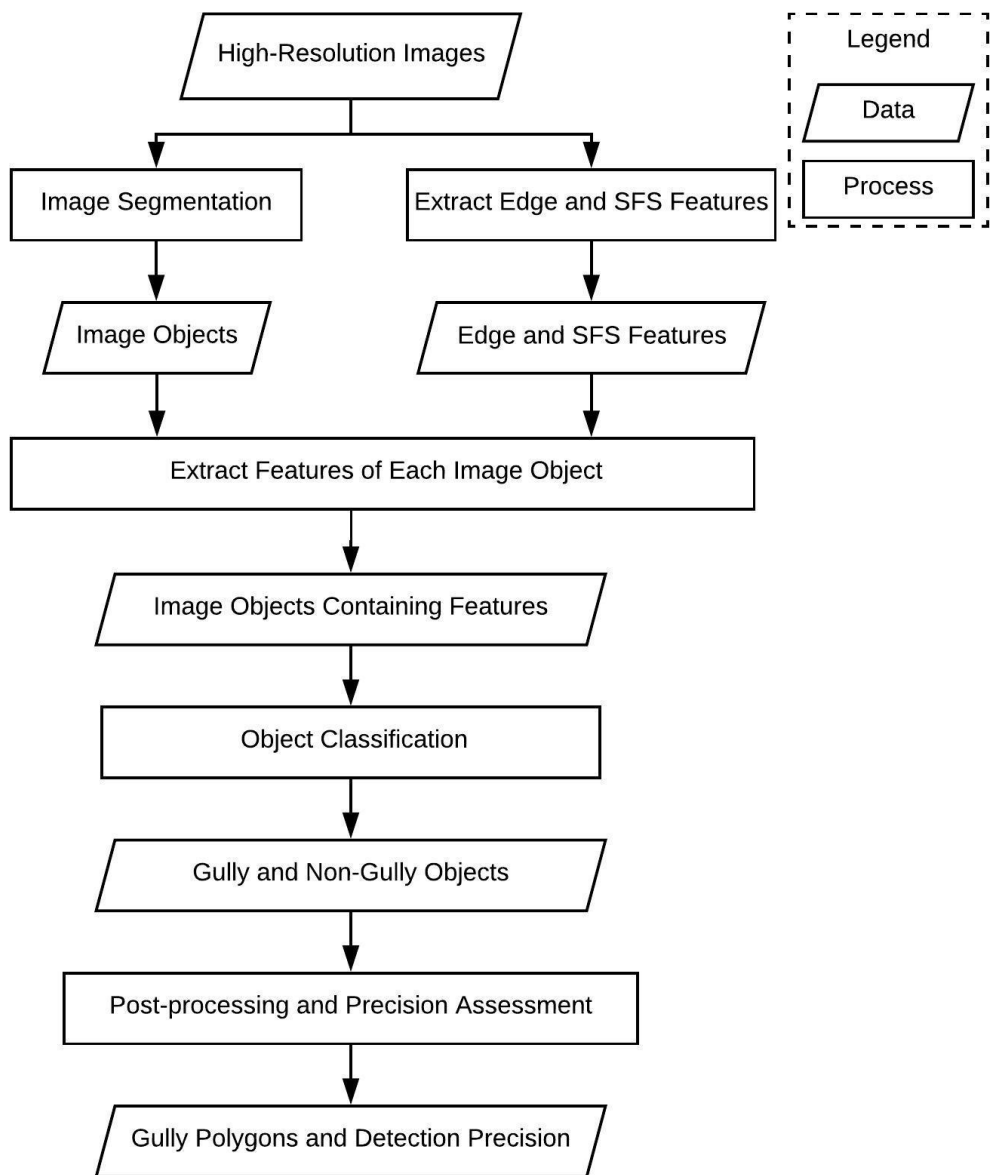


Figure 2.3: Flowchart of our GEOBIA method for gully detection.

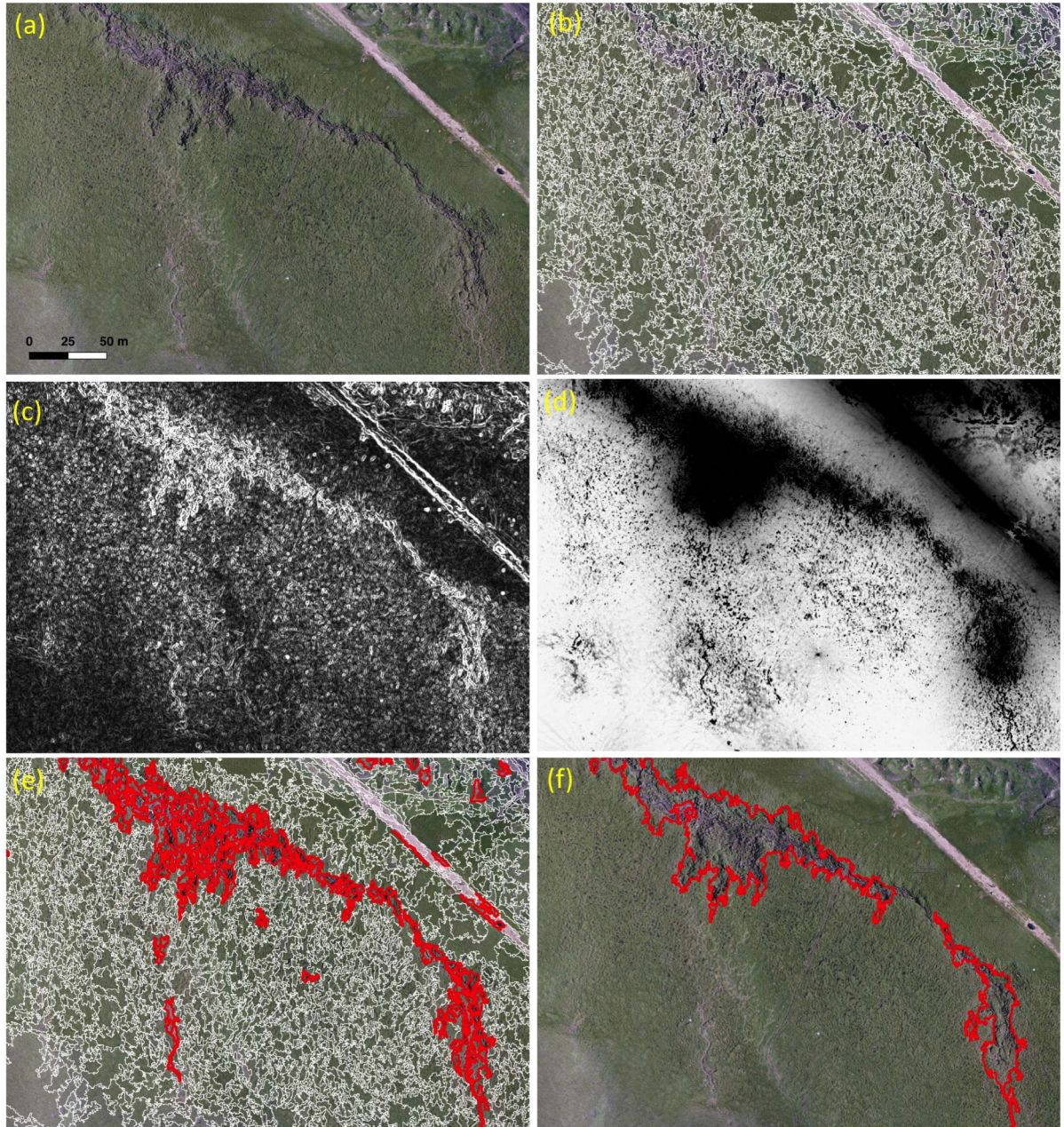


Figure 2.4: Examples of intermediate and final results of our GEOBIA method: (a) is a patch of the DOM; (b) shows the segmentation results. The white polygons denote the segmented image objects; (c) shows the edge features; (d) shows the pixel shape index (PSI) (see more in the text). A brighter color means a greater PSI value. (e) shows the classified gully and non-gully objects with red and white polygons, respectively; (f) shows the final detection results. Only the gully polygons are kept.

segmentation. The mean shift algorithm is well suited to analyzing a complex feature space and is widely used in image segmentation (Comaniciu and Meer, 2002). Due to the large size of the high-resolution images, we used a parallel image segmentation strategy that subdivides the source images into multiple subsets before applying the mean shift algorithm (Huang et al., 2014; Hu et al., 2016). The parallel image segmentation strategy is the same as the one in (Huang et al., 2014). More specifically, we downsampled the DOM to six spatial resolutions (including 0.06 m, 0.12 m, 0.24 m, 0.48 m, 0.96 m, and 1.92 m) to save computing time and then segmented the resampled images and obtained six sets of segmentation results. By visually comparing these six sets, we found that the images of 0.48 m resolution gave the best segmentation results that would facilitate further processing. Six parameters of the mean shift algorithm control the quality of segmentation results and influence the extent and shape of homogeneous regions (Comaniciu and Meer, 2002). Therefore, the combination of these parameters can be considered as the metric of object homogeneity. These parameters include the spatial bandwidth, color bandwidth, minimum size of each object, gradient window size, weight of gradient magnitude and local pattern, and threshold of similarity for fusing adjacent objects. After a few tests, we empirically set them as 7.0, 5.0, 100, 3, 0.3, and 0.3, respectively. Figure 2.4b shows the results of image segmentation applied to Figure 2.4a.

During the feature extraction and selection step, we extracted the edge features, structural feature set (SFS) texture, and spectral information of each object. Firstly, we applied the Sobel operator to the DOM to extract the edge features. We utilized the edge features because micro-landforms (such as small ponds, isolated vegetation, exposed soil, and collapsed surface inside the gullies), characterize distinct edges in the high-resolution image. Figure 2.4c shows that the strong edge features correspond to gullies and roads. Secondly, we used the SFS extraction function provided by the “Orfeo Tool Box” (Inglada and Christophe, 2009) to extract the SFS values of each pixel. The SFS describes six statistical features (length, width, pixel shape index, w-mean, ratio,

and standard deviation) of the direction-lines histogram (Huang et al., 2007). Direction lines are the lines through the central pixel with equal space (Shackelford and Davis, 2003; Zhang et al., 2006). The length of a direction line is mainly determined by the similarity between the central pixel and the pixels on the radiating lines. We define a threshold of 10 to represent the similarity when using the Google image. Specifically, the pixel shape index (PSI) value indicates the contextual information of the central pixel (an example is shown in Figure 2.4d). Usually, a greater PSI means that the central pixel is located within a larger homogeneous region. Each pixel has ten digital values (one for the edge, six for SFS, and three for spectral information) of features. We utilized all the features listed above when performing object classification. Lastly, we calculated the average value of all the pixels within each object for any given features to obtain the object features.

We used the support vector machine (SVM), a supervised learning method (Wu et al., 2004; Cortes and Vapnik, 1995), to classify all the objects into gully and non-gully. After many tests, we chose the radial basis function as the SVM kernel function (penalty parameter $C = 1$; Kernel coefficient gamma = 0.1). We used the C-Support Vector Classification (SVC) function provided by the “scikit-learn” library (Pedregosa et al., 2011) with the following strategies specifically implemented for gullies. First, we standardized the spectral, edge, and SFS features to data with zero mean and unit variance. Such standardization helps to improve the classification performance of SVM (Schölkopf et al., 2002). Next, we used ten of the field-identified gully polygons (more in Section 2.2.2.3) and 13 non-gully polygons representing the typical non-gully land covers in this region, including grasses, roads, and bare lands, to train the SVM model. We analyzed the intersection between these training polygons and the image objects (results of image segmentation). Any object whose intersection area is greater than the half of the object’s area was chosen as a gully or non-gully training sample. Lastly, we used the trained SVM model to classify all the objects into the gully and non-gully categories. Figure 2.4e shows the SVM classification results, with the gully/non-gully

objects marked by red/white boundaries.

The post-processing step includes removing non-gully objects, merging objects belonging to the same gully, and removing noise polygons. First, we removed the non-gully objects and only kept the gully objects for further processing. Next, because one gully may have been segmented into multiple objects in the segmentation step, we merged the objects that belonged to the same gully into a gully polygon. Specifically, we built an adjacency matrix of objects and used it to merge the adjacent objects recursively. We define the adjacent objects as two objects that touch each other, and their intersection is one or multiple lines. The adjacency matrix is a square matrix whose element values are 1 or 0 which represent whether two objects are adjacent or not, respectively. The merging steps include (1) to select the first object as the start; (2) to recursively identify the adjacent objects based on the adjacency matrix until no more adjacent object can be found; (3) to merge these adjacent objects into one polygon. We iteratively performed the merging steps on the unmerged objects until no more unmerged objects remained. Then, we considered those polygons which were isolated, small, and non-narrow as noise polygons and removed them. We chose an area threshold of 70 m^2 to remove the small polygons. The gullies are typically narrow features, so we defined a narrowness metric (N) to represent how narrow the gully is as

$$N = \frac{P^2}{S} \quad (2.1)$$

where P and S are the perimeter and area of the polygon, respectively. For example, N of a circle is 4π . A larger N means a narrower polygon. We only kept polygons with $N > 25$. We did not utilize N when classifying objects because an object can only cover part of one gully. We also removed any noise polygon with a spectral value greater than (50, 45, 40) or an edge feature smaller than 20. Lastly, we filled the holes inside each gully polygon.

2.2.2.3 Validation Method

We identified and mapped 20 thermo-erosion gullies in the field in July 2016. We walked along gully boundaries, one to two meters away from the gully cliffs, with GPS-RTK and measured the boundary of each gully at centimeter-level accuracy. One of the gully boundaries we outlined is shown in Figure 2.1a. We considered these 20 polygons as the ground truths for validating the detection results.

We quantitatively assessed the validation using the intersection over union (IOU) which is independent of the image resolution. Assuming that A is a gully polygon detected from the remote sensing images and B is a ground truth polygon identified from the field, then we calculated the IOU as

$$IOU(A, B) = \text{area}(A \cap B) / \text{area}(A \cup B) \quad (2.2)$$

The IOU value ranges from 0 to 1. A typical threshold of IOU is 0.5 for evaluating detection results in term of both their locations and extents. Here, we considered a detected polygon as a true detection if its IOU is greater than 0 (i.e., there is an overlap between the detected polygon and any ground truth polygon). The reasons for such choice are that (1) intersections can indicate the locations of gullies and (2) both the ground truth and detected gully polygons contain uncertainties. Otherwise, it is a false detection. We further calculated the detection precision as

$$\text{precision} = \frac{C_T}{C_T + C_F} \quad (2.3)$$

where C_T and C_F are the numbers of true detections and false detections, respectively.

2.3 Results

We detected 66 polygons from the Google image, 23 of which (red polygons in Figure 5a) are true detections and match the locations of 18 out of 20 ground truth polygons

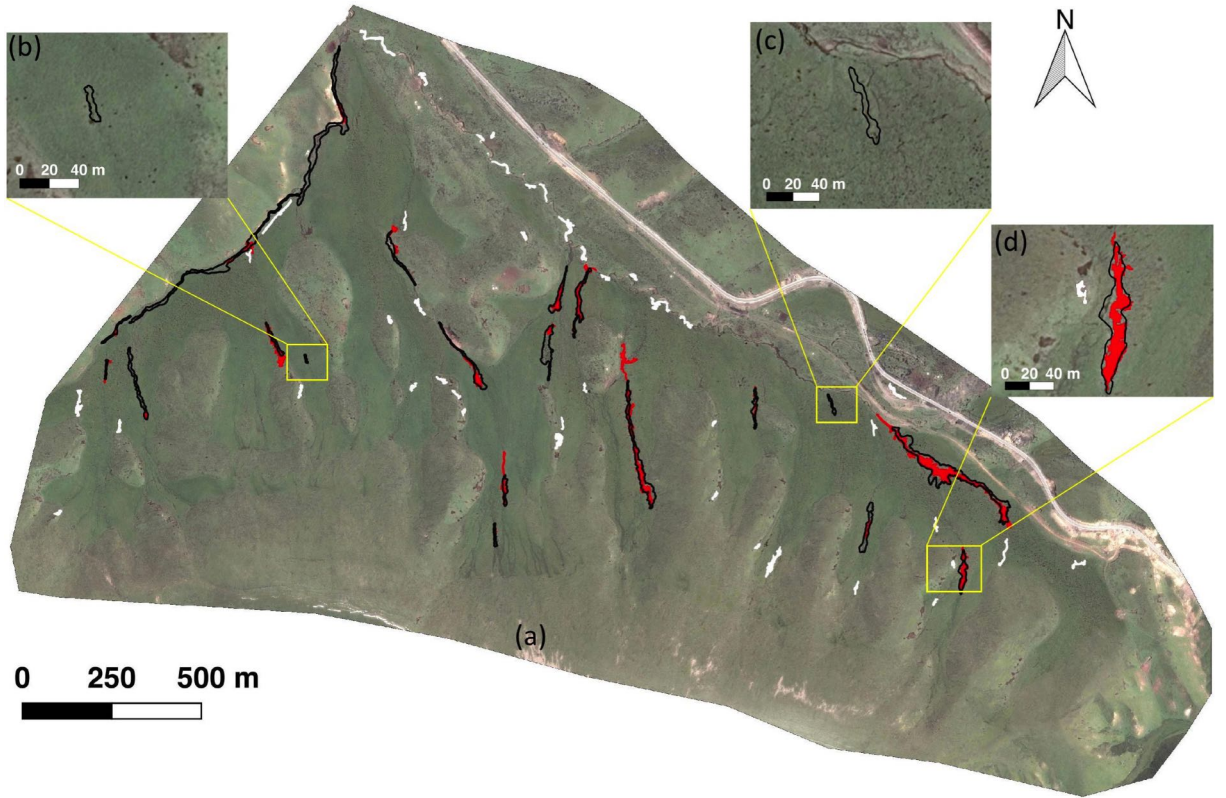


Figure 2.5: (a) Thermo-erosion gullies detected from the Google image: the red polygons are true detections; the white polygons are false detections; the ground truth polygons are outlined in black. (b) and (c) show the two ground truth polygons that we failed to detect from the Google image. (d) is an example of the true detection.

(e.g., Figure 2.5d). The two missed ground truth polygons are shown in Figure 2.5b and 2.5c. Therefore, our method detected the locations of 90% gullies from the Google image over the entire study area. 43 polygons (white polygons in Figure 2.5a) are false detections, which results in a low detection precision of 34.8%. Moreover, Figure 2.5a shows that most of the detected polygons only cover parts of the ground truth polygons or even extend beyond the ground truth polygons. Most of the false detections are water flows, vehicle tracks, or in areas of bare land.

Within the same extent, the detection results from the DOM and those from the Google image are significantly different (shown in Figure 2.6). The detection precision of the DOM is 75%: three true detections and one false detection (Figure 2.6a). In contrast, the detection precision of the Google image within the same extent is lower

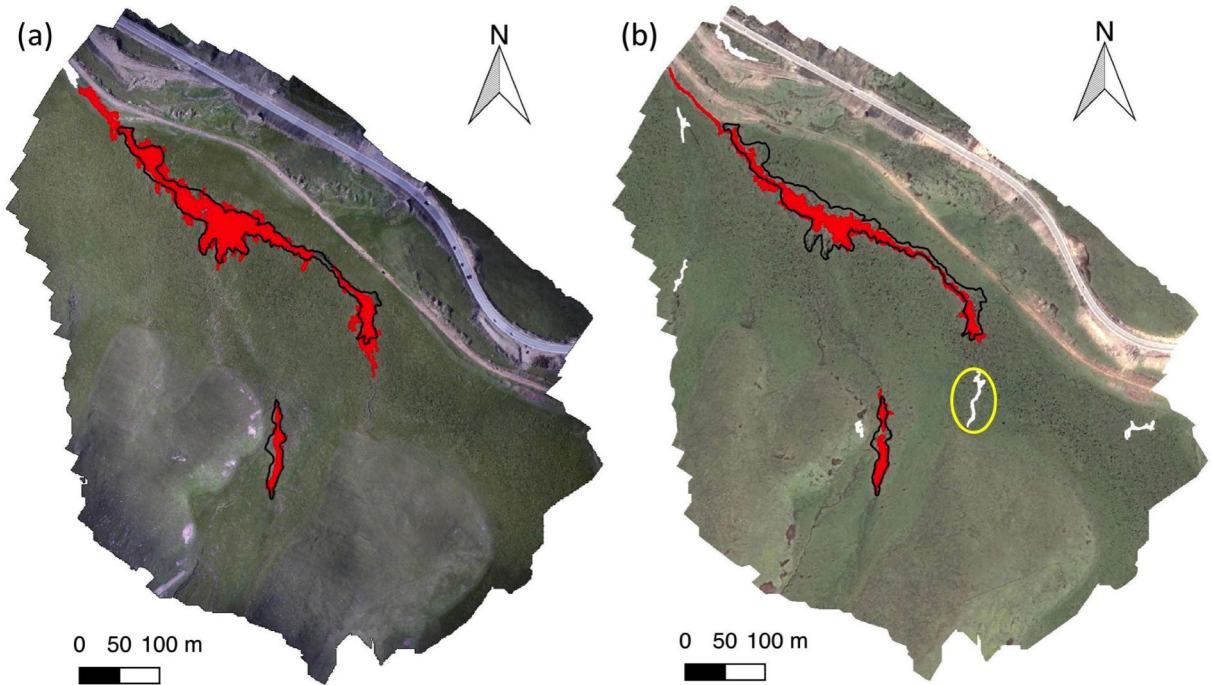


Figure 2.6: Detection results using the DOM (a) and the subset of the Google image (b). The red polygons are true detections; the white polygons are false detections; the ground truth polygons are outlined in black. The yellow circle marks a false detection that we will discuss in Section 2.4.1.

at 40%: it has four true detections and six false detections (Figure 2.6b). Both sets of results have detected polygons in the location of the ground truth polygons, but the results using the Google image have more false detections than the DOM-based results. Conversely, in terms of detecting an individual gully, results of the Google image are better than the DOM-based ones. When comparing detected polygons in the northern ground truth polygon (the larger black polygon) in Figure 2.6, detected polygons in Figure 2.6b cover the entire gully, but the ones in Figure 2.6a pick up two separated parts of the gully.

2.4 Discussion

2.4.1 Factors that influence gully detection

Many factors influence the detection process and precision. These factors include the platforms of remote sensing sensors (UAV and satellites), the evolution of gullies, the acquisition times of remote sensing and field data, and the morphology of the gullies.

The platforms of remote sensing sensors influence the representation of source images, especially the resolution, and thus affect the detection results. The UAV images were acquired from an aerial platform about 200 m above the ground. They have a very high resolution and contain targets such as topography, shadow, and vegetation observed from different angles. The DOM generated from the UAV images can capture the microtopography inside the gully but contains distortion and noise at the same time. The distortion due to the satellite platform can be ignored because our study area is relatively small when compared to the whole scene of a satellite image. The Google image has a relatively coarser resolution and cannot capture the microtopography, and only shows dark and rough regions inside the gullies. Moreover, the bare land, water tracks, and shadow also appear dark in the Google image. The dark appearance of gullies and other landforms in Google image result in many false detections. For example, Figure 2.6a and Figure 2.6b have the same extent, but Figure 2.6b has more false detections than Figure 2.6a. The evolution of gullies changes the surface, but remote sensing images and ground truth polygons are snapshots of the gully evolution at different times. The evolution of thermo-erosion gullies typically lasts a few years or decades (Godin and Fortier, 2012, 2010). Most of the thermo-erosion gullies in the study are still actively developing. Moreover, they are likely at different stages of evolution. The differences in the two sets of detection results may also result from possible temporal changes of the gully landforms from the acquisition of the Google image (2015) to the acquisition of the DOM and our fieldwork (2016). For example, we

detected one gully from the Google image within the yellow circle in Figure 2.6b and can visually confirm it from Figure 2.2b. However, neither our fieldwork of July 2016 nor the DOM identified this particular gully. The DOM also shows a subtle gully at the same location but is quite different from the other two gullies (outlined by the black polygons in Figure 2.6a). We infer that the gully did not disappear but had already changed.

The gully morphology can cause significant variation in geometric and radiometric properties, which further complicates the automatic detection. The gully width, depth, and length vary not only one by one but also within individual gullies. The vegetation and exposed soils within the gullies show a certain level of similarity to other land covers, thus leading to some false detections. Moreover, both the geometric variations and microtopography within gullies violate the assumption of GEOBIA that one object is a homogeneous region, and equivalently, a gully consists of several homogeneous regions. In our method, we set the mean shift parameters to relax the requirements of homogeneity in the image segmentation regions. However, this strategy introduces two negative consequences: (1) it increases the variation of the extracted features within each object; and (2) one object may contain pixels inside and outside a gully.

2.4.2 Technical challenges of GEOBIA

Despite our efforts at optimizing GEOBIA methods for gully detection, the following three technical challenges remain.

(1) The quality of image segmentation is essential for accurate detection, but the segmentation is not error-free. For example, if one segmented object extends outside a gully (i.e., it includes both gully and non-gully pixels), we would still classify this object as either gully or non-gully. In this case, the detection is inevitably incorrect. Moreover, the image segmentation algorithm directly affects the size and shape of objects and indirectly affects the averaged feature values of each object.

(2) Many GEOBIA parameters can influence the detection results, but it can be

challenging to optimize them for producing the best results. For example, there are six parameters which can influence the behavior of the image segmentation algorithm. We chose the values of the parameters from the original mean shift paper (Comaniciu and Meer, 2002) as the initial values, then adjusted them, especially the color bandwidth and the minimum size of each object, for different datasets. We needed to run a considerable number of tests when adjusting the parameters, which makes it difficult to choose the best values.

(3) Post-processing requires high-quality results from the previous steps and expert knowledge. We cannot merge some classified objects in one gully in the post-processing step because they do not touch any other objects. This is non-ideal because image segmentation divides the original image into many objects, yet classification cannot group all the objects belonging to the same gully based on the extracted features. We set the criteria based on the color, edge feature, shape, and size of the gullies to remove noise polygons, which requires a priori knowledge about the general features of the gullies in the study area.

2.4.3 Erroneous features from the ground truth

The gully boundaries we identified from the field are different from the boundaries detected from remote sensing images. Due to safety concerns, we measured the boundary close to, but not precisely at the edge of the gully. This results in the ground truth polygons containing not only gully features but also a small portion of non-gully features. Furthermore, we cannot rule out the possibility that we may overlook some thermo-erosion gullies in the field.

2.4.4 Future work

In the future, we will improve the source data and methods to achieve better detection results. Improving the quality of validation data and conducting synchronous field validation are a priority for future studies. Our study area is small, so adding more

data is feasible and may help improve results. For example, it is possible to distinguish thermo-erosion gullies from water tracks if we utilize multiple band images, such as the images with eight bands from the WorldView-2 satellite. Utilizing topography data can help detect gullies (Shruthi et al., 2011; d’Oleire Oltmanns et al., 2013). Accordingly, we will incorporate more data such as digital elevation models and remote sensing images with multiple bands in the GEOBIA workflow. However, adding more data is impractical for a large area. In GEOBIA, any flawed results of the previous step can propagate to the following steps. Thus, we need to check and improve the output of each step, including a quantitative assessment of image segmentation results.

The gully geometries are necessary for understanding the evolution of gullies, and we still need to obtain not only their locations but also spatial extent. With the guideline of detection results, we can quickly edit the results and obtain the geometries for further analysis. However, the manual edit is labor-intensive and cannot apply to a large area. Automatically mapping not only the locations but also the boundaries of gullies is the goal we still need to achieve.

2.5 Summary

In this chapter, a GEOBIA-based mapping method was applied to high-resolution remote sensing images from Google Earth and UAV DOM to detect thermo-erosion gullies over Eboling Mountain in the northeastern Tibetan plateau. The locations of 90% of the thermo-erosion gullies in the entire study area were correctly detected from the Google image. However, the detection results using the Google image included a high number of false detections. Using the DOM, which covers a fraction of the study area, it obtained a greater detection precision.

This is the first study applying GEOBIA to high-resolution images and aiming to automatically map thermo-erosion gullies on the Tibetan Plateau. It provides a unique perspective on the challenges and potentials of mapping non-lake thermokarst

landforms.

Various characteristics of thermo-erosion gullies and erroneous samples contained in training data lead to the unexpected performance of GEOBIA. In particular, GEOBIA is a complex algorithm containing many steps, and erroneous output in the previous step would affect the next step. Moreover, many parameters of GEOBIA require experience and understanding of the input data, which makes extending to larger areas difficult. Therefore, in next chapter, I propose a new method based on deep learning which has a high capability to represent the various characteristics of thermo-erosion gullies, high tolerance to erroneous samples, and can learn parameters automatically from training data.

Chapter 3

Mapping Thermo-Erosion Gullies Using Deep Learning

This chapter presents the study that utilized cutting-edge deep learning algorithms to automatically map a type of non-lake thermokarst landforms (i.e., thermo-erosion gullies) on high-resolution images. A semantic segmentation (i.e., DeepLab) based on convolutional neural networks was adopted, and a method with key steps including preparing training data, fine-tuning, inference, and post-processing was proposed. Validating against the field measurements and manual digitizing results, we obtained an F1 score of 0.74 (precision is 0.59 and recall is 1.0), showing that the proposed method can effectively map small and irregular thermokarst landforms. It is potentially viable to apply the designed method to mapping diverse thermokarst landforms in a larger area where high-resolution images and training data are available.

The study area and targets in this chapter are the same as I introduced in Chapter 2, but with a totally different methodology. In Chapter 2, the method based on GEOBIA cannot delineate their boundaries accurately. To obtain the boundaries of thermo-erosion gullies, a state-of-the-art deep learning algorithm was adopted, because deep learning has been used in many complex scenarios and achieved outstanding results.

3.1 Introduction

In this study, we proposed a method based on deep learning to automatically map small, irregular thermokarst landforms from high-resolution remote sensing images. Our method innovatively utilizes a supervised deep learning algorithm building on the Convolutional Neural Networks (CNN) (LeCun et al., 1998). Deep learning is widely used and has achieved unprecedented and promising results in many fields (such as computer vision and artificial intelligence) in the past few years (Krizhevsky et al., 2012; LeCun et al., 2015; Silver et al., 2017). Moreover, many studies apply deep learning to map land cover, detect objects, and estimate poverty from remote sensing images (Guo et al., 2018; Huang et al., 2018a; Jean et al., 2016; Zhu et al., 2017). However, none of them targets thermokarst landforms. The objectives of this study were: (1) to assess the capability of CNN in mapping non-lake thermokarst landforms from high-resolution images; and (2) to analyze the distribution of thermokarst landforms in the study area in the Northeastern Tibetan Plateau.

Due to the small size of thermokarst landforms, we needed high-resolution remote sensing images (whose spatial resolution is higher than one meter). Previous methods use multispectral images for mapping landscape dynamics and thermokarst landforms (Belshe et al., 2013; Nitze and Grosse, 2016; Nitze et al., 2017; Rudy et al., 2013). However, the ones with high spatial resolution are typically only available from commercial satellites and expensive. Instead of integrating various remote sensing datasets, we only utilized three-bands (i.e., red, green, and blue) images, which are relatively easy to obtain from satellites or airborne platforms. In this paper, we demonstrate the performance of the proposed method and discuss its advantages as well as limitations.

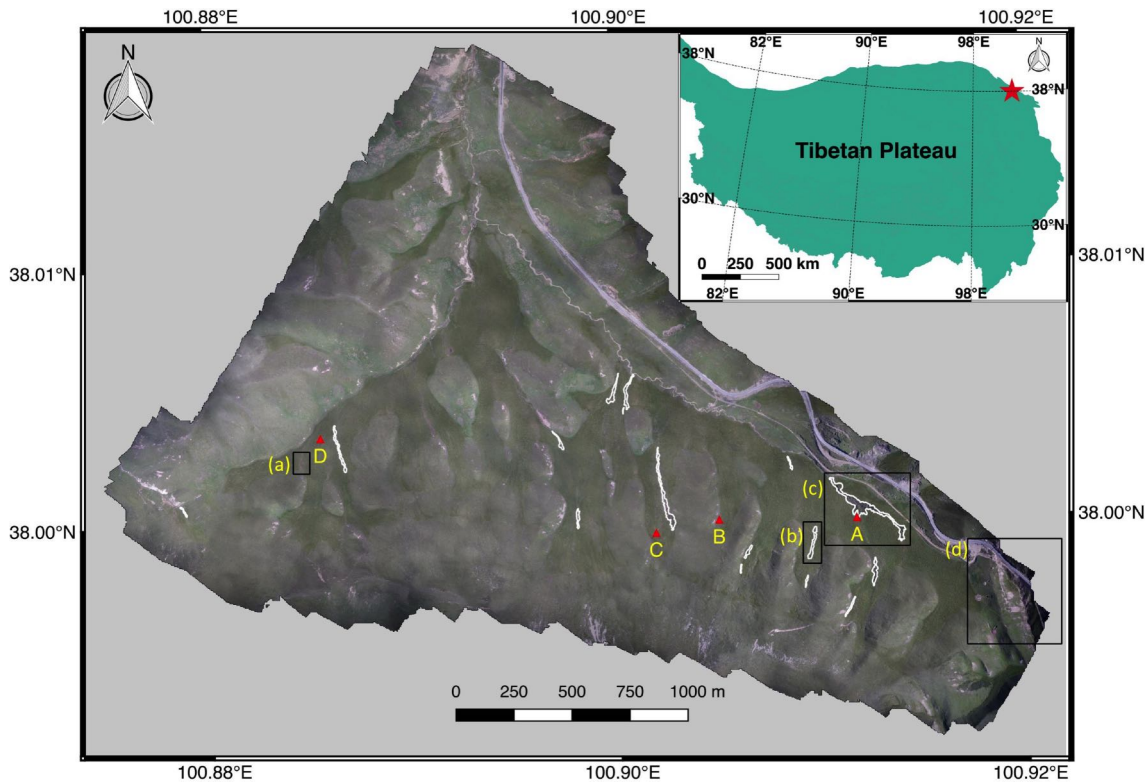


Figure 3.1: Digital Orthophoto Map (DOM) of the study area. The white polygons are the ground truth polygons. The red triangles and yellow uppercase letters indicate the positions and the names of ground photos shown in Figure 3.2, respectively. The black rectangles with lowercase letters indicate the extents of the DOM subsets shown in Figure 3.5. The red star in the inset shows the location of our study area on the Tibetan Plateau.

3.2 Study area

Figure 3.1 shows high-resolution imagery of the study area. More description on the study area can be found in Chapter 2 section 2.2.1.

Three types of thermokarst landforms, including thermo-erosion gullies, sinkholes, and thermokarst pits, are present in this area. Sinkholes and thermokarst pits are rare and subtle on remote sensing images. Hence, we only target thermo-erosion gullies (hereafter referred to as “gullies”) in this study. These gullies are characterized by erosional features such as collapsed ground, ponds, disturbed vegetation, and exposed soil (Figure 3.2a). Most of them are narrow features on the images (Figure 3.2a,e). Their width and length range from around 1 to 30 m and 20 to 500 m, respectively.

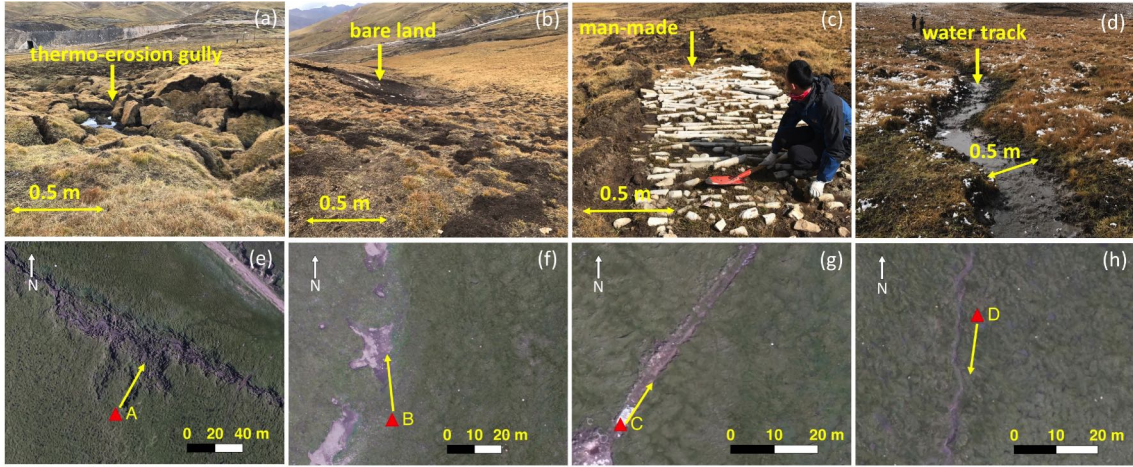


Figure 3.2: Ground photos (a–d); and their corresponding DOMs (e–h) of different land covers or landforms in the study area. In (e–h), the red triangles indicate the camera positions and the yellow arrows indicate the looking directions.

Most of these gullies also incise more than one meter into the ground (Figure 3.2a).

In addition to thermokarst landforms, diverse land cover types such as water tracks, bare land, and roads are found in the study area (Figures 3.1 and 3.2). Anthropogenic disturbance and natural processes contribute to bare land (Figure 3.2b,f) and man-made objects (Figure 3.2c,g). The low permeability of permafrost and saturated organic soil layer lead to many water tracks (Figure 3.2d), which are also narrow features on remote sensing images (Figure 3.2h).

3.3 Methods

3.3.1 Collection of UAV images and creation of digital orthophoto map

We collected the UAV images in the field in July 2016. The UAV platform, camera, and software for collecting UAV images are the same as the ones in section 2.2.2.1 of Chapter 2. We deployed 12 ground control points (GCPs) that are evenly distributed within the study area and measured their locations using Real-time Kinematic (RTK) with centimeter-level positioning accuracy. We used the Trimble Inpho UASmaster software to create a DOM using the measured GCPs and to generate a digital elevation

model (DEM). Table 3.1 lists the software parameters and settings. The final DOM (Figure 3.1) has a spatial resolution of 0.15 m and contains three spectral bands of red, green, and blue. The DEM covers the entire study area. It was used for assisting the manual digitizing of gullies and simulating stream vectors. The horizontal resolution and vertical accuracy of the DEM are 0.41 m and 0.12 m, respectively.

3.3.2 Collection of ground truth polygons

The ground truth polygons were collected using the RTK measurements in the field and manually delineated (digitizing) on the DOM. In the field, we walked along the edges of the thermo-erosion gullies and measured the boundaries of nine gullies in July 2016. We considered gully banks with collapse features as parts of gullies. We manually delineated seven gullies in QGIS (version 2.18.14, qgis.org). The UAV-based DEM also helped us to distinguish gullies from water tracks because the first ones incise more than one meter into the ground. We obtained 16 polygons (the white polygons in Figure 3.1) as the ground truths. Figure 3.3 gives the method of obtaining each polygon. We note that their boundaries are 1–2 m away from the gully edges because we could not walk exactly along the edges due to safety concerns.

3.3.3 Preparation of training data

We chose training polygons to prepare images to train our supervised learning method (Figure 3.6). Although some public datasets such as the PASCAL VOC 2012 images (Everingham et al., 2015) are suitable for training and evaluating deep learning algorithms, none of them contain thermo-erosion gullies. Therefore, we prepared the training data specifically for thermo-erosion gullies. Among these training polygons, 11 of them are from the ground truths and 15 from manually identifying non-gully regions (Figure 3.4 shows their distribution and sources). The 11 ground truths are representative of all gullies in the study area. The rest ground truths and the other regions on the DOM were used as test data. The 15 non-gully polygons are essential because they

Table 3.1: Parameters and settings of the Trimble Inpho UASmaster software for producing the digital elevation model and digital orthophoto map

Steps	Parameter name	Value
Preparation	Projected Systems	WGS-84-99E
	Cameras/Sensors	UX5-5100
	Number of used images	280
	Number of strips	20
	Flying height (min/avg/max)	4018.4/4030.8/4045.4 [m]
	Terrain height (min/avg/max)	3443.3/3587.6/3832.6 [m]
	Average photo scale	1:24442
	Count of Ground Control Points	12
	Sensor (width/height) [pixel]	6000/4000
Camera Calibration	Distortion type	Polynomial
	Focal length [mm/pixel]	15.5785/3974.0311
	Focal length (Fx/Fy) [pixel]	3973.9634/3974.0987
	Principal point (x/y) [mm & pixel]	0.1388/0.0209 & 2964.0993/1994.1725
	GNSS-Mode	On
Block Adjustment	Earth Curvature Correction	On
	Refraction Correction	On
	Extraction With Adjustment	Full Resolution
Georeferencing	Exterior Orientation	extensive
	Generate DSM	Very dense (slow)
Surface and Ortho Generation	Pixel Size	0.15 m
	Output format	GeoTiff

Note: Please refer to the User Guide of Inpho UASmaster for the explanation of the settings and parameters.

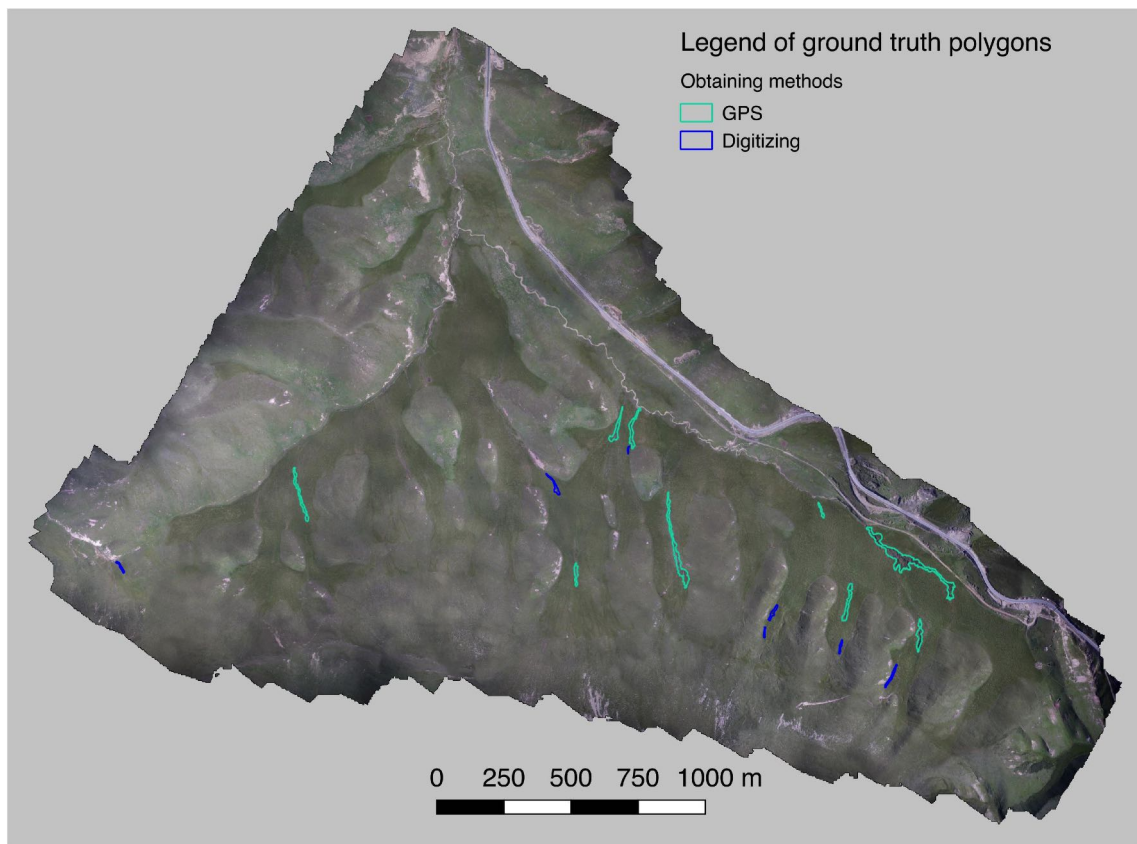


Figure 3.3: Map of the ground truth polygons and their obtaining methods. Nine of them were collected in the field using GPS Real-Time Kinematic. Seven of them were manually delineated (digitizing) on the DOM.

help distinguish the gullies from the similar non-gully land covers during the training. To prove that our choice of training polygons is representative, we conducted 21 (three groups) independent experiments using different combinations of training data, which is similar to bootstrapping in statistics. All experiments had the same setting except their training polygons. The first experiment (first group) used all ground truths and non-gully polygons. Both the second and third groups of experiments randomly selected 70% of ground truths. The second group randomly selected 70% of non-gully polygons while the third group used all of them. Using 70% of ground truths as training data is common in machine learning application. In the third group, the number of training polygons equaled the number of representative selection we described above. Lastly, we compared the results of these 21 experiments with the final results reported in this study.

We utilized the training polygons to extract the subsets of the DOM (termed as sub-images) and to generate the corresponding label images. For each training polygon, we adopted the following two steps to extract a sub-image. (1) We expanded the training polygon by adding a 20-m-wide buffer area. (2) We utilized the minimum bounding rectangle of the expanded area to extract a subset of the DOM by using the Geospatial Data Abstraction Library (GDAL, www.gdal.org). After extracting operation, we obtained 26 sub-images. Among them, 15 contain non-gully land covers such as a water track, bare land, and road, as shown in Figure 3.5a,d. The other 11 sub-images (e.g., Figure 3.5b,c) contain both gullies and their surrounding non-gully pixels. To obtain label images, we first rasterized all the ground truth polygons into one single image using GDAL. Then, we extracted 26 label images such as those shown in Figure 3.5a-L to d-L from this image.

We needed to further subdivide the sub-images and label images into small patches due to the input requirement of our method. The deep learning algorithm (more in Section 3.3.4) was originally developed to process images from everyday scenes such as the ones in the PASCAL VOC 2012 dataset. These images have small dimensions (on

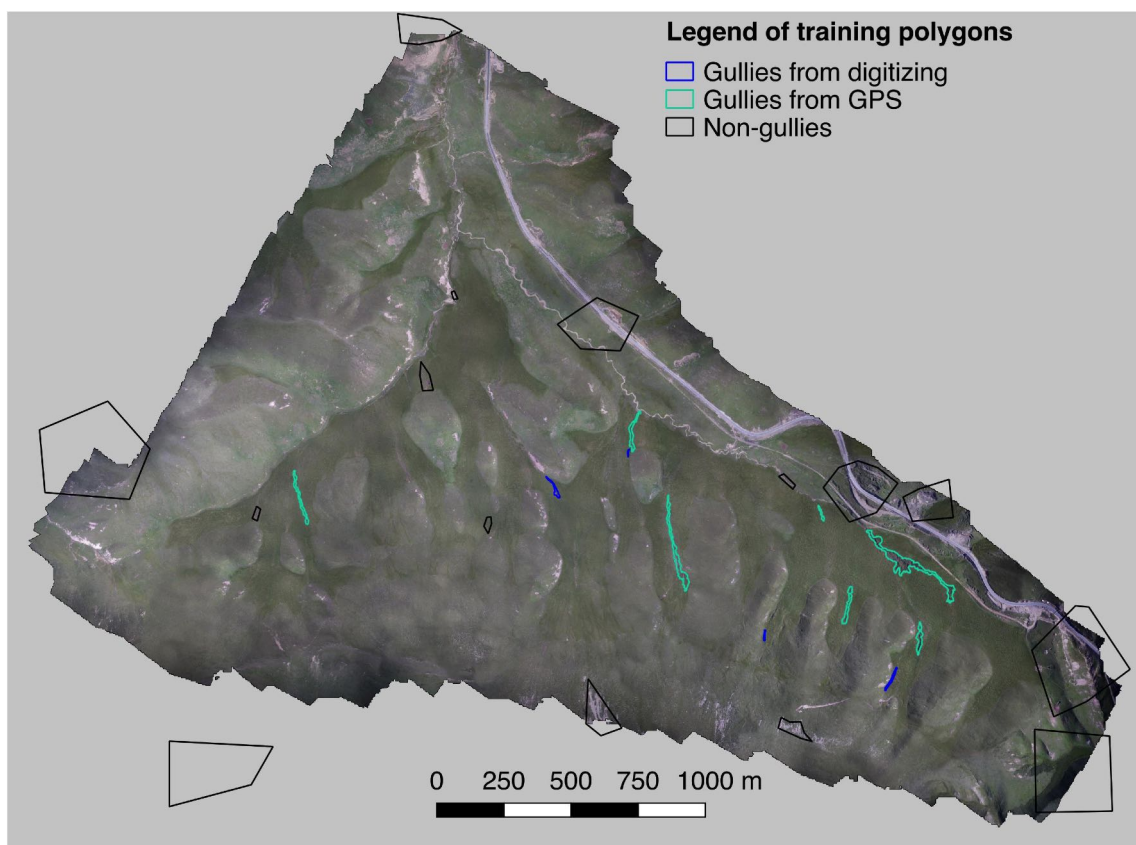


Figure 3.4: Distribution of the training polygons: 15 of them are non-gullies; seven were collected from field GPS measurements; and four were from manual delineation (digitizing).

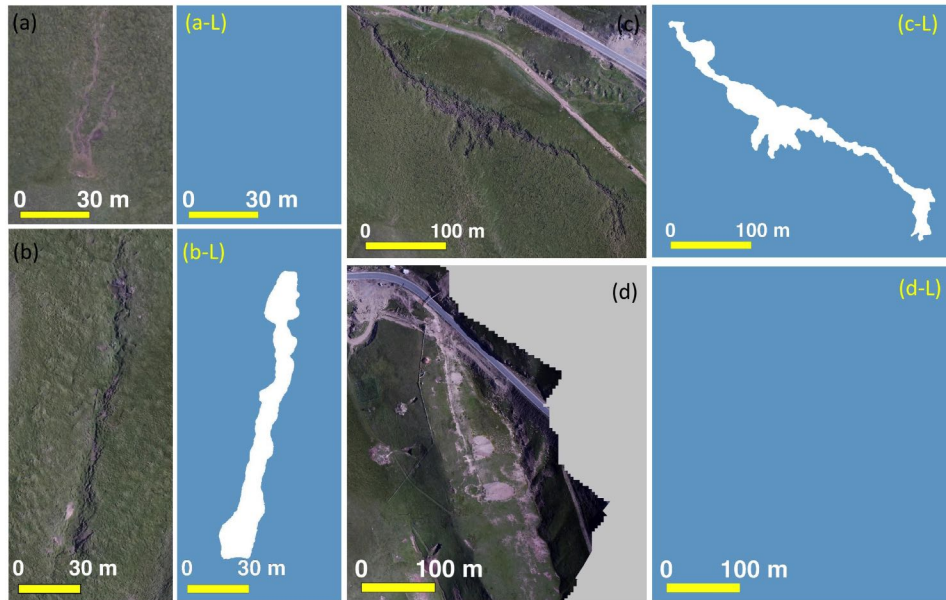


Figure 3.5: Examples of the DOM subsets used for training: (a,d) examples of sub-images containing non-gully land covers; (b,c) examples of sub-images containing gullies; and (a-L–d-L) their corresponding label images. The white pixels in (a-L–d-L) indicate gullies, while non-gully pixels appear as light blue. A label image appears entirely light blue (e.g., (a-L,d-L)) if the corresponding sub-image does not contain a gully.

the order of 500×500 pixels) and file sizes (smaller than one megabyte). High-resolution remote sensing images are larger than everyday images. For example, the dimension and file size of the DOM are $28,162 \times 21,003$ pixels and 2.4 gigabytes, respectively. The dimension of sub-images ranges from 313×455 to 3011×2706 pixels depending on the size and shape of the training polygons. Moreover, because of the limitation of Graphics Processing Unit (GPU) and the algorithm, it is not possible to directly input an image with large dimension (such as greater than 1000×1000 pixels) to the deep learning algorithm. Therefore, we subdivided each sub-image and the corresponding label image into image patches and label patches.

We created a grid for each sub-image, and then subdivided sub-images based on their corresponding grids. Figure 3.7 gives an example of how we subdivided the sub-image shown in Figure 3.5c. The size of each black square is 321×321 pixels. To utilize the contextual information, we extended each black square in up, down, left,

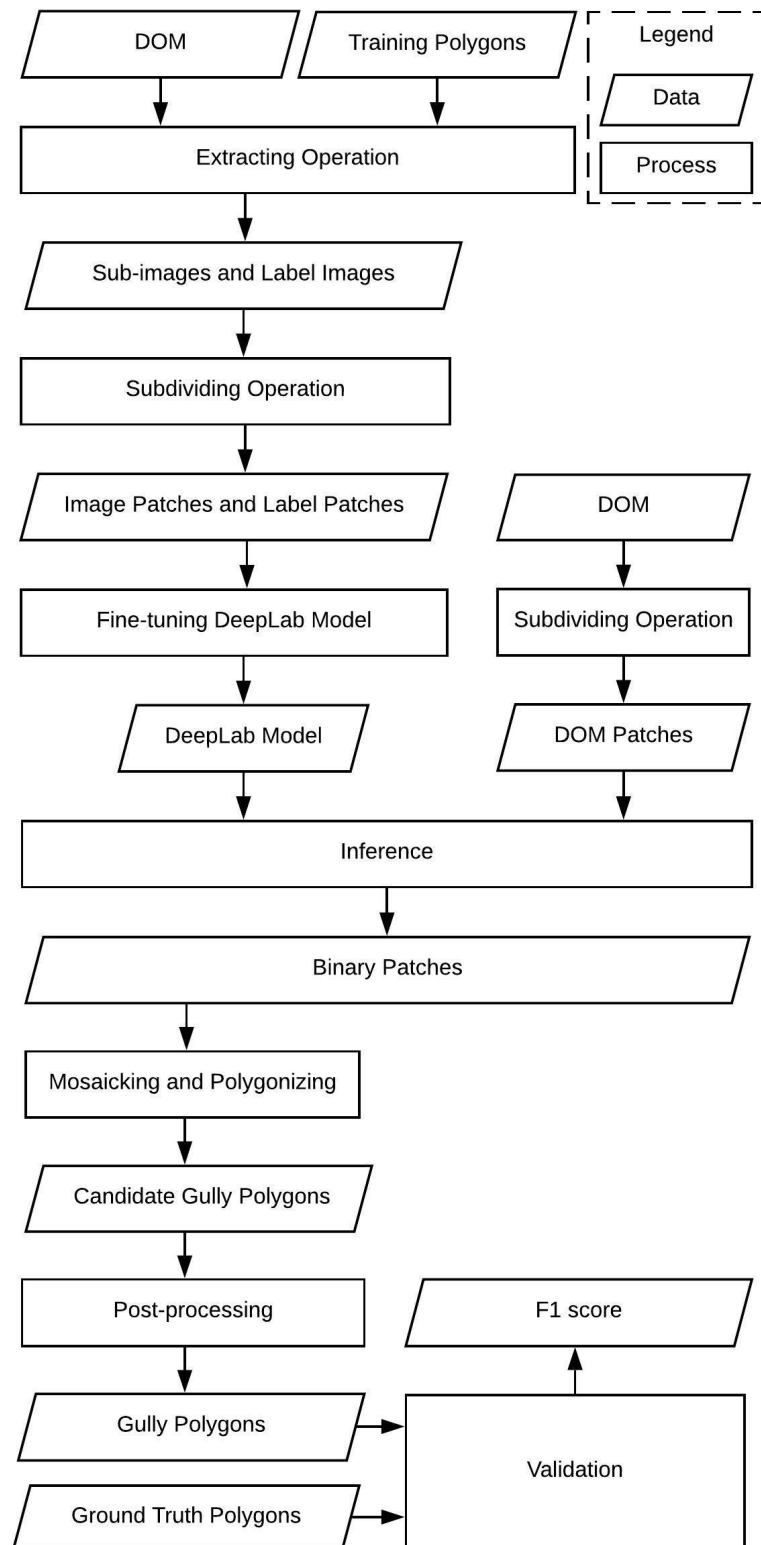


Figure 3.6: Flowchart of our mapping method based on DeepLab.

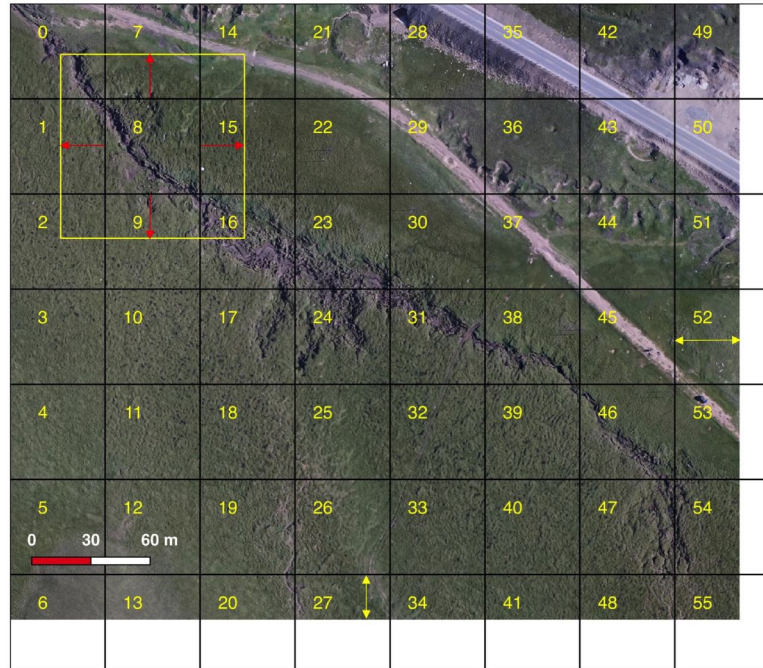


Figure 3.7: The grid for subdividing a sub-image (same as Figure 3.5c). The yellow number in each black square is the ID of the subdivided image patch. The yellow square is an example showing how we extend the boundary of a subdivided image patch (#8) from the black square to the yellow square. The yellow arrows in #52 and #27 indicate the patch width and height, respectively.

and right directions by 150 pixels (red arrows in Figure 3.7). The yellow square in Figure 3.7 shows an example of how we extended one black square (ID #8). The extending operation ensures that each patch overlaps its adjacent ones. Moreover, the overlap is necessary for producing consistent results among the adjacent patches. Then, we extracted the image patches from the sub-images based on the extended squares. In the case the image patches in the last column or row of the grid are too small (the length of the yellow double arrow is smaller than one-third of the black square), we merged them to the patches in the adjacent column (e.g., #27 into #26 in Figure 3.7) or row (e.g., #52 into #45 in Figure 3.7). We did not subdivide those sub-images smaller than 321×321 pixels and considered them as image patches directly. Lastly, we applied the same subdividing operation to label images (e.g., Figure 3.5c-L) and obtained the corresponding label patches.

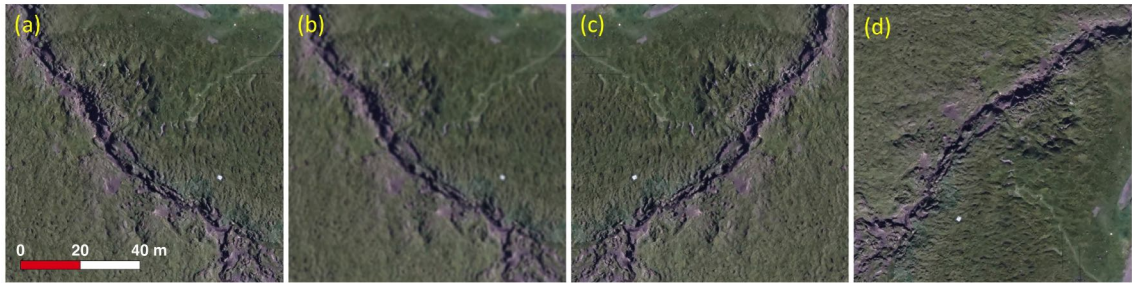


Figure 3.8: Data augmentation: (a) the patch marked by the yellow square in Figure 3.7; and (b–d) the patches after blurring, flipping left and right, and rotating 90° clockwise, respectively.

To increase the number of the training data and the generalization of the deep learning algorithm, we performed data augmentation on the subdivided image patches and the corresponding label patches. The data augmentation included flipping, blurring, and rotating (see Figure 3.8 for examples of data augmentation).

3.3.4 Mapping of thermo-erosion gullies using DeepLab

The core of our method is based on DeepLab, a state-of-the-art semantic image segmentation algorithm building on deep CNN (Chen et al., 2016). Semantic segmentation implies that the algorithm assigns each pixel in images to a specific class. We only have two classes, namely gullies and non-gullies, in the semantic segmentation task. DeepLab was developed to label specific objects (e.g., cars, cats, and dogs) on RGB images and outperforms many other deep learning algorithms (Chen et al., 2016). Therefore, we developed our method based on DeepLab. We input three-band (i.e., RGB) images to DeepLab, which can learn features automatically. However, it is unclear what features it learned (more discussion in Section 3.5.5). The network architecture we used is DeepLab-LargeFOV. All parameters in the neural network can be considered as a model.

We fine-tuned the DeepLab model by utilizing image patches and the corresponding label patches. Fine-tuning implies that we initialized the network using a pre-trained model instead of random values, and then we made small adjustments to the model in

the training process. The pre-trained model consisted of a set of network parameters that have been obtained by training with the PASCAL VOC 2012 images (Chen et al., 2016). It has already learned image features that can be used for identifying targets. Such ability is termed as transfer learning, as the features that have been learned in one setting can be exploited to another setting (Goodfellow et al., 2016). By adopting the fine-tuning strategy, we could reduce the training time and lower the requirement of training data quantity. The fine-tuning step took around three hours on one GPU (NVIDIA Quadro P5000) after 6000 iterations and reached convergence (the loss value stabilized at about 0.05).

We utilized the fine-tuned model to map thermo-erosion gullies. We subdivided the entire DOM into many DOM patches (smaller than 650×650 pixels) and performed inference on them. Inference implies that we input a DOM patch into the network with the learned parameters, and then obtain a feature map. The feature map indicates the probability of thermokarst landforms at each pixel. It took around 23 min in the inference step for all the DOM patches on GPU Quadro P5000. We converted the feature map to a binary (gully or non-gully) patch and mosaicked them into a single file for the entire study area. Lastly, we converted (polygonized) binary results to polygons using GDAL. Hereafter, we refer to these polygonized results as “candidate gully polygons”.

3.3.5 Post-processing

We set criteria based on the area and shape of thermo-erosion gullies to remove a few erroneously candidate polygons. We set an area threshold of 40 m^2 to remove polygons smaller than it. We removed the candidate polygons with $N < 40$ (N is the narrowness of a gully defined by Equation 2.1 in chapter 2). The remaining polygons after post-processing are considered as the final output, namely the mapped gully polygons (also simply termed as ‘gully polygons’).

3.3.6 Validation

We used the ground truth polygons to validate the gully polygons. We assigned each pixel on the DOM to gully or non-gully, but only gullies are our targets. Therefore, we calculated the IOU (Equation 2.2 in chapter 2) value of each gully polygons, then counted the numbers of true positives and false positives. In cases when multiple IOU values exist for one gully polygon (i.e., it intersects with several ground truth polygons), we only keep the maximum one. The value of IOU ranges from 0 to 1. A higher IOU value means a higher delineation accuracy for a given gully polygon. We set the IOU threshold as 0.4, slightly lower than the conventional threshold of 0.5 because the ground truth polygons contain uncertainties (e.g., their boundaries are wider than the truth ones). If the IOU value of a gully polygon is greater than the threshold, we count it as a true positive. Otherwise, it is a false positive. A false negative means that a ground truth polygon does not have any corresponding true positive. The number of false negatives is equal to the number of ground truth polygons minus the number of true positives. We then used these numbers to calculate the F1 score as:

$$\text{Precision} = TP / (TP + FP) \quad (3.1)$$

$$\text{Recall} = TP / (TP + FN) \quad (3.2)$$

$$F1 = 2 \times \text{Precision} \times \text{Recall} / (\text{Precision} + \text{Recall}) \quad (3.3)$$

where TP , FP , and FN are the number of true positives, false positives, and false negatives, respectively. The F1 score provides a quantitative rubric for assessing the overall accuracy of our mapped results. We also conducted a sensitivity analysis on how the delineation accuracy depends on the choices of IOU threshold (see Table 3.2). The analysis shows that this threshold is reasonable and produces the best results in terms of the overall F1 score.

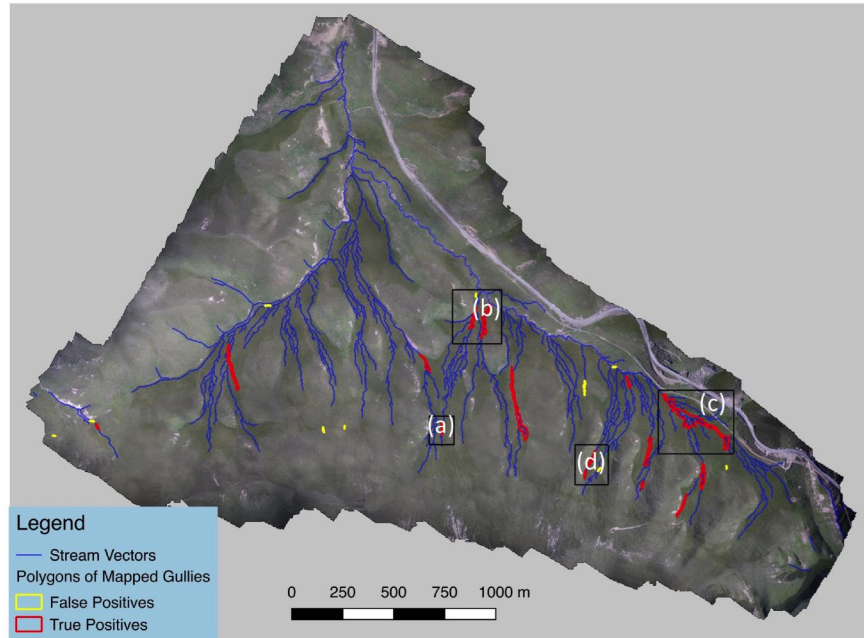


Figure 3.9: Distribution of the mapped gully polygons (the red and yellow ones are true and false positives, respectively). The blue lines are the simulated surface streams (see Section 3.5.1). The boxes (a)–(d) denote the extents of the subfigures in Figure 3.10.

3.4 Results

From the DOM, our method allowed us to delineate 27 thermo-erosion gullies (Figure 3.9). Among them, 16 are true positives and 11 are false positives. The number of ground truth polygons is 16, thus $TP = 16$, $FP = 11$, and $FN = 0$. Based on Equations (3.1)–(3.3), the precision, recall, and F1 score are 0.59, 1.0, and 0.74, respectively. Visual inspection of gullies on the DOM (e.g., Figure 3.10a–d) has shown that the boundaries of most of the gully polygons are close to the ones of the ground truth polygons. The false positives correspond to water tracks and shadows, which appear similar to thermo-erosion gullies (more discussion in Section 3.5.3).

The experiments (Table 3.3) using varying combinations of training polygons show that the highest achievable F1 score is within 0.7–0.8, which also proves the robustness of our main results. Moreover, our choice of representative training polygons outperforms all other random combinations in terms of the F1 score and false negatives. Only

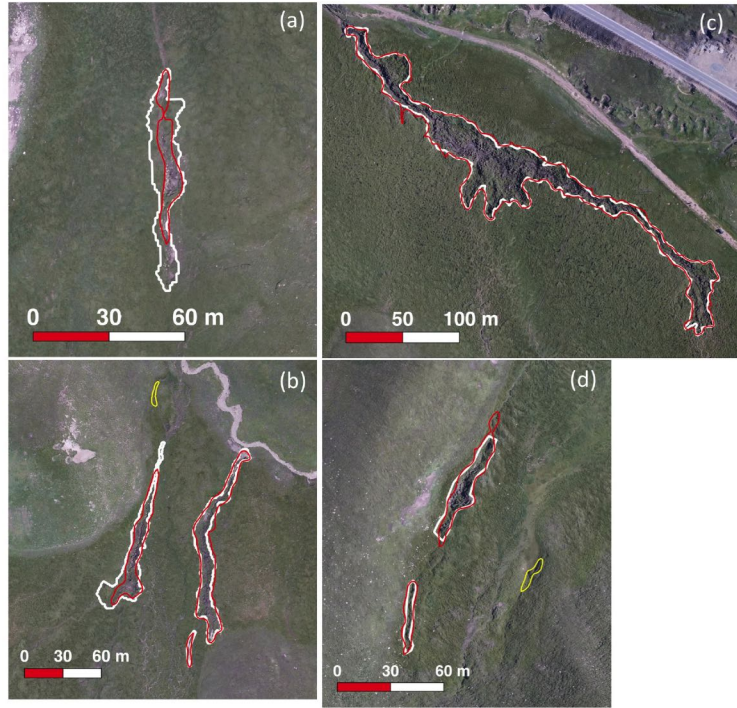


Figure 3.10: Zoomed-in comparisons between the gully polygons (red) and ground truth polygons (white). The yellow ones are false positives (same as in Figure 3.9). The extents of (a)–(d) are marked in Figure 3.9. See more discussion in Sections 3.5.2 and 3.5.3.

one experiment (#16) has a higher F1 score than our final result. However, its FN equals one, which implies that one ground truth is missed in the result. The first group of an experiment (#1) shows that using all ground truths cannot guarantee the highest F1 score. The possible reason is that a larger number (16 gullies vs. 11 non-gullies) of gully samples in the training polygons makes the algorithm more sensitive to gully-like land cover, thus the algorithm produced more false positives. The F1 scores in Groups 2 and 3 are similar, which implies that the same percentage of ground truths can result in similar accuracies.

The thermo-erosion gullies are concentrated at moderate elevations and slopes within the study area. The elevation of gully polygons (true positive) ranges from 3526 m to 3667 m (Figure 3.11a), while the elevation of the entire study area ranges from 3484 m to 3726 m. Moreover, 94% of the gullies are located on slopes gentler than 17° but steeper than 8° (Figure 3.11b), while the slope values of more than half

Table 3.2: Delineation accuracies obtained with different IOU thresholds

Threshold of IOU	0.4	0.45	0.5	0.55	0.6	0.65	0.7
Number of True Positives	16	15	14	14	13	12	11
Number of False Positives	11	12	13	13	14	15	16
Number of False Negatives	0	1	2	2	3	4	5
Precision	0.59	0.56	0.52	0.52	0.48	0.44	0.41
Recall	1	0.94	0.88	0.88	0.81	0.75	0.69
F1 score	0.74	0.7	0.65	0.65	0.6	0.56	0.51

Table 3.3: Accuracies of experiments using varying combinations of training polygons.

Group	#	TP	FP	FN	Precision	Recall	F1 Score
1	1	16	17	0	0.48	1.00	0.65
	2	12	15	4	0.44	0.75	0.56
	3	13	13	3	0.50	0.81	0.62
	4	14	12	2	0.54	0.88	0.67
	5	15	18	1	0.45	0.94	0.61
	6	13	22	3	0.37	0.81	0.51
	7	15	17	1	0.47	0.94	0.63
	8	15	15	1	0.50	0.94	0.65
	9	12	22	4	0.35	0.75	0.48
	10	15	20	1	0.43	0.94	0.59
	11	14	15	2	0.48	0.88	0.62
2	12	13	24	3	0.35	0.81	0.49
	13	13	21	3	0.38	0.81	0.52
	14	13	22	3	0.37	0.81	0.51
	15	14	22	2	0.39	0.88	0.54
	16	15	7	1	0.68	0.94	0.79
	17	13	16	3	0.45	0.81	0.58
	18	15	21	1	0.42	0.94	0.58
	19	12	8	4	0.60	0.75	0.67
	20	13	13	3	0.50	0.81	0.62
	21	15	13	1	0.54	0.94	0.68

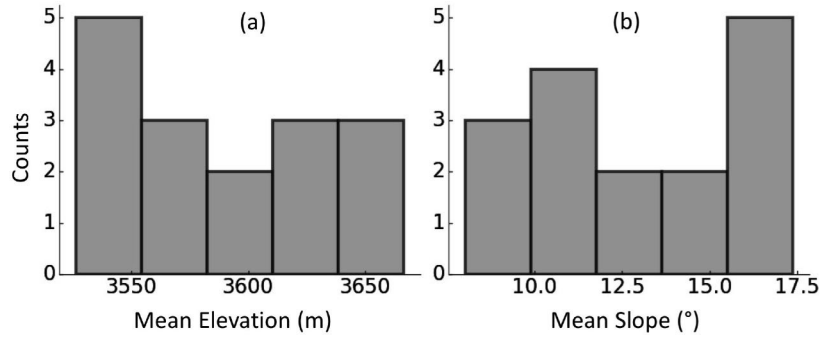


Figure 3.11: Topographical statistics of the mapped thermo-erosion gullies. (a) and (b) are statistics of mean elevation and mean slope, respectively.

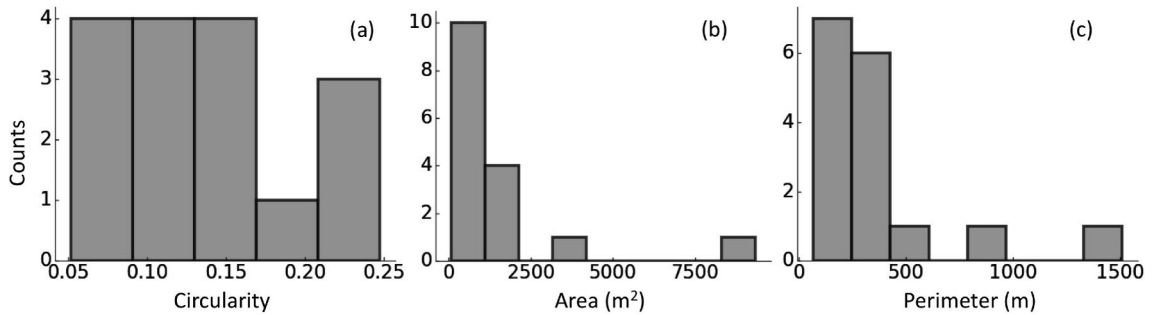


Figure 3.12: Geometric statistics of the mapped thermo-erosion gullies. (a), (b), and (c) are statistics of circularity, area, and perimeter, respectively.

(55.6%) of the study area are greater than 17° or smaller than 8°.

Their circularity indexes (namely, $\frac{4\pi S}{P^2}$) are smaller than 0.25 (Figure 3.12a). Compared to thermokarst lakes, which have been well studied, the gullies are small: 87% of them are smaller than 2050 m² (Figure 3.12b) and 94% of them have perimeters shorter than 1000 m (Figure 3.12c).

The IOU values of the true positives range from 0.41 to 0.91 (Figure 3.13) with a mean of 0.73. The minimum and maximum IOU values correspond to the gully polygons in Figure 3.10a,c, respectively.

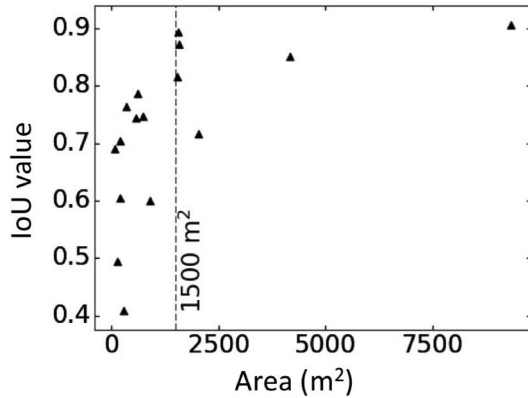


Figure 3.13: Scatter plot between the IOU values of the mapped gullies (the true positives) and their areas.

3.5 Discussion

3.5.1 Spatial distribution of the thermo-erosion gullies

Our results provide insights into the controls of gully appearance. Typically, the spatial distribution of thermo-erosion gullies in the Arctic is controlled by ice-wedge polygon networks and topographic gradient (Fortier et al., 2007). The growth of ice-wedges is not typical in the study area. Therefore, we focused on examining the topographic gradient as represented by simulated surface streams. We obtained the stream vectors as shown in Figure 3.9 from a watershed simulation based on the DEM using the Geographic resources analysis support system (GRASS) toolbox (grass.osgeo.org). Only counting the true positives, we found that all gully polygons are co-located with the simulated surface streams (Figure 3.9). Two mechanisms can result in such co-location. Firstly, water run-off heats the ground and accelerates the thawing of ice-rich permafrost. Secondly, stream erosion disturbs or even removes the vegetation and soils, which exposes the organic layer to solar radiation and leads to permafrost thawing. We also note that not all the simulated stream vectors have co-located gullies, implying that ground ice content in the near-surface permafrost can also influence the distribution. However, the exact distribution of ground ice is unknown and difficult to quantify.

3.5.2 Delineation accuracies of the true positives

The IOU values indicate high delineation accuracies for most of the mapped gullies. A low IOU value (e.g., 0.41) could be due to the difference between the microtopography observed in the field and on the DOM. In the field, we considered the collapsed ground on the gully bank as part of the gully; however, the collapse features appear subtle at the gully in Figure 3.10a as well as a few others on the DOM. Therefore, the ground truth polygons of these gullies are wider than the corresponding mapped polygons from the DOM.

The gully size affects the delineation accuracy. Among the six mapped gullies whose areas are greater than 1500 m², one has an IOU value around 0.7 and the other five have IOU values greater than 0.8 (Figure 3.13). Conversely, the IOU values of the gullies smaller than 1500 m² are lower than 0.8. Obviously, a bigger gully is easier to be identified from the DOM. However, as shown in Figure 3.13, the dependency of the IOU values on the sizes is non-linear.

3.5.3 Possible causes of false positives

The false positives are mainly delineated due to the limitations of the training data and diverse land covers in our study area. Firstly, the formation of thermo-erosion gullies involves complex thermal, hydrological, and geomorphic processes (Fortier et al., 2007; Godin and Fortier, 2010). Some of the gullies in our study area may be at an early stage of development. The training polygons we used may not include all the gullies at different development stages because we only selected the ones that we easily identified on the DOM and in the field. Secondly, the non-gully training polygons we selected may not cover all the land cover types. The study area is close to settlements. The residents and their livestock may have disturbed the land surface at some locations (e.g., vegetation damage and vehicle tracks). These anthropogenic disturbances may have been mistakenly mapped as thermo-erosion gullies because of their similar appearance

on the DOM. Lastly, as we pointed out in Figure 3.10, some water tracks, shadows, and bared land also contribute to the false positives.

3.5.4 Mapping of thermo-erosion gullies on the UAV-based DEM

We tested the capability of mapping thermo-erosion gullies on the UAV-based DEM because it is natural to use DEM data to map geomorphological features, although we wanted to solely use the three band (RGB) images. We applied the same processing chain on the DEM and obtained mapped gully polygons (as shown in Figure 3.14). In these results, we obtained the accuracy of F1 score = 0.49 (precision is 0.35 and recall is 0.81). Compared to the results solely using the RGB image, there are more false positives and false negatives. The reasons for this could be: (1) many other landforms or disturbances are similar to thermo-erosion gullies on the DEM in the study area; and (2) many erosional features (e.g., collapsed ground, ponds, and exposed soil) that are critical for identifying thermo-erosion gullies are not presented on the DEM. Further investigation on using DEM is worth exploring but was not included in this study because including DEM in the method would limit its transferability. In many other regions, collecting remote sensing images with high spatial resolution from airborne platforms or satellites is easier than obtaining or constructing a high-resolution DEM.

3.5.5 Advantages and limitations of deep learning for mapping thermokarst landforms

The most significant advantage of deep learning methods is that they can automatically learn features (LeCun et al., 2015). Hand-designed features are essential and critical in the traditional automatic mapping methods. These methods require time and expertise to design good features and choose the best combination of them. However, with deep learning methods, we can easily extend the method to other application without corresponding expertise. In this study, we only prepared the training images according to the requirement of DeepLab and adopted a network architecture from other appli-

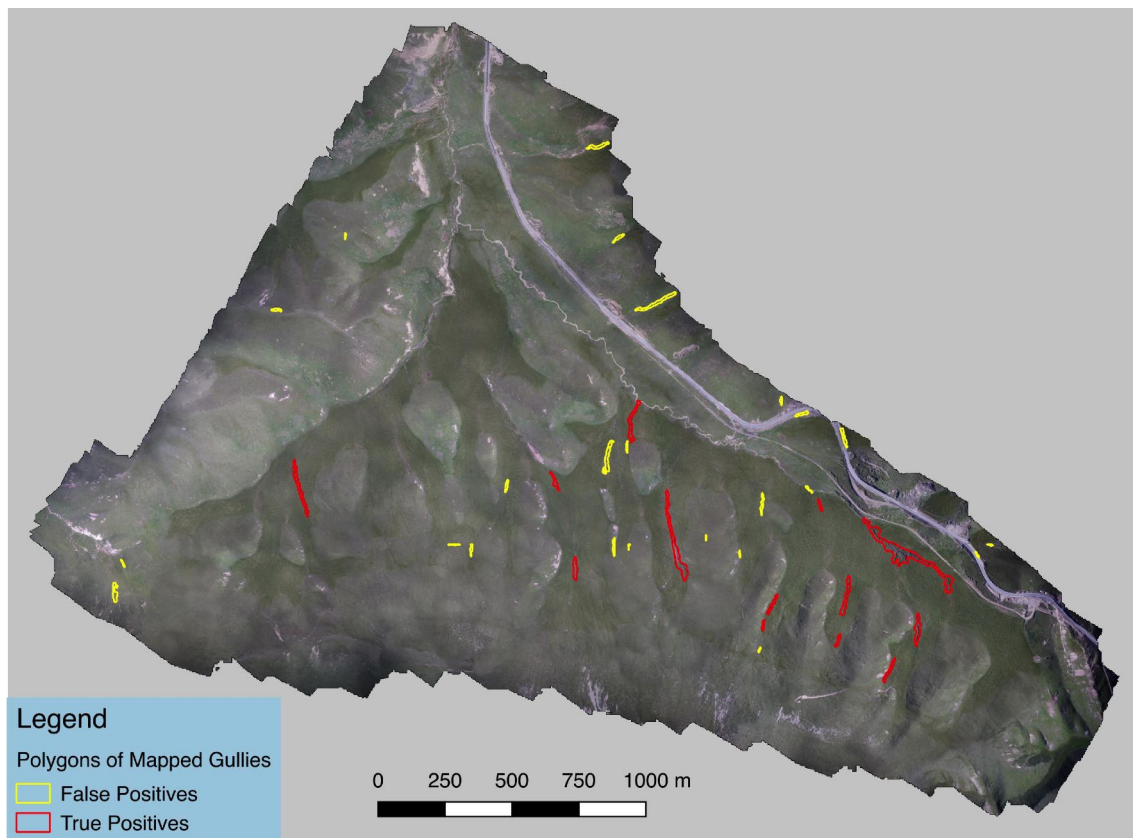


Figure 3.14: Distribution of mapped gully polygons (the red and yellow ones are true and false positives, respectively) solely using the UAV-based digital elevation model.

cation (i.e., DeepLab-LargeFOV). We did not design features or conduct experiments on different combinations of features.

Our method based on deep learning can output results close to manually identified ones. Typically, traditional automatic or semi-automatic mapping methods detect the boundaries based on the differences in the features including edge, texture, and spectral information. Consequently, these methods output results that cannot delineate the thermokarst landform due to the various spectral reflection inside it (Belshe et al., 2013; Rudy et al., 2013). A comparison (Figure 3.15) between the results obtained from GEOBIA (Chapter 2) and the ones in this Chapter demonstrates the outstanding performance of deep learning. The deep-learning-based method can delineate the landforms and acquire high IOU values (as discussed in Section 3.5.2). Conversely, GEOBIA can only detect separated portions of gullies and contain many false results.

However, many studies claim that deep learning is a black box, namely the learned features are unknown, and the factors controlling the output are unclear (Castelvecchi, 2016; Zeiler and Fergus, 2014). For instance, we used different data augmentation strategies but found that not all strategies gave the same F1 score; some even introduced more false positives (and reduced the F1 score). However, it is unclear how exactly the data augmentation strategies yield the different mapping results. Nonetheless, we need to point out that data augmentation was essential in this study as our training data were limited.

Our deep learning method did not produce exactly repeatable results. We conducted several processes of fine-tuning and inference using the same network setting and training data. However, these processes gave different, yet very similar results; and the F1 score varied between 0.7 and 0.78. Even if we doubled the number of training iterations, the F1 score was still not repeatable. We speculate that the random initialization of parameters (of input and output layers) and dropout (which is a strategy to prevent overfitting) led to this phenomenon. Moreover, the small number (16) of ground truth polygons made the F1 score sensitive to TP, FP, and FN.

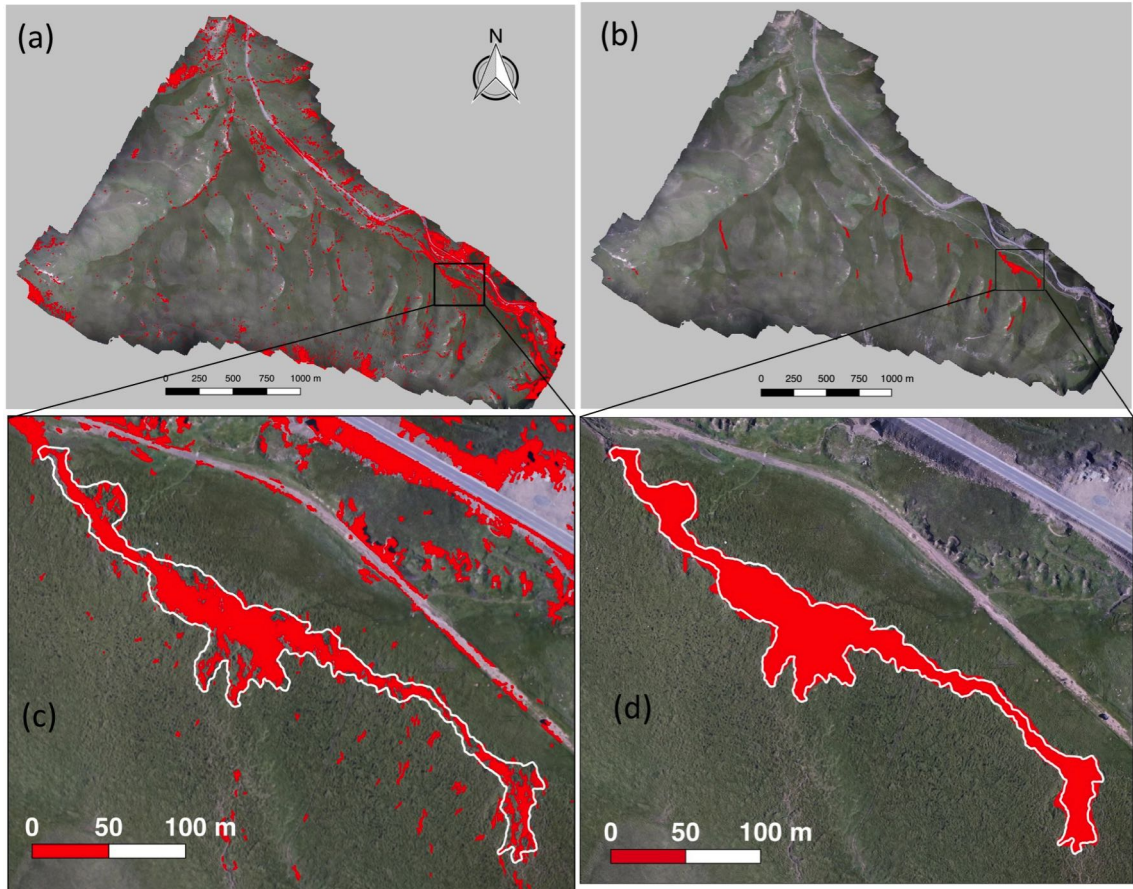


Figure 3.15: Comparison between the DeepLab-based results and those obtained from a supervised classification using support vector machine (SVM), which is a key step of GEOBIA described in Chapter 2. The mapped gullies are marked by filled red polygons on all sub-figures. (a) and (c) are the results of SVM, which contain numerous false positives. (b) and (d) are the results of DeepLab, which only contain a few false positives. The white boundary in (c) and (d) is a ground truth polygon.

3.5.6 Prospects and future work for mapping thermokarst landforms in a large area

With deep learning, the achievement of image processing has reached a new stage (Krizhevsky et al., 2012; LeCun et al., 2015). For example, identification of objects such as cats in images was challenging a few years ago, but it is much easier nowadays. Automatic mapping of thermokarst distribution in permafrost areas was regarded as extremely difficult (Council, 2014). However, our results show that it is feasible to map thermokarst landforms on remote sensing images with deep learning algorithms automatically.

Despite the great potentials, we need to make a few major improvements to the current method and training data towards mapping thermokarst landforms at regional scales such as the Tibetan Plateau. When extending the method to a large area, we need to collect corresponding high-resolution remote sensing images and training polygons. Due to the diverse types of thermokarst landforms in a large area, obtaining training data is labor-intensive. Therefore, it may require a community effort (from permafrost scientists and engineers). Variation in the size of thermokarst landforms requires images with different spatial resolution, which will increase image heterogeneities (different sources, bands, acquisition times, and spatial resolution). Moreover, a large area also means a large volume of data. To overcome these challenges, we need to innovate and improve the algorithm in the following aspects: (1) adopting state-of-the-art algorithms and trained models because deep learning methods advance very quickly; (2) utilizing multiple bands information by integrating the recurrent neural network and CNN; and (3) improving the algorithm to handle the dataset covering the large area by using multiple GPUs.

3.6 Summary

This chapter documents an automatic mapping method based on deep learning to map the thermokarst landforms from high-resolution UAV images. Despite a few false positives, we successfully mapped all 16 thermo-erosion gullies in a local area in the Northeastern Tibetan Plateau (the overall F1 score is 0.74, precision is 0.59, and recall is 1.0). The geometric characteristics and terrain analysis show that (1) these gullies are relatively small and narrowly-shaped and (2) they are co-located with simulated surface streams, confirming that the formation and development of the gullies are largely affected by the surface streams.

This study proposes a new application of deep learning and assesses the potential of automatically mapping of non-lake thermokarst landforms in a large area such as Tibetan Plateau. Moreover, products from such comprehensive mapping efforts will significantly improve observations and understanding of permafrost degradation and the corresponding environmental and socio-economic impacts.

Chapter 4

Mapping Retrogressive Thaw Slumps in Beiluhe Using Deep Learning

This chapter extends the study area to Beiluhe on the Tibetan Plateau and focuses on another non-lake thermokarst landform, that is, retrogressive thaw slumps (RTSs), but still utilizing deep learning algorithms. RTSs are among the most dynamic landforms in permafrost areas, and their formation can be attributed to the thawing of ice-rich permafrost. The spatial distribution and impacts of RTSs on the Tibetan Plateau are poorly understood. In this chapter, I innovatively applied DeepLabv3+, a cutting-edge deep learning algorithm, to Planet CubeSat images, which are satellite images with high spatial and temporal resolution. I obtain the spatial distribution of RTSs in the Beiluhe region and analyze their geometric characteristics as well as terrain variables.

4.1 Introduction

A retrogressive thaw slump (RTS) is one of many kinds of thermokarst landforms resulting from the thawing of ice-rich permafrost (Czudek and Demek, 1970; Jorgenson and Osterkamp, 2005; Jorgenson, 2013; Kokelj and Jorgenson, 2013). Several triggering mechanisms including lateral stream erosion and active layer detachments are responsible for RTSs (French, 2017). Commonly, a detachment slide removes the soil above

permafrost and exposes it to rapid thawing, then initiates an RTS. Retrogressive thawing of permafrost at the exposed headwall further expands the thawed area towards the upslope (Jorgenson, 2013). Typically, the retreat rates are 6–8 meters per year (Jorgenson, 2013). Once an RTS initializes, it can be active for decades (Burn and Friele, 1989; Lacelle et al., 2010; Swanson and Nolan, 2018; Lewkowicz and Way, 2019) and has significant impacts on the local and downslope ecosystem such as mass wasting (Gooseff et al., 2009) and increases of mercury concentrations (Pierre et al., 2018).

RTSs can occur throughout permafrost areas, but many of them are unmapped, especially those on the Tibetan Plateau. Many studies have investigated RTSs in northern and central Alaska (e.g., Swanson and Nolan, 2018; Balser et al., 2014), northern Canada (e.g., Burn and Lewkowicz, 1990; Cassidy et al., 2017; Armstrong et al., 2018; Lewkowicz and Way, 2019), and Siberia (e.g., Leibman et al., 2003; Zwieback et al., 2018). Compared with these Arctic and subarctic regions, however, the RTSs on the Tibetan Plateau have received much less investigation. A few studies focused on one or several RTSs near the Qinghai-Tibet Highway (e.g., Wang and French, 1995; Sun et al., 2017). The only regional studies to date have targeted an area along the Qinghai-Tibet Engineering Highway (Niu et al., 2014, 2016). The distribution and impacts of RTSs in large permafrost areas on the Tibetan Plateau are poorly quantified and understood. Possible reasons include (1) most of them are in remote and inaccessible regions and (2) they are similar to the surroundings or other landforms, which makes it challenging to map them from remote sensing images.

The images from CubeSats enable us to map the spatial distribution of RTSs on the Tibetan Plateau. CubeSats, small and low-cost satellites, can provide high spatial and temporal resolution images by deploying them in a multi-satellite constellation. Planet (also known as Planet Labs; planet.com) has deployed more than 150 CubeSats in sun-synchronous orbits and collects daily images of the global land surface at 3–5 m resolution. These images have great potential for earth observation and have been used in many studies, such as water body tracking (Cooley et al., 2017, 2019; Aragon et al.,

2018; Miles et al., 2018), vegetation (Houborg and McCabe, 2016, 2018), and glacier investigation (Altena and Kääb, 2017). In this study, we collect images of our study area from the PlanetScope constellation (hereafter referred to as “Planet images”), which have a spatial resolution of 3 m and are sufficient for delineating most RTSSs. The high temporal resolution of Planet images enables cloudless images to be acquired which cover the whole study area within one month, even in areas with frequent cloud cover. With the high spatial resolution, we can map many small RTSSs, including one with an area smaller than a hectare previously reported Niu et al. (2012, 2016), and accurately delineate their boundaries. These small RTSSs do not show up well on Landsat images because of its coarse resolution (30 m) although these images were used to map RTSSs in circumpolar areas (Lacelle et al., 2015; Brooker et al., 2014; Nitze et al., 2018).

To automatically map RTSSs, which is necessary for a large area, we innovatively apply deep learning algorithms to Planet images. Previous studies (e.g., Ramage et al., 2017; Lantuit and Pollard, 2008; Niu et al., 2014) combined field investigation and manual delineation on high-resolution remote sensing images to obtain RTS inventories, which are time-consuming and limited to small areas. Compared with thermokarst lakes, RTSSs are complex landforms and are difficult to automatically map on images. An RTS consists of headwall, slump floor, slump lobe, and head scarp (Lantuit and Pollard, 2008). Different parts of RTSSs have different colors on images because of various soil types, water content, incoming solar angles, and vegetation. In some regions with sparse vegetation, the colors of RTSSs are quite similar to other land covers such as bare lands. Therefore, the diverse radiometric characteristics and the similarity to their surroundings require a mapping method which has a high capability that can represent their obscure features. Deep learning outperformed other algorithms in image classification with a large margin (Krizhevsky et al., 2012) and has dramatically improved image processing technology (LeCun et al., 2015). In remote sensing applications, deep learning has also achieved outstanding results in land cover mapping, object detection, poverty estimation, and delineation of ice-wedge polygons (Jean et al., 2016; Guo et al.,

2018; Zhang et al., 2018). However, none of these studies have targeted RTSSs.

The objectives of this study are: (1) to automatically map RTSSs using Planet images, based on deep convolutional neural networks and (2) to analyze the relationship between the spatial distribution and terrain factors in the Beiluhe region on the Tibetan Plateau. We applied DeepLabv3+, one of the best semantic segmentation algorithms, to Planet images and conducted numerous experiments using different settings. By comparing with manual delineations, we calculated the accuracies of mapped results and assessed the performance of our method. We quantified their geometric characteristics of the mapped RTSSs and analyzed the relationship between their spatial distribution and terrain factors. We also discuss the advantages and limitations of using Planet images as well as the automatic mapping method. To the best of our knowledge, this is the first study on mapping landforms related to the thawing of ice-rich permafrost using CubeSat images, and will provide an assessment of deep learning applications on the Tibetan Plateau.

4.2 Study area

The study area (92.50°E to 93.51°E , 34.69°N to 35.18°N) is in the Beiluhe region on the Tibetan Plateau (Figure 4.1), with an approximate size of 5200 km^2 . The elevation ranges from 4418 m to 5320 m, with a mean of 4673 m. The records from a nearby meteorological station (93.08°E , 35.22°N) show that the mean annual air temperature and annual precipitation are -3.8°C , and around 300 mm, respectively (Luo et al., 2015). The vegetation includes alpine meadow (occupies $>45\%$ of the area) and alpine grassland (occupies $<20\%$ of the area) (Luo et al., 2015).

Most of this area is underlain by ice-rich permafrost: 70% of the area has a volumetric ice content higher than 30%, and the thickness of permafrost ranges from 20 to 80 m (Zhou et al., 2000; Luo et al., 2015). The mean annual ground temperature of the entire area is between -2.0 and -0.5°C , and the active layer thickness is between 1.5

and 2.0 m (Zhou et al., 2000; Luo et al., 2015; Wu and Zhang, 2010; Wu et al., 2015).

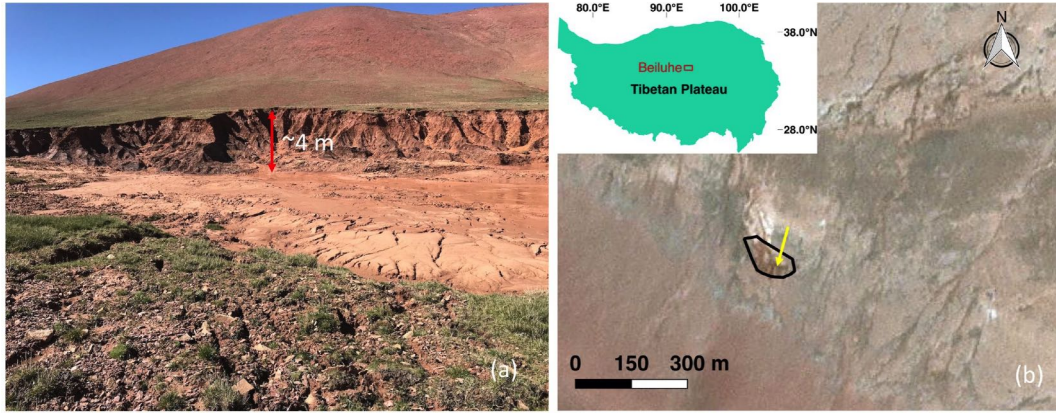


Figure 4.1: The ground photo (a) and Planet image (b) of a retrogressive thaw slump (RTS) whose central location is 92.912°E , 34.848°N . In (b), the black polygon outlines the RTS, the yellow arrow indicates the facing direction of the ground photo, and the inset shows the location of our study area on the Tibetan Plateau.

RTSs are one of the typical thermokarst landforms in this area. Figure 4.1a shows the ground photo of an RTS. Its size is about 0.9 ha and the headwall height is around four meters. Figure 4.1b shows the corresponding Planet images with red, green, and blue bands.

4.3 Methods

4.3.1 Collection and pre-processing of Planet images

We downloaded Planet images via the Planet website (www.planet.com) through its Education and Research Program. We downloaded 64 PlanetScope scenes of images (as known as Daily Imagery). Each scene covers an area of around 10 km by 30 km and has four bands (blue, green, red, and near-infrared). The acquisition dates were 22 and 23 May 2018. The product level we chose was “Analytic”, which means that the images had been orthorectified and were surface reflectance. Moreover, the bit depth and positional accuracy are 16 bit and higher than 10 m, respectively.

We pre-processed the Planet images according to the requirement of the deep learn-

ing algorithm and manual delineation. For the 64 scenes, we mosaicked and extracted red, blue, and green (RGB) bands using Geospatial Data Abstraction Library (GDAL, gdal.org), then stretched and sharpened the images using OpenCV (opencv.org). Since the deep learning algorithm (DeepLabv3+) used in this study only accepts three image bands as input, we conducted experiments to decide the best approach to extract three bands from Planet images. The candidate approaches include (1) extracting RGB bands since they are a natural color and will facilitate manual identification, (2) combining of normalized difference vegetation index (NDVI) (Rouse Jr et al., 1974), normalized difference water index (NDWI) (McFeeters, 1996), and the blue band (excluded when calculating NDVI and NDWI), and (3) adopting the first three bands after applying principal component analysis (PCA) to the 4-band Planet images. Because formation of RTSSs results in an abrupt change of land cover in vegetation and soil moisture, including NDVI and NDWI can help identify RTSSs on images. PCA uses an orthogonal transformation to re-organize the information in descending order (Wold et al., 1987). We used “Orfeo Tool Box” (Inglada and Christophe, 2009) to conduct PCA transformation then only kept the first three bands. By using PCA, we can keep the maximum amount of information on Planet images when reducing 4-band images to 3-band images. After pre-processing, we obtained a mosaic image (30916 pixels by 18713 pixels) as the input to the automatic mapping method and manual delineation. Unless stated otherwise the Planet image refers to this mosaic one in the remainder of this dissertation.

4.3.2 Collection of ground truth polygons

We manually delineated RTSSs inside the entire study area on Planet images in QGIS and conducted fieldwork to validate them. We divided the total study area into 1410 square grids using the vector-grid tool in QGIS. The size of each grid was $2.3\text{ km} \times 2.3\text{ km}$. RTSSs in each grid were independently delineated by two researchers with extensive experience of mapping RTSSs. The criteria for mapping RTSSs were based on their

distinct morphologic and tonal characteristics, including the presence of a headwall, slump floor or toe, the absence of vegetation, and the RTS shape. We cross-checked 90% of the manual results by visiting them in the field in 2014 and 2018 and all of them by visual checking from Google Earth. Around 10% of the RTSSs were difficult to reach in the field. In total, we obtained 202 polygons of RTSSs as ground truths.

4.3.3 Automatic mapping of RTSSs

Figure 4.2 shows the flowchart of our automatic mapping method. Firstly, we converted boundaries of landforms (i.e., ground truths) and a portion of Planet images to training and label images. Secondly, we trained the neural network and obtained its parameters. Next, we inputted the Planet image of the entire study area and predicted RTSSs. After post-processing, we obtained mapped polygons of RTSSs. Lastly, we validated the mapped polygons and calculated their accuracy. The details of each step are described below.

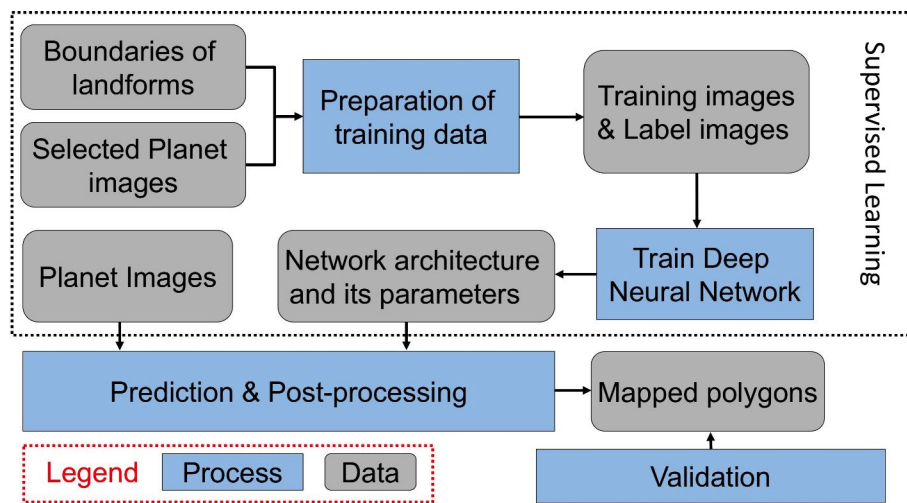


Figure 4.2: Flowchart of the automatic mapping method based on deep learning algorithms.

4.3.3.1 Preparation of training data

We derived training data by choosing all the ground truths as positive training polygons and 104 non-RTS polygons as negative ones. The non-RTS polygons cover other land

covers such as vegetation, bare land, and water bodies. To make the non-RTS polygons representative for training, we ran an initial mapping exercise only used ground truths as training polygons, then we delineated non-RTS polygons to cover areas containing numerous false positives (defined in section 4.3.3.3). It is practical to choose negative samples that are similar to RTSs. Otherwise, creating non-RTS polygons requires expertise and ground knowledge of all the land covers in the study area. Since the surrounding area of an RTS contains context information, we set a buffer area of 300 meters and then extracted a subset of Planet images (hereafter referred to as “sub-image”). Figure 4.3, 4.4, and 4.5 show the distribution and extent of the training polygons and sub-images. The sub-images only covered 6.03% (1.35% and 4.68% derived from positive and negative training polygons, respectively) of the entire study area. Furthermore, we subdivided a sub-image into patches by setting a patch size as 480 pixels with an overlap of 160 pixels. The overlap is critical to identify all pixels of one RTS that appears at several patches. We rasterized ground truth polygons then derived label images from the raster. The technical details of obtaining training images and label images are described in greater detail by Huang et al., 2018b.

To improve the quantity of training data and generalization of the mapping method, we applied data augmentation to the positive patches. Data augmentation is an approach to synthesizing training data and is necessary for this study because it can enrich our limited training data. We excluded the negative patches during data augmentation because their quantities are sufficient for training. The most common data augmentation practices include flipping, blurring, cropping, scaling, and rotating. In this study, we utilized the implementation of these methods in the “imgaug” package (imgaug.readthedocs.io). Specifically, we adopted flipping (left and right as well as up and down), blurring (gaussian blur with sigma equal to one and two), cropping (10 and 30 pixels), scaling (with factors are 0.75 and 1.25), and rotating (45, 90, and 135 degrees). Since effectiveness and methods of data augmentation depend on the application domain (Perez and Wang, 2017), we conducted a set of experiments by applying

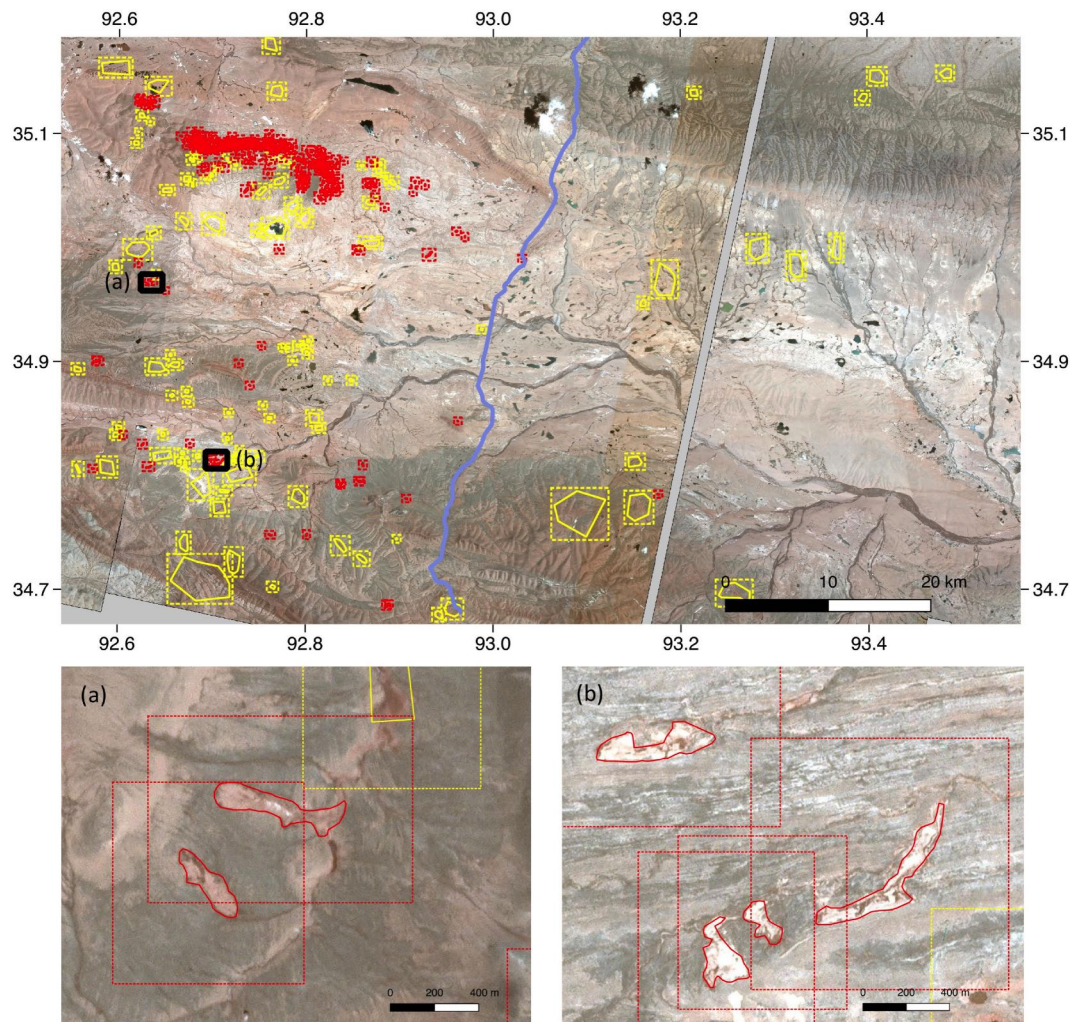


Figure 4.3: Distribution and extent of training polygons and sub-images. The red and yellow polygons are positive and negative training polygons, respectively. The red and yellow rectangles with dot lines are the corresponding sub-images. (a) and (b) are the zoom in of two small areas marked on the main figure.

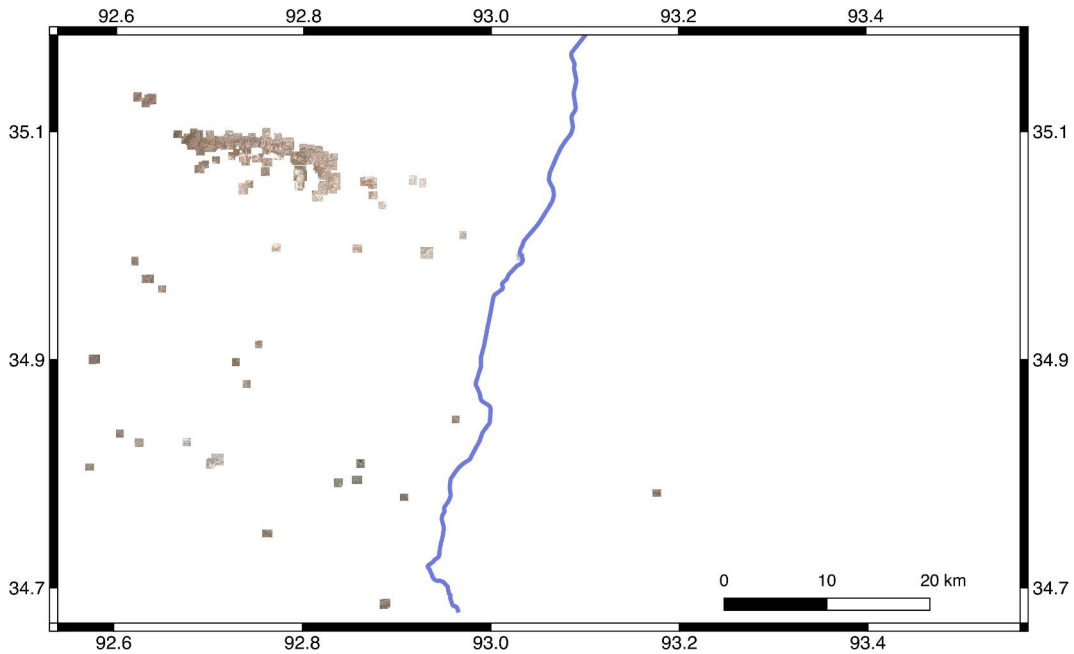


Figure 4.4: The mosaic of positive sub-images which are derived from positive training polygons.

different combinations of data augmentation practices (results will be presented in section 4.4.1). Based on the results of these experiments, we only adopted the flipping, blurring, and cropping options.

4.3.3.2 Training, prediction, and post-processing

Our automatic mapping method is a supervised learning method and built on DeepLabv3+ (Chen et al., 2018), which is a state-of-the-art deep learning algorithm for semantic segmentation. Semantic segmentation gives each pixel a class label to indicate its category on images. Similarly, our goal was to label each pixel on the Planet image as RTS or non-RTS. DeepLabv3+ is the latest version of DeepLab and outperforms (first place) many other algorithms in the PASCAL VOC image segmentation tasks (Everingham et al., 2015). DeepLabv3+ is also an open source algorithm, readily available on Github (github.com/tensorflow/models/tree/master/research/deeplab).

Training is an iterative process that makes the DeepLabv3+ network learn fea-

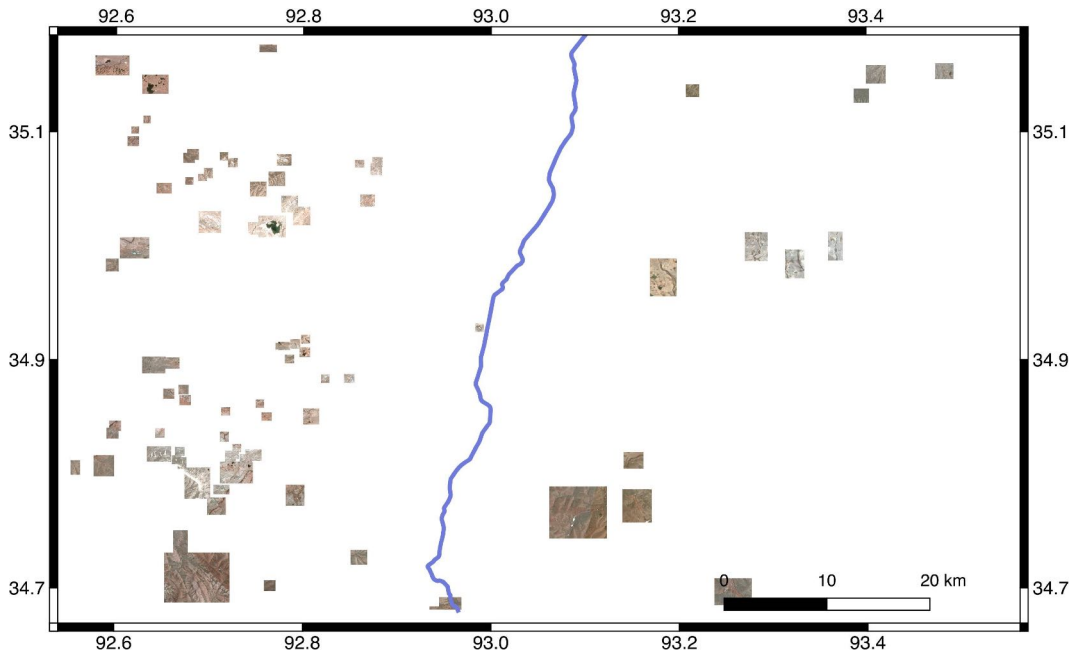


Figure 4.5: The mosaic of negative sub-images which are derived from negative training polygons.

tures from training data. The network architecture we used was Xception65 (Chollet, 2017), and the pre-trained model was based on the ImageNet datasets (Russakovsky et al., 2015). The learning rate was 0.007, and the iteration number was 30000, as recommended by the original study of DeepLabv3+ (Chen et al., 2018). We chose the best-trained model based on the value of the average precision (section 4.3.3.3). To evaluate the robustness of this algorithm, we utilized 5-fold and 10-fold cross-validation, which are commonly used in machine learning. In the 5-fold cross-validation, we randomly divided the positive and negative training polygons into five portions with a roughly equal count, and then used four portions for training and the remaining one for validation. We repeated this training process five times and present the results in Figure 4.7. Figure 4.8 shows that average precision in 10-fold cross-validation is slightly higher than the one in 5-fold, which indicates that more training data (90% in 10-fold and 80% in 5-fold) can lead to better results. To achieve the best results, we included all the ground truths in the training polygons.

In the prediction step, we divided the Planet images into many small patches and predicted the pixel categories (RTS or non-RTS) on each patch. To fit the input requirement of DeepLabv3+, we divided the Planet images into 22,582 small patches (each with a size of 480 pixels \times 480 pixels). Similar to the subdividing step in the preparation of training data, each patch had an overlap of 160 pixels with its adjacent ones. We used the trained network to predict the RTS pixels on each patch and obtained binary patches.

The post-processing includes mosaicking of the binary patches, converting to mapped polygons, and removing false polygons. We mosaicked the binary patches using GDAL, then obtained a binary mosaic. For the overlapping areas of patches, if any pixel was labelled as RTS, the pixel in the mosaic would be categorized as an RTS pixel. We converted the binary mosaic to mapped polygons using GDAL. Finally, we removed the mapped polygons with an area smaller than 0.3 ha with the consideration of the image resolution and the challenges of delineating small RTSSs.

4.3.3.3 Validation of mapped polygons

We conducted two types of validation: pixel-based and polygon-based. The pixel-based method validates the results pixel by pixel and obtains the Kappa index, and overall accuracy index. The pixel-based accuracies can be readily compared with other methods, because the pixel-based method is widely used in the classification of remote sensing images. We used “Orfeo Tool Box” (Ingla and Christophe, 2009) to conduct pixel-based validation by comparing the label raster and the binary mosaic. Specifically, the polygon-based validation is more practical than the pixel-based one since the direct input and output are the RTS boundaries. The polygon-based method compares the mapped polygons with the ground truth polygons by using the IOU (Equation 2.1 in chapter 2).

To evaluate the performance of the proposed method, we plotted the precision-recall curve, which illustrates the relationship between precision (Equation 3.1 in Chapter 3)

and recall (Equation 3.2 in Chapter 3) for different IOU thresholds. The precision-recall is a useful metric to measure the success of prediction when the number of classes are imbalanced. In this study, RTSSs occupied a small portion of the entire area and were considered as one class, while other and much larger regions were non-RTS, i.e., the other class. A high precision but low recall implies that the results contain few mapped polygons, but most of them are correct when compared to the ground truths. Conversely, a high recall but low precision implies that the results contain many mapped polygons, but most of them are incorrect. A set of good results requires high scores for both. The area under the precision-recall curve can be represented as average precision (AP):

$$AP = \sum_{i=2}^n (Recall_i - Recall_{i-1}) \times Precision_i \quad (4.1)$$

to evaluate the method, where n is the total number of thresholds for plotting the curve. A higher AP indicates better performance of a method.

4.3.4 Quantification of RTS characteristics and terrain factors

We quantified the geometric attributes of the RTSSs in the study area. Based on true positives of the mapped polygons (i.e., the mapped RTSSs), we calculated their surface areas (S), perimeters (P) and circularities (namely, $\frac{4\pi S}{P^2}$). The circularity is a metric used to represent the shape of a polygon. Its value ranges from zero to one, and a polygon close to a perfect circle has a high circularity. In contrast, the circularity value of a narrow polygon or starfish footprint has a value markedly lower than one.

To understand the relationship between the spatial distribution and environmental factors, we quantified the terrain variables of RTSSs, including elevation, slope, slope orientation, topographic position index (TPI), and potential incoming solar radiation (PISR). The digital elevation model (DEM) we used is the 30 m DEM from Shuttle Radar Topography Mission (SRTM) (Farr et al., 2007). The SRTM was conducted in

the year of 2000, while most of the RTS in the study area were triggered after 2010 by checking the historical imagery in Google Earth. Therefore, the terrain variables represent topographic conditions before the initiation of most RTSSs. We used System for Automated Geoscientific Analyses (SAGA, Conrad et al., 2015) to calculate these terrain variables. The slope, TPI, and PISR are in raster format, with the same resolution as the DEM. The values of these terrain variables are the mean value of pixels inside the extent of an RTS. We defined a line segment of each RTS with its start point in the upslope and passing through its geometric center, then calculated its azimuth as the slope orientation for the corresponding RTS. TPI is the difference between the elevation of a pixel and its surrounding defined by a specified radius (Guisan et al., 1999; Reu et al., 2013). We set the radius as 100 meters in SAGA. A positive TPI indicates that the pixel is higher than its surroundings, while a negative TPI indicates a lower location. PISR represents the received solar radiation, which can be affected by the topography and location. PISR can affect temperature, evaporation, and patterns of snowmelt (Böhner and Antonić, 2009). We calculated the daily average of PISR from May to August 2018 by setting the percentage of lumped atmospheric transmittance as 70% in SAGA. We calculated the frequencies of these terrain variables at different ranges for RTSSs and for the total study area (hereafter termed as landscape). Compared with landscapes, a higher frequency of RTSSs indicates their preferential occurrence at these ranges of terrain variables (Lacelle et al., 2015).

We quantified the characteristics and terrain factors using the mapped RTSSs and ground truths. We chose the mapped RTSSs from experiment #16 in Table 4.1 because it achieved the highest AP value. To assess the impact of false negatives and false positives in automatic mapping results, we also quantified the RTS characteristics based on the ground truths. We present the two sets of characteristics in section 4.5 and discuss the impact in section 4.6.3.

4.4 Performance of the automatic mapping method

4.4.1 Robustness of the method

The robustness of our method is illustrated by the results of numerous experiments. Table 4.1 and Table A.1 in appendix list the accuracies of using different data augmentation methods. The AP of these experiments has a small variation (0.48–0.54), indicating that the mapping method is robust. Moreover, at three IOU thresholds of 0.8, 0.4, and 0, the F1 scores (Equation 3.3 in Chapter 3) range from 0.449 to 0.653, 0.772 to 0.871, and 0.881 to 0.926, respectively. The experiments of using different portions of training polygons (i.e., 5-fold and 10-fold cross-validation) also show a small variation (0.44–0.53) in AP. Since we utilized the recommended hyper-parameters of DeepLabv3+, the only factor that would affect the performance of the method is the training data, especially the portion of training polygons and the options for data augmentation. The number of negative patches is a constant (1268) since we did not apply data augmentation to them; while the numbers of positive patches range from 343 to 4116 (experiments #0 and #31, as listed in Table A.1). Data augmentation duplicates images then flips (or other methods) them, so the number of positive patches varies when adopting different methods.

The performance of each experiment, represented by precision-recall curves, varies very little. The relation between the precision and recall at various IOU thresholds is almost linear, as indicated by the precision-recall curves shown in Figure 4.6, 4.7, and 4.8. The reason is that TP increases and FP (or FN) decreases simultaneously as the IOU threshold decreases. There are distinct steps in the precision-recall curves between recall from 0.2 to 0.6. This is because there are only a few mapped polygons with IOU between 0.1 and 0.7 (Figure 4.9).

Table 4.1: Selected experiments of data augmentations: without data augmentation (#0), the top five (#16, 4, 2, 13, and 6) and bottom five (#24, 9, 23, 25, and 20) based on AP

#	Augmentation Methods	AP	Neg	Pos	IOU	TP	FP	FN	Pre	Rec	F1
0		0.516	1268	343	0.8	93	89	109	0.511	0.460	0.484
					0.4	161	21	40	0.885	0.801	0.841
					0.0	165	17	13	0.907	0.927	0.917
16	F, B, C	0.536	1268	2401	0.8	130	66	72	0.663	0.644	0.653
					0.4	172	24	27	0.878	0.864	0.871
					0.0	175	21	7	0.893	0.962	0.926
4	S	0.531	1268	1029	0.8	120	78	82	0.606	0.594	0.600
					0.4	171	27	29	0.864	0.855	0.859
					0.0	171	27	4	0.864	0.977	0.917
2	F, B	0.523	1268	1715	0.8	121	79	81	0.605	0.599	0.602
					0.4	169	31	32	0.845	0.841	0.843
					0.0	173	27	6	0.865	0.967	0.913
13	C, S	0.521	1268	1715	0.8	131	76	71	0.633	0.649	0.641
					0.4	175	32	25	0.845	0.875	0.860
					0.0	176	31	5	0.850	0.972	0.907
6	F, R	0.519	1268	2058	0.8	108	90	94	0.546	0.535	0.540
					0.4	166	32	34	0.838	0.830	0.834
					0.0	170	28	6	0.859	0.966	0.909
24	B, S, R	0.494	1268	2744	0.8	111	77	91	0.590	0.550	0.569
					0.4	161	27	39	0.856	0.805	0.830
					0.0	164	24	15	0.872	0.916	0.894
9	B	0.493	1268	1029	0.8	107	76	95	0.585	0.530	0.556
					0.4	157	26	43	0.858	0.785	0.820
					0.0	161	22	17	0.880	0.905	0.892
23	B, C, R	0.490	1268	2744	0.8	112	76	90	0.596	0.555	0.574
					0.4	163	25	37	0.867	0.815	0.840
					0.0	165	23	17	0.878	0.907	0.892
5	R	0.485	1268	1372	0.8	84	88	118	0.488	0.416	0.449
					0.4	144	28	57	0.837	0.716	0.772
					0.0	152	20	21	0.884	0.879	0.881
20	F, C, R	0.480	1268	2744	0.8	95	80	107	0.543	0.470	0.504
					0.4	153	22	46	0.874	0.769	0.818
					0.0	155	20	22	0.886	0.876	0.881

#: experiment number, F: flipping, B: blurring, C: cropping, S: scaling, R: rotating.

AP: average precision, **Pos** and **Neg**: count of positive and negative patches, **IOU**: IOU threshold, **Pre**: precision, **Rec**: recall, **F1**: F1 score

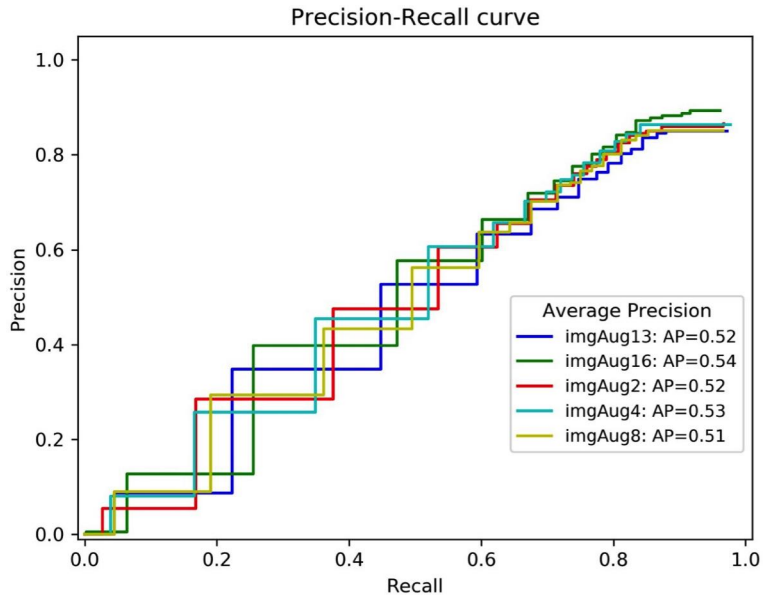


Figure 4.6: Precision-recall curves of the top five average precision (AP) in experiments of data augmentation (labeled as “imgAugX”, where X is the experiment number).

4.4.2 Mapped polygons and their accuracies

There are 196 mapped polygons in experiment #16, as shown in Table 4.1, which has the highest AP. Figure 4.10 and 4.11 show their spatial distributions and the corresponding amplifications of selected regions. With an IOU threshold of 0.5, which is commonly used, 165 of them are true positives, 31 are false positives, and 37 of the ground truths are missed, i.e., false negatives. The corresponding precision, recall, and F1 score are 0.842, 0.817, and 0.829, respectively. For the pixel-based validation, the Kappa index is 0.917 and the overall accuracy index is 0.999. As shown in Figure 4.11, the automatic-based boundaries match the manual-based ones very well, consistent with Figure 4.9, which shows that most of the IOU values are greater than 0.7. The false positives are at the locations where the land covers are similar to the RTSSs. Since some of the RTSSs are close to each other (their closest part is less than 15 m, i.e., five pixels), they were merged into one RTSS, so that the sum of TP and FN is not equal to the number of ground truths in some experiments (see Table A.1). Once a mapped polygon covers two or more RTSSs, it would be categorized as a true positive

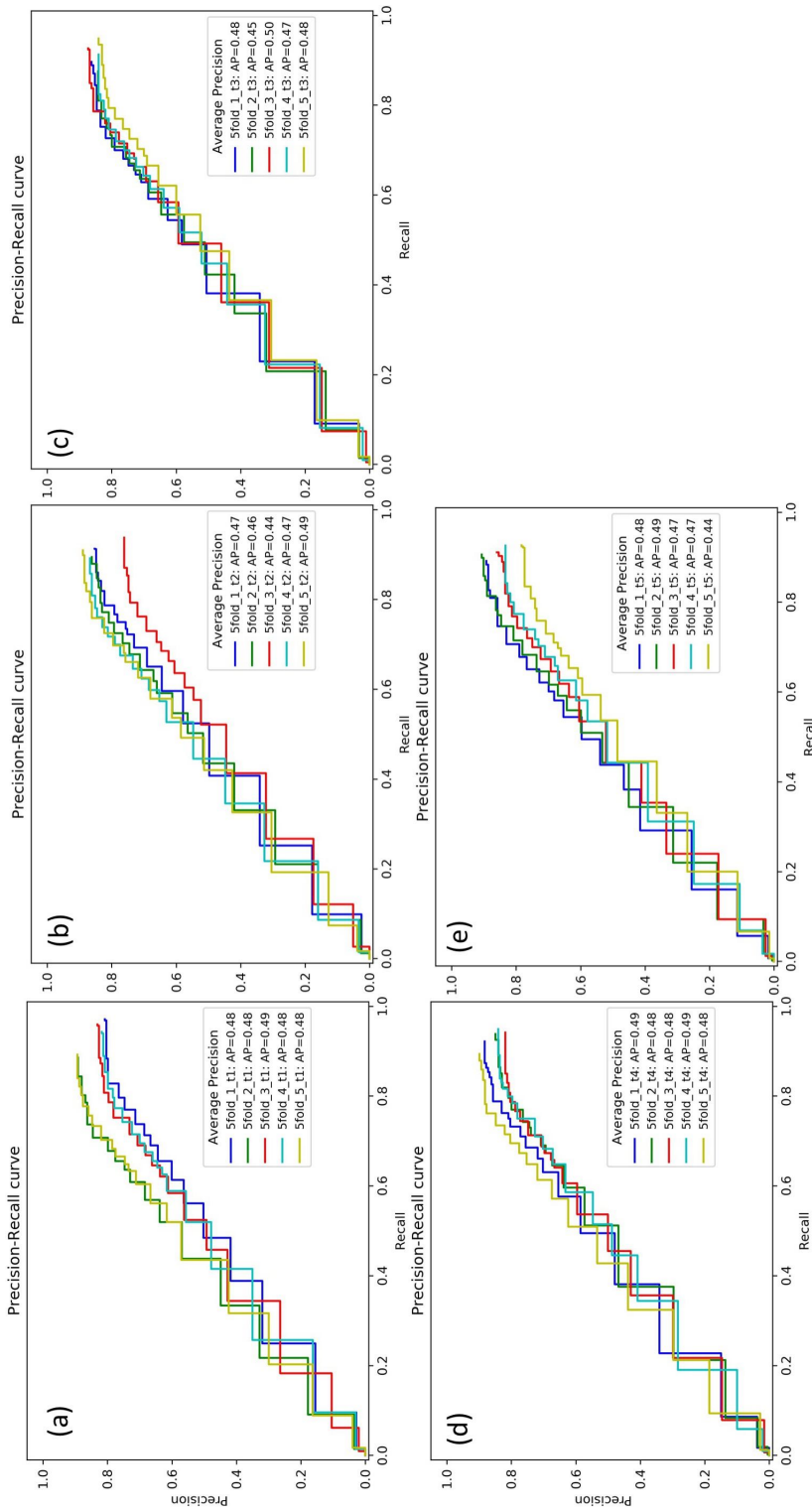


Figure 4.7: Precision-recall curves of five repeating tests applying 5-fold cross-validation. (labeled as “5fold_XtY”, indicating that the #Y experiment with the Xth fold as validation data).

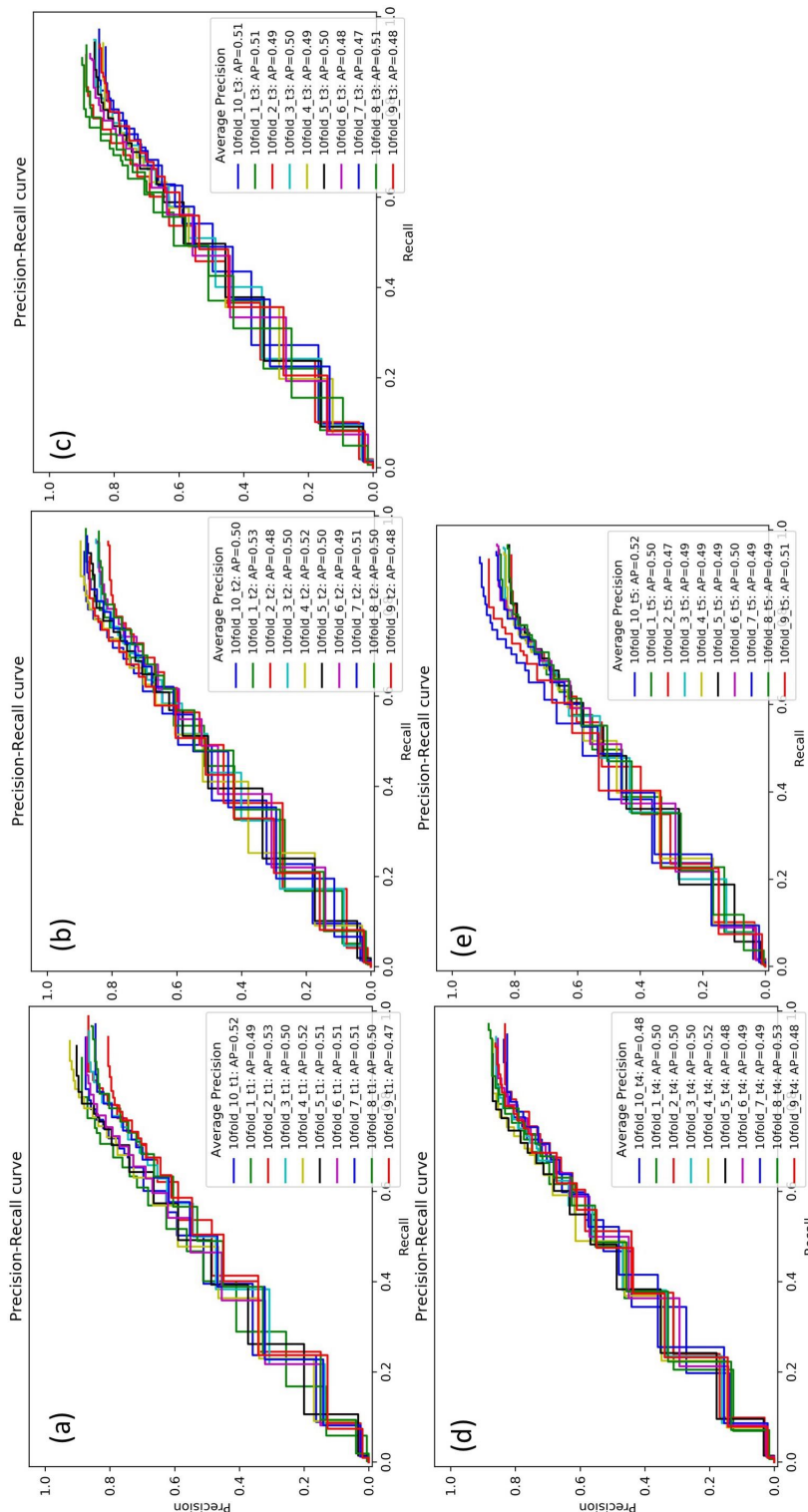


Figure 4.8: Precision-recall curves of five repeating tests applying 10-fold cross-validation. (labeled as “10fold_X_tY”, indicating that the #Y experiment with the Xth fold as validation data).

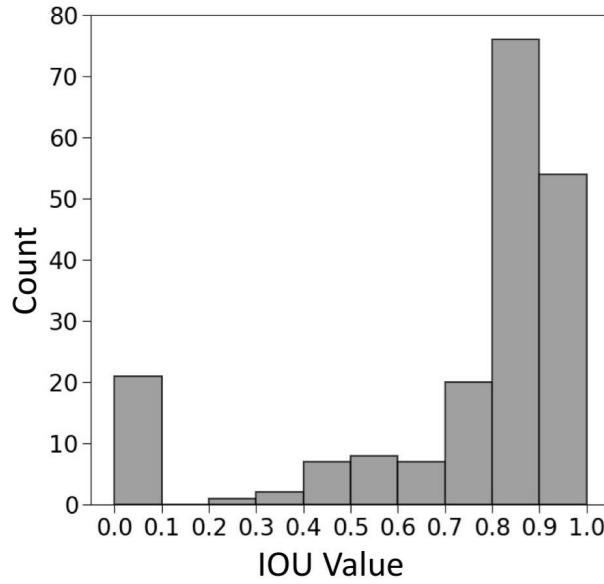


Figure 4.9: IOU histogram of the mapped polygons in experiment #16.

if its IOU value is greater than 0.5, otherwise as a false positive (examples of true and false positives are marked by red and yellow rectangles in Figure 4.11a, respectively).

4.4.3 Improvement due to data augmentation

A comparison between the experiments with and without data augmentation shows that including data augmentation can improve the IOU values of mapped polygons but introduce more false negatives. The F1 scores of experiment #0 at IOU thresholds of 0 and 0.4 are close to those obtained in other experiments, and the difference between them is within 0.05. However, when the IOU threshold is 0.8, the difference increases significantly to 0.17 (comparing #0 and #16). Moreover, all the experiments with data augmentation, except #5 have higher F1 scores than #0. Therefore, data augmentation increases the IOU values, namely, the mapped polygons better match the ground truths. Experiment #5 is a particular case in point, since rotating produced more false negatives. Lastly, experiment #0 has a relatively small number of false positives (17), which implies that the data augmentation also leads to more false positives.

Different data augmentation methods may make different contributions to improv-

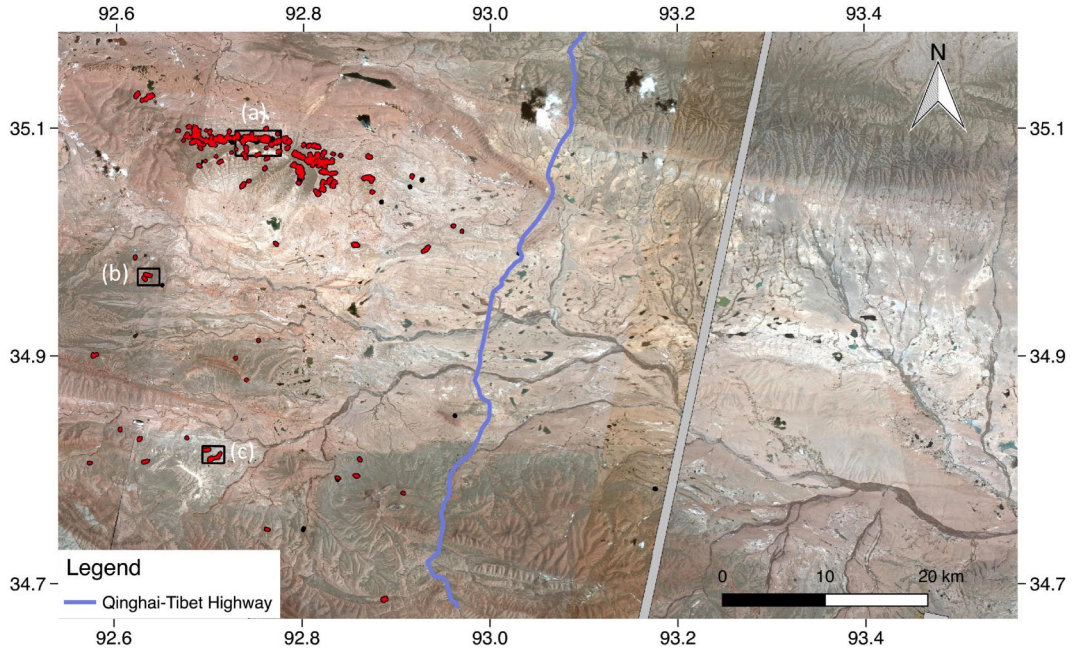


Figure 4.10: Automatically mapped retrogressive thaw slumps (red polygons) versus manual delineation (black polygons) on Planet images. The red polygons are true positives of the mapped polygons in Experiment #16. (a)–(c) are extents of the figures in Figure 4.11. The grey gap is due to the lack of Planet scenes.

ing accuracies. Table 4.2 lists the statistics on the minimum, maximum, and average of F1 scores at different IOU thresholds when adopting different data augmentation methods. When the IOU threshold is 0.8, there is a difference of F1 scores between experiments adopting rotating and other methods. The difference decreases when the IOU threshold is 0.4 and becomes negligible when it is zero.

4.4.4 Other combinations of the four bands of Planet images

The combination of red, blue, and green bands outperforms other combinations. Table 4.3 lists the accuracies of two experiments, which also adopted data augmentation of flipping, blurring, and cropping. The band combination of experiment #32 is the blue band of Planet images, NDVI, and NDWI. Experiment #33 utilized the first three PCA bands. All the experiments listed in Table 4.1 and A.1 used the RGB bands. Compared to the experiments using RGB bands, experiment #32 achieved a good AP but not

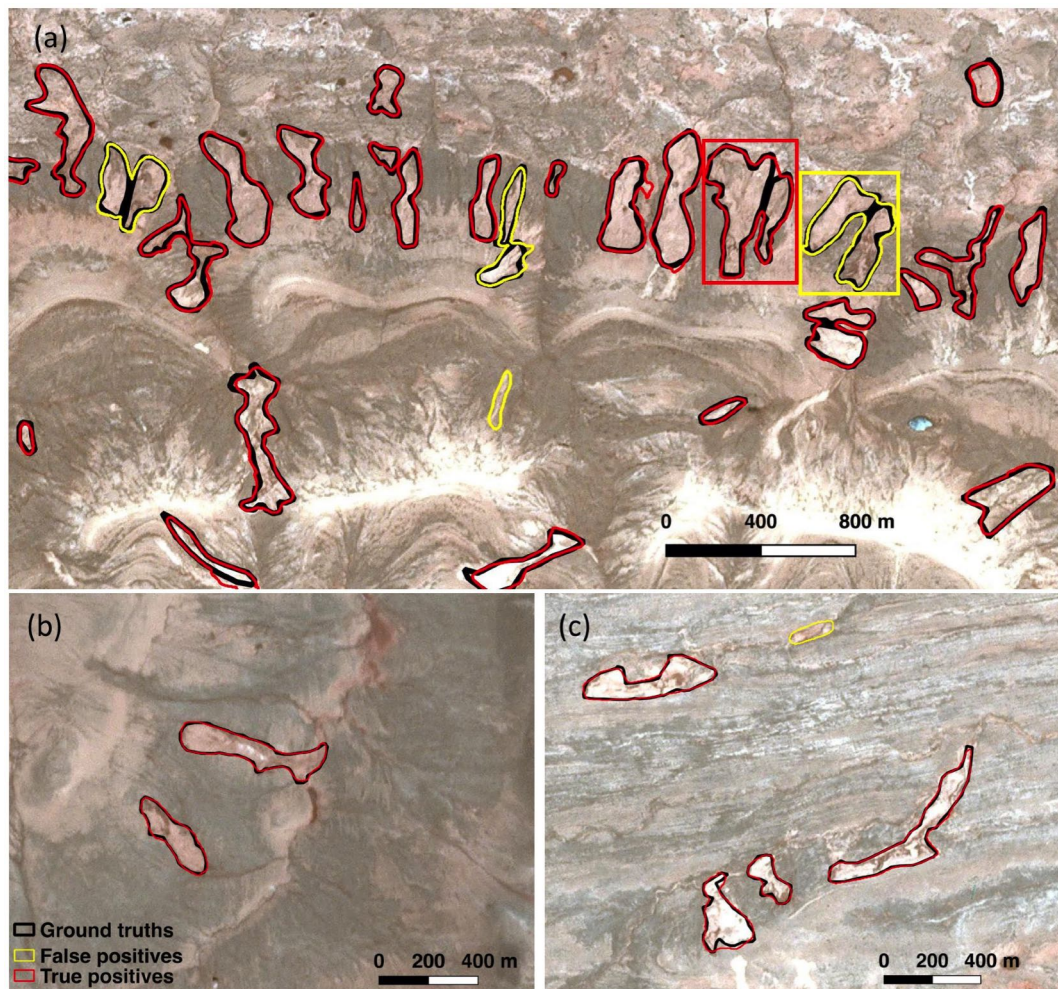


Figure 4.11: Amplifications of mapping results. (a)–(c) are amplifications of three regions marked by black rectangles in Figure 4.10. The two rectangles marked are discussed in sections 4.4.2 and 4.6.2.

Table 4.2: Statistics of accuracies based on different data augmentation methods.

IOU	Methods	F1 score		
		min	max	mean
0.8	F	0.504	0.653	0.581
	B	0.512	0.653	0.591
	C	0.504	0.653	0.597
	S	0.547	0.641	0.590
	R	0.449	0.606	0.555
0.4	F	0.818	0.871	0.842
	B	0.805	0.871	0.842
	C	0.818	0.871	0.849
	S	0.830	0.861	0.845
	R	0.772	0.861	0.834
0.0	F	0.881	0.926	0.901
	B	0.887	0.926	0.902
	C	0.881	0.926	0.904
	S	0.887	0.917	0.901
	R	0.881	0.914	0.897

the highest, while experiment #33 obtained the lowest AP. Possible reasons are (1) the training polygons were delineated on RGB images, which make the features utilized in the manual delineation and automatic mapping consistent, (2) the vegetation in the study area is sparse, so the changes in NDVI are small, (3) on the surface, water content is very high or the soil is saturated during the thaw season, which lowers the effectiveness of NDWI, and (4) after PCA, some key features for identifying RTSSs may disappear.

Table 4.3: Accuracies of other band combinations.

#	Bands	AP	IOU	TP	FP	FN	Pre	Rec	F1
32	Blue, NDVI, NDWI	0.514	0.8	129	76	73	0.629	0.639	0.634
			0.4	175	30	25	0.854	0.875	0.864
			0.0	177	28	6	0.863	0.967	0.912
33	1–3 components after PCA	0.472	0.8	109	52	93	0.677	0.540	0.601
			0.4	146	15	53	0.907	0.734	0.811
			0.0	147	14	32	0.913	0.821	0.865

4.4.5 Factors affecting the accuracies

The IOU value, which represents the delineated accuracy of an individual RTSS, can be affected by the geometric characteristics of RTSSs. The delineated accuracies are

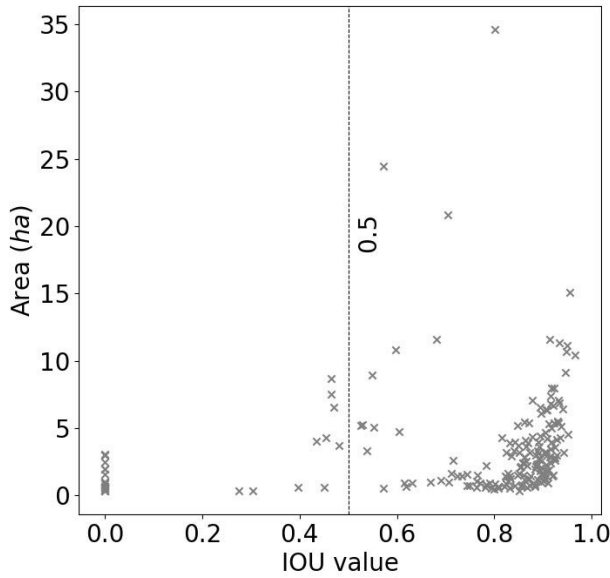


Figure 4.12: Scatter plot between the IOU values and areas of the mapped polygons (the true and false positives) based on experiment #16.

critical for analyzing the temporal change of RTS extents and the total mapping accuracies. Figure 4.12 and 4.13 are scatter plots between IOU values and areas as well as perimeters. They show that a small mapped polygon (whose area and perimeter are smaller than most of the polygons) tends to have lower IOU values, but there are also many mapped polygons with high IOU values are small in size. The IOU values do not correlate with the circularities of RTSs as shown in Figure 4.14.

As shown in Figure 4.15, the count of adjacent RTSs can affect the IOU values. The adjacent RTSs are those RTSs which have intersections with the buffer area of a central RTS. Figure 4.15 only shows the mapped polygons which cover a single RTS. The false positives are those with zero or two adjacent RTSs, and the zeros are the majority. Many high IOU values also occur where the count of the adjacent RTSs is zero. The reason could be that these RTSs share similar features which are enhanced during training. The setting of buffer areas and overlap pixels in the step of preparation of training images results in the duplication of RTS pixels. If an RTS has more adjacent RTSs, it would have more duplications in the training data. Therefore, the deep learning

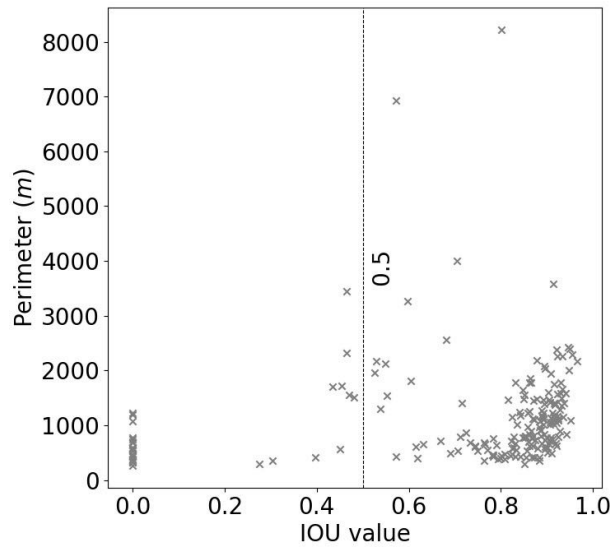


Figure 4.13: Scatter plot between the IOU values and perimeters of the mapped polygons (the true and false positives) based on experiment #16.

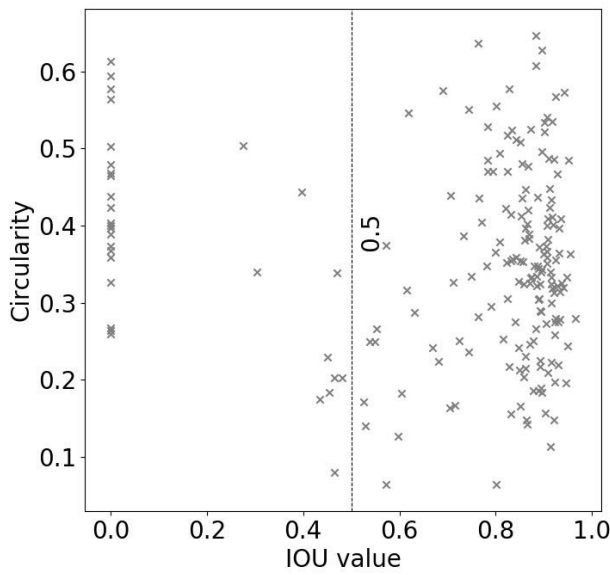


Figure 4.14: Scatter plot between the IOU values and circularities of the mapped polygons (the true and false positives) based on experiment #16.

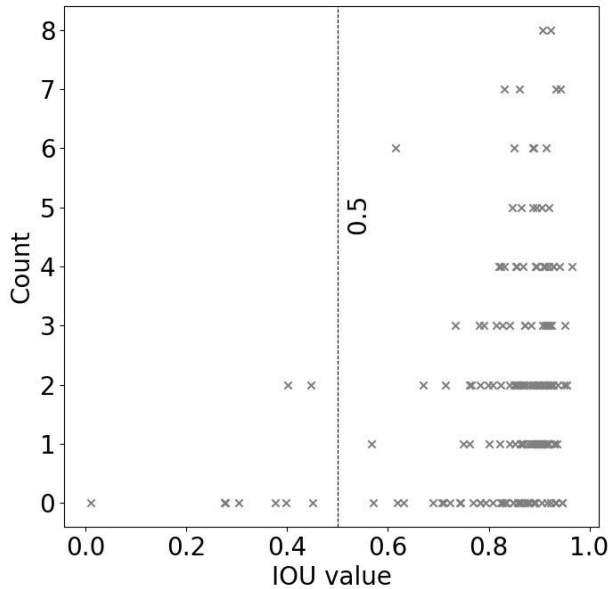


Figure 4.15: Scatter plot between the IOU values of the mapped polygons (the true and false positives) based on experiment #16 and the corresponding count of adjacent RTSSs.

algorithm learns more features of the RTS and is more sensitive to both it and similar ones.

The uncertainty of the training polygons, some of which are derived from ground truths, could also have affected the mapping accuracies. The possible uncertainties include: (1) RTSs may have been at different stages of development, but we did not distinguish between them when collecting and validating the ground truths; (2) many of the RTSs were validated in 2014, but the images were only acquired in 2018; and (3) around 10% of ground truths were used without validation in the field.

4.5 Characteristics of RTSs and their terrain factors

4.5.1 Geometric characteristics of RTSs

Figure 4.16 shows the geometric characteristics of the mapped RTSs. The areas of the mapped RTSs range from 0.3 to 34.6 ha, with an average of 3.7 ha, and 95% of them are smaller than eight ha (Figure 4.16a). Their perimeters range from 288 to 8226 meters,

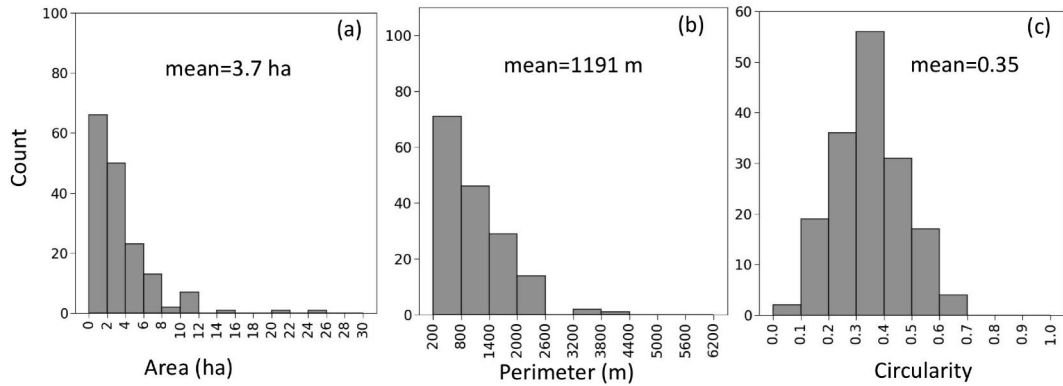


Figure 4.16: Geometric statistics of the RTSSs based on mapped RTSSs of experiment #16 in Table 4.1. One RTSS whose area is 34.6 ha not shown in (a), and two RTSSs, whose perimeters are 6924 meters and 8226 meters, respectively, are not shown in (b) because they are out of range.

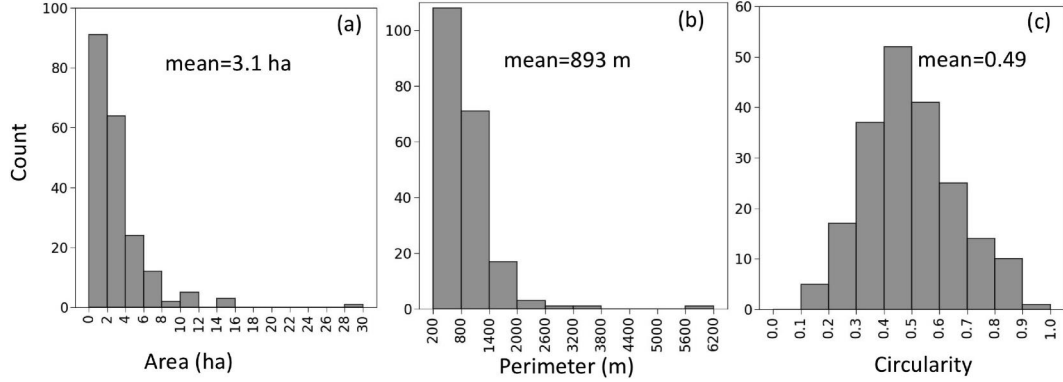


Figure 4.17: Geometric statistics of the RTSSs based on manual delineation (i.e., ground truths).

with an average of 1191 meters, and 90% of them are smaller than 2000 meters in length (Figure 4.16b). Figure 4.16c shows a nearly normal distribution of the circularities with minimum, maximum, and average of 0.06, 0.65, and 0.35, respectively.

The geometric characteristics of the mapped RTSSs are similar to those featuring as ground truths. Figure 4.17 shows that the averages of the areas, perimeters, circularities of the ground truths are 3.1 ha, 893 meters, and 0.49, respectively. The averages of the areas and perimeters of the mapped RTSSs are higher than those of the ground truths, but the average circularity is lower. These differences are possibly due to the fact that (1) many small and nearly circular RTSSs were missed in the mapped results and (2)

some of the RTSSs are close to each other and may have been merged into a single polygon, such as the one marked by the red rectangle in Figure 4.11a.

4.5.2 Terrain factors of RTSSs

Figure 4.18 shows the statistics of the mapped RTSSs in different ranges of terrain factors. Their elevation and slope range from 4639 meters to 4938 meters and from 2.4 degrees to 10.2 degrees, with an average of 4776 meters and 5.6 degrees, respectively. Figure 4.18a and b show that RTSSs preferentially occur at elevations from 4700 to 4850 meters, and on slopes from four to eight degrees. The TPI of mapped RTSSs range from -1.3 to 0.6 , with an average of -0.17 (Figure 4.18c), indicating that most of the RTSSs were initiated at a location slightly lower than their surroundings, although they are still on the slopes. The possible reasons can be found in section 4.5.3. Their daily PISR of the RTSS locations in summer varies from 8.65 to 9.04 kWh/m^2 , with a mean of 8.88 kWh/m^2 . The PISR of the entire area is between 8.50 and 9.13 kWh/m^2 , with a mean of 8.91 kWh/m^2 . Figure 4.18d shows that RTSSs preferentially occur at locations where the PISR ranges from 8.74 to 8.92 kWh/m^2 . The preferential orientations of the mapped RTSSs are north and northeast (Figure 4.18e), so that they tend to receive less incoming solar radiation than those oriented southwards.

A comparison between Figure 4.18 and Figure 4.19 shows that there is no significant difference in occurrences between mapped RTSSs and ground truths. The averages of elevation, slope, TPI, and PISR based on the ground truths are 4775 meters, 5.7 meters, -0.15 , and 8.88 kWh/m^2 . The distributions of slope orientations are similar except that the total number is reduced because some RTSSs have been missed in the mapped results.

4.5.3 Spatial distribution and the terrain controlling factors

Most of the RTSSs are in the western, particularly the northwestern section, of the study area. As shown in Figure 4.10, there is a cluster of RTSSs in the northwestern

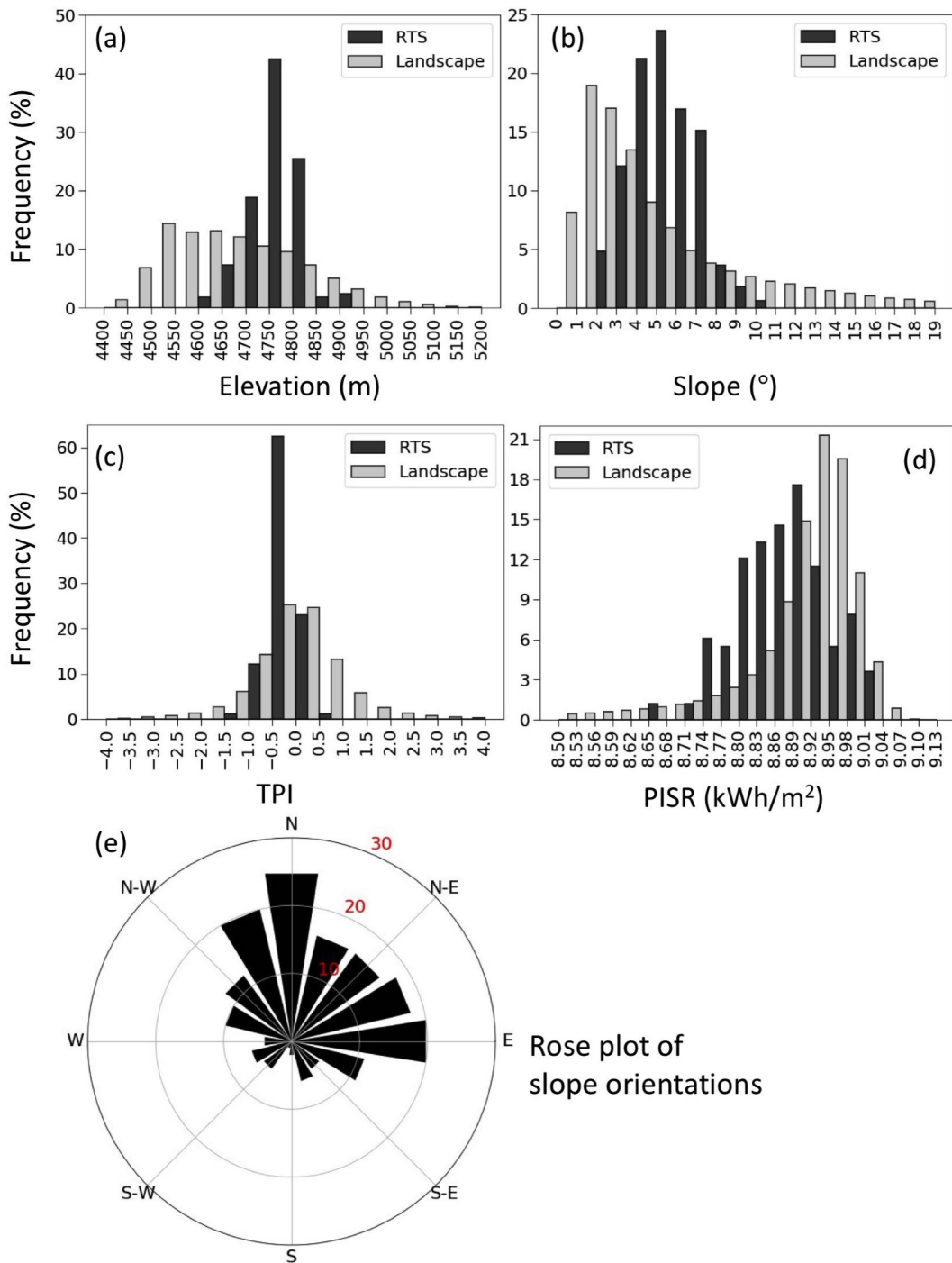


Figure 4.18: Statistics of RTS terrain factors based on automatic mapping results (#16 in Table 4.1). Landscape refers to the entire study area.

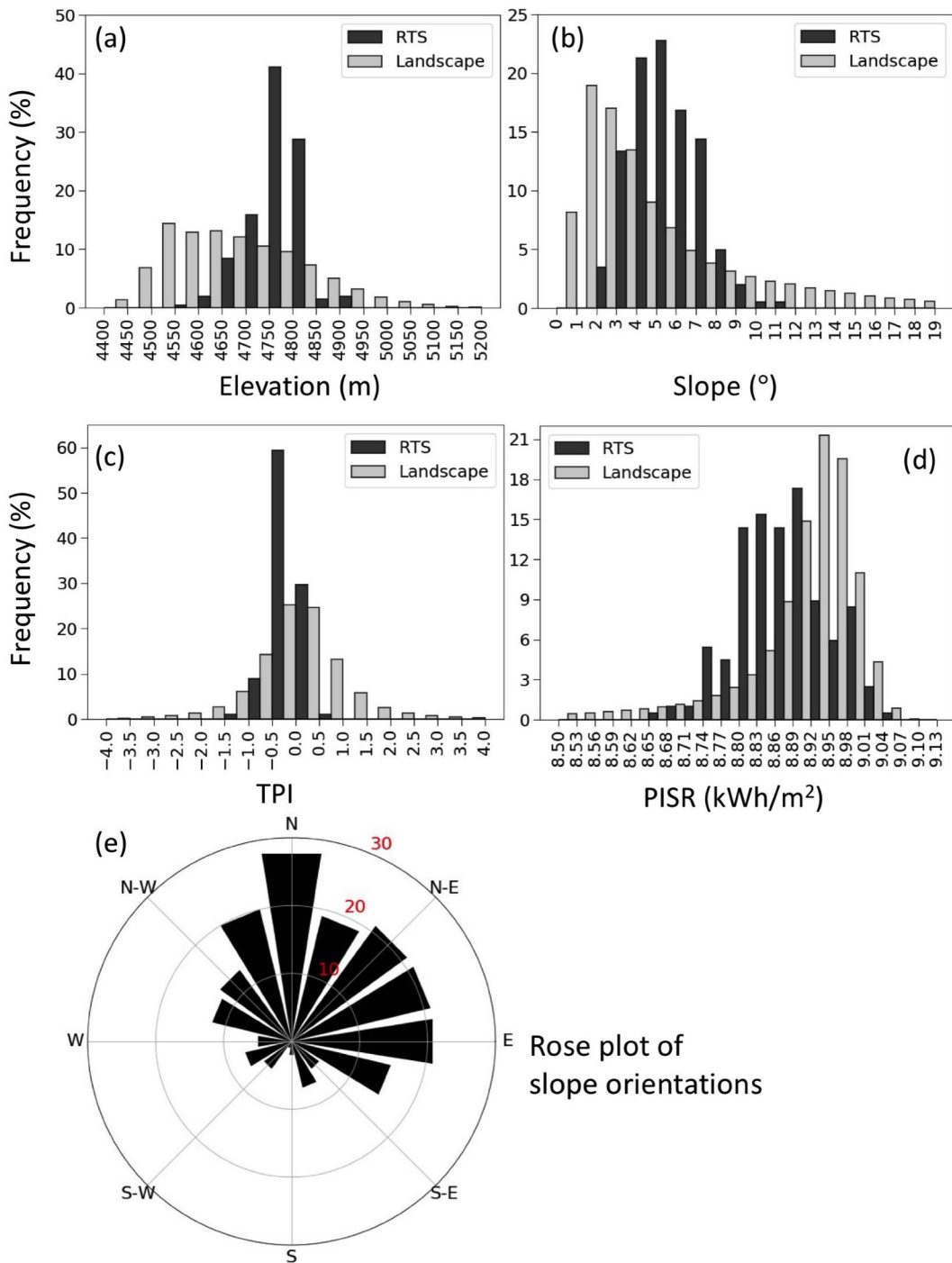


Figure 4.19: Statistics of RTS terrain factors based on manual delineation (i.e., ground truths).

region. Most of the RTSSs in this cluster are on the north-facing slope of a mountain. In our study area, north-facing slopes are cooler than south-facing ones because they received less direct solar radiation throughout the year. Many RTSSs are isolated to the west of the Qinghai-Tibet Highway. There is only one RTSS to the east of the highway. Many factors, including vegetation, soil texture, and ice context, can affect the spatial distribution of RTSSs, as well as permafrost, but these elements are beyond the scope of this study. The relationships between RTSS spatial distribution and terrain factors, including elevation, slope angle as well as orientation, TPI, and PISR are discussed as follows.

In this area, RTSSs are distributed in the locations which have a relatively high elevation. As shown in Figure 4.10, almost all the RTSSs are to the west of the Qinghai-Tibet Highway, at a higher elevation to those located east of the highway, as shown in Figure 4.20. Permafrost on the Tibetan Plateau is known as Plateau Permafrost, as its formation is mainly controlled by the elevation (Zhou et al., 2000). Therefore, elevation affects the spatial distribution of permafrost, thereby also limiting the spatial distribution of RTSSs. However, elevation is not the only factor controlling the distribution of permafrost. As a previous study has highlighted, other factors such as vegetation, aspect, and soil types can also affect its distribution (Yin et al., 2017).

RTSSs tend to occur on gentle slopes, a tendency which has been noted in many previous studies (e.g., Leibman, 1995; Niu et al., 2014; Lacelle et al., 2015). Slope condition is important, because water and melted materials from permafrost flow downward and keep the permafrost exposed to the air. In permafrost areas, a gentle slope allows water to accumulate under the active layer. The accumulation of water reduces the friction between the uppermost permafrost and the active layer, then triggers the detachment of the active layer and exposes the ice-rich permafrost (McRoberts and Morgenstern, 1974a,b). The air and solar radiation can heat ice-rich permafrost, then cause a rapid thawing.

The TPI statistics show that RTSSs are common in locations that are lower than

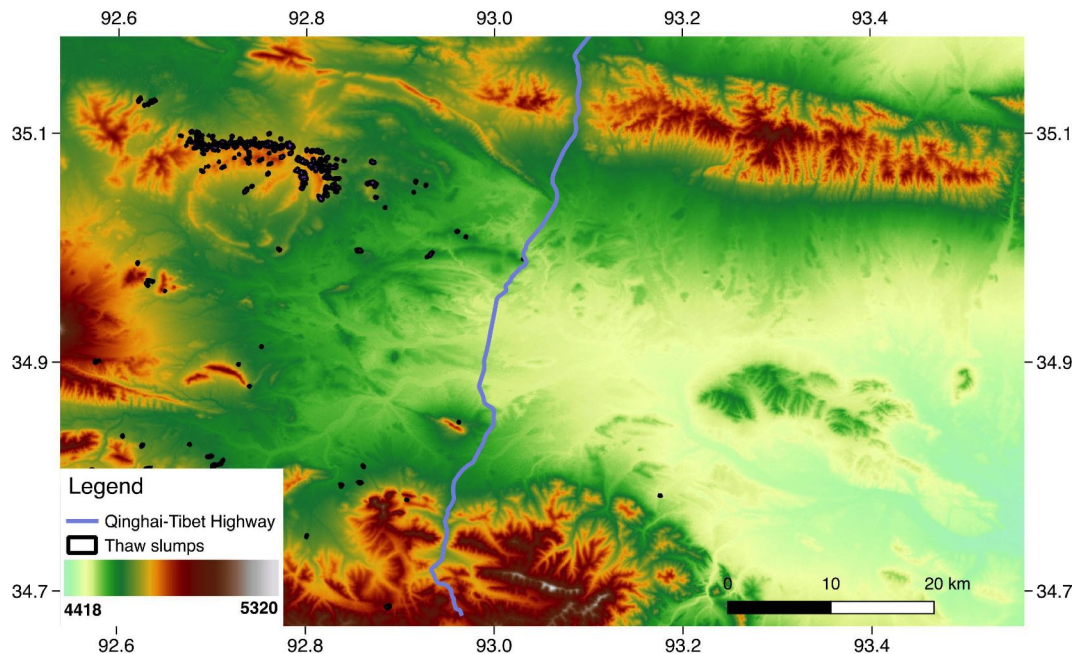


Figure 4.20: DEM and RTSSs in the study area.

their surroundings. The lower position allows water from the melting of ground ice or precipitation to easily accumulate, making it more likely to trigger the detachment of active layers. Lower positions tend to accumulate snow from precipitation and wind blow in winter. Snow cover can prevent the cooling of permafrost in the winter, which increases the likelihood that the permafrost will thaw in the next thaw season (Stieglitz et al., 2003).

Slope orientation and PISR consistently show that RTSSs preferentially exist at locations receiving less solar radiation. Less solar radiation can lead to shallower active layers, which increase the likelihood of ground ice being closer to the surface and hence more accessible to thawing. North-facing slopes may have greater snow accumulation and persistence, which can increase the soil moisture in the thaw season.

4.6 Discussion

4.6.1 Advantages and limitations of using Planet CubeSat images

Global coverage and high temporal resolution are some of the advantages of using Planet images. RTSs are the most striking dynamic landforms in the permafrost, and images with a high temporal resolution are required to monitor their temporal changes. The images from the similar sensors aboard the Planet CubeSats make the pre-processing and analysis of images a simple task with fewer uncertainties. With the advantage of high temporal resolution, we can track the highly dynamic changes of the earth's surface. The global coverage of Planet images makes it easy to extend our method to other regions for mapping RTSs without re-training.

The spatial resolution of Planet images is the main limitation, which results in the loss of many small (less than 0.3 ha) RTSs in the results. Although the Planet images have a nominal spatial resolution of 3.0 meters, their actual resolution can be lower depending on the parameters of CubeSat, such as looking angles. RTSs contain many portions including headwall, slump floor, and slump lobe. It may not be possible to distinguish between the different portions of RTSs, even those with an area greater than 0.3 ha. Moreover, if the temporal changes of the RTS are smaller than one pixel of Planet images, then they cannot be identified. Most of the stabilized thaw slumps are drier and covered by new vegetation, much like their surroundings, which makes it challenging to identify them.

4.6.2 Advantages and limitations of the automatic mapping method for RTSs

The automatic mapping method can potentially be applied to a large area such as the Tibetan Plateau, and allows us to map RTSs to an unprecedented extent. Many permafrost areas remain unmapped because (1) they are challenging to reach and (2)

manually mapping on high-resolution images is labor-intensive. Automatic mapping methods can overcome this issue. In this study, we utilized the images of around 6% of the study area for training, then mapped the entire area. Similarly, we can collect training data in several case studies, and then map RTSSs on the entire Tibetan Plateau. Furthermore, with the automatic mapping results in a large area, we can analyze the numerous RTSSs simultaneously, which may provide important new insights into their characteristics, impacts, and controlling factors.

Transfer learning, which is the intrinsic advantages of deep learning, enables us to apply the same method to other regions. If the sources of images and targets are the same as this study, we can apply our method directly. Otherwise, we need to fine-tune the model using the corresponding training data.

As a supervised learning method, the training process is time-intensive and requires the adjustment of hyper-parameters. It took around 10 hours to train the network by utilizing two mainstream GPUs, which is longer than many traditional methods such as support vector machines. Many hyper-parameters need to be assigned before training. The most important one is the learning rate, which controls the steps of model adjustment. A higher learning rate can lead to loss explosion and crash of the training process. Once the training process crashes, we have to restart it. Restarting the training may overcome the crash issue because the initiation of input and output layers is random. A lower value of learning rate requires a much longer period of training.

The performance of the methods depends crucially on the quantity and quality of training data. The neural network used in this study requires a large volume of training data. Moreover, erroneous labels in training data can result in erroneous features for the method. The balance of training data is also important, because more training data for a specific class can make the method more sensitive to this class. Although the method can learn features automatically, it is unclear what features it learns because of its black-box nature.

Another limitation of this method is that it cannot distinguish between two or more

RTSs if there are close to each other, as shown in Figure 4.11. The reasons could be: (1) the deep learning algorithm, that is, DeepLabv3+ is not good at capturing the edges of the targets when they are too close; and (2) the merging processing of inference patches gives a higher priority to the RTS pixels than non-RTS pixels.

4.6.3 Comparison between the mapped polygons and ground truths

Automatic mapping of results using remote sensing images is less accurate than manual delineation on images or in the field. By comparing the geometric characteristics as well as statistics of terrain factors (Sections 4.5.1 and 4.5.2) derived from automatically mapped RTSs and manual delineation (i.e., ground truths), we can conclude that they have a very high similarity. But even manual delineation requires validation, due to the uncertainties of remote sensing images. Therefore, we can still use the automatic mapping results for further analysis or updating existing maps, especially in the region where the manually delineated results are unavailable or outdated.

The accuracies of mapped polygons can be higher if we adjust the criteria for removing false results or choose other IOU thresholds as shown in Table 4.1. A total of 37 RTSs were missed in experiment #16, but if we lower the criteria for removing false polygons and set the IOU threshold as zero, only one of them would have been missed. In some of the experiments, not a single RTS was missed when the IOU threshold was zero, as shown in Table A.2 in the appendix. Different tasks could have different mapping purposes. For example, if the mapping goal is to find the locations of RTSs, a lower threshold of IOU is a good choice. If we lower the threshold of removing small mapped polygons, we may achieve results without false negatives. For a region without ground truths, we cannot apply the IOU threshold. A practical approach for achieving satisfying results is to lower the criteria for removing false polygons, then to manually check the mapped polygons on the images.

4.6.4 Future work

Combining other sources of satellite images such as Landsat or Sentinel-2 with Planet images is the key to improving the mapping results and extending them to large areas. Using high-resolution remote sensing images will face the challenges of a large dataset. Landsat images are valuable for detecting landscape dynamics and mapping RTSSs in large permafrost areas (Nitze and Grosse, 2016; Nitze et al., 2017, 2018), but they only target RTSSs with a large surface area (e.g., Brooker, 2014). With Landsat images, we can first identify the locations of RTSSs, and then delineate the boundaries of RTSSs on Planet images. Since RTSSs are usually isolated, we can reduce the volume of Planet images required by restricting our coverage to their immediate vicinity. Landsat or Sentinel-2 have more than seven bands, which also may help reduce false positives.

We need to improve the deep learning algorithm to utilize the four bands of Planet images and overcome unsatisfying results. Because DeepLabv3+ only accepts three bands, we conducted experiments in which we used different combinations of the four bands, but other combinations did not outperform the one using RGB bands. Usually, more image bands contain more information, indicating that we did not utilize all the bands in an optimized approach. We should improve the current algorithm or adopt other advanced deep learning algorithms to fully utilize the four bands. The issue of the mapped polygons covering multiple RTSSs also needs to be solved by improving the deep learning algorithm and post-processing.

4.7 Summary

In this chapter, a deep learning algorithm, DeepLabv3+ was applied to Planet CubeSat Images for automatically mapping retrogressive thaw slumps in the Beiluhe region on the Tibetan Plateau. Numerous experiments show that our method is robust. The experiments with the highest average precision (0.536) contains 196 mapped polygons. Of these 196 results, 165 are true positives, and 31 are false positives when the IOU thresh-

old is 0.5, and the corresponding precision, recall, and F1 score are 0.842, 0.817, and 0.829, respectively. Most (95%) of the mapped RTSSs are smaller than eight ha, and 90% of their perimeters are smaller than 2000 meters. The comparison between the statistics of true positives and manual delineations shows that automatically mapped results show similar statistics to manual ones. Analysis of the terrain factors indicates that (1) the RTSSs preferentially occur in the locations with gentle slopes (four to eight degrees), (2) the locations where the RTSSs are initiated tend to be lower than their surroundings, suggested by the statistics of TPI values whose mean is -0.17 , and (3) RTSSs are more likely to develop in locations receiving less solar radiation (i.e., north-facing slopes). This study demonstrates that the method can automatically map RTSSs on Planet images, and offers a invaluable approach to mapping RTSSs on the Tibetan Plateau.

Chapter 5

Temporal Changes of Active Layer Detachments and Retrogressive Thaw Slumps in Beiluhe

Investigating the development of non-lake thermokarst landforms and its controlling factors is imperative to improve the understanding of permafrost degradation, which is the next step of mapping exercises. In this chapter, I use multi-temporal high-resolution images to investigate the temporal changes of active layer detachments and retrogressive thaw slumps. The preliminary results show that rapid development of retrogressive thaw slumps from 2010 to 2012 and the possible triggering factor is the timing of snow cover in winter. However, this is a preliminary study and requires thorough quantitative investigation and further analysis of external controlling factors.

5.1 Introduction

Active layer detachments (ALDs) and retrogressive thaw slumps (RTSs) are slope failures in permafrost areas. An active layer detachment is a localized slope failure that is confined to the active layer (French, 2017). ALDs contain detached active layer as well as the overlying vegetation mat, and their whole failure planes are within the

slope. Most ALDs are compact or elongated morphological features, appearing as linear gashes on the slope (Lewkowicz and Harris, 2005; Krieger, 2012). RTSs have been described in detail in section 4.1 of Chapter 4. Usually, ALDs are smaller than RTS in surface area, and the height of RTS headwall is much larger than the depth of ALDs (Wolfe et al., 2001; Krieger, 2012). The slump scar or hollow of an ALD is less than one meter in depth (French, 2017).

ALDs and RTSs are dynamic landforms in permafrost areas. ALDs can initiate and develop within a few hours or days, and the velocities of their propagation to downslope are a few meters per hour (Lewkowicz, 2007). Compared with ALDs, RTS development spans a much longer period. An RTS can be active for decades; and typically, its retreat rate is 6–8 meters per year (Jorgenson, 2013). The maximum retreat rate can be greater than 10 meters per year (e.g., 16 m yr^{-1} reported by Burn and Friis, 1989) or even larger (e.g., 38 m yr^{-1} reported by Swanson and Nolan, 2018). The formation of an ALD can expose the underlain ice-rich permafrost, therefore, an ALD could convert to an RTS if the thawing continues (French, 2017; Krieger, 2012). The development of ALDs and RTSs is controlled by many factors, including the timing of snow cover, warmer air temperatures, and summer precipitation (e.g., McRoberts and Morgenstern, 1974b; Balser et al., 2014; Lewkowicz and Way, 2019).

Both ALDs and RTSs are common in the polar region and on the Tibetan Plateau. In the Arctic and subarctic, many studies investigated the developments of RTSs using remote sensing images as well as field measurement (e.g., Lantuit and Pollard, 2008; Lantz and Kokelj, 2008; Lacelle et al., 2010; Brooker et al., 2014; Lacelle et al., 2015; Segal et al., 2016). However, on the Tibetan Plateau, only a few studies focused on the development of individual RTSs next to Qinghai-Tibet Highway (Niu et al., 2005, 2012; Sun et al., 2017).

To quantify RTS dynamics and the associated controlling factors on the Tibetan Plateau. We utilized historical images from Google Earth (referred to as Google images thereafter) and the SPOT-5 satellite (referred to as SPOT-5 images thereafter) to quan-

tify temporal changes of RTSs near Beiluhe in central Tibet. This study only focuses on RTS development because the fast development of ALDs cannot be captured by these images. By integrating data from the nearest meteorological station and snow cover products from Moderate Resolution Imaging Spectroradiometer (MODIS) satellites, we analyzed the external controlling factors for RTS triggering and developing. This is one of the few studies to provide a quantitative investigation of RTS development in a regional scale on the Tibetan Plateau.

5.2 Data and methods

5.2.1 Study area

The study area (92.604°E to 92.877°E , 35.012°N to 35.118°N) is in the Beiluhe region on the Tibetan Plateau as shown in Figure 5.1. More information about the study area can be found in section 4.2 of Chapter 4. We focused on this study area because within it a cluster of RTSs was shown in the mapping results of Chapter 4.

5.2.2 Collecting and processing remote sensing images

High-resolution (finer than three meters) images are necessary to delineate RTSs. The typical retreat rates of RTSs are only a few meters (Jorgenson, 2013), which cannot be represented by relatively low-resolution images such as Landsat images with a spatial resolution of 30 m. Therefore, to accurately delineate the RTSs boundaries and investigate the RTS development, we utilized high-resolution images from Google Earth and SPOT-5 satellite (listed in Table 5.1). By inquiring the image information on DigitalGlobe website (discover.digitalglobe.com), the images from Google Earth were acquired by GeoEye-1 and IKONOS-2 satellites. The 2012 Google image is a mosaic of images acquired in November and December. We downloaded the images using “LocaSpace Viewer” (www.locaspace.cn). During the downloading process, the resolution was set as one and two meters for images covering the study area and the entire

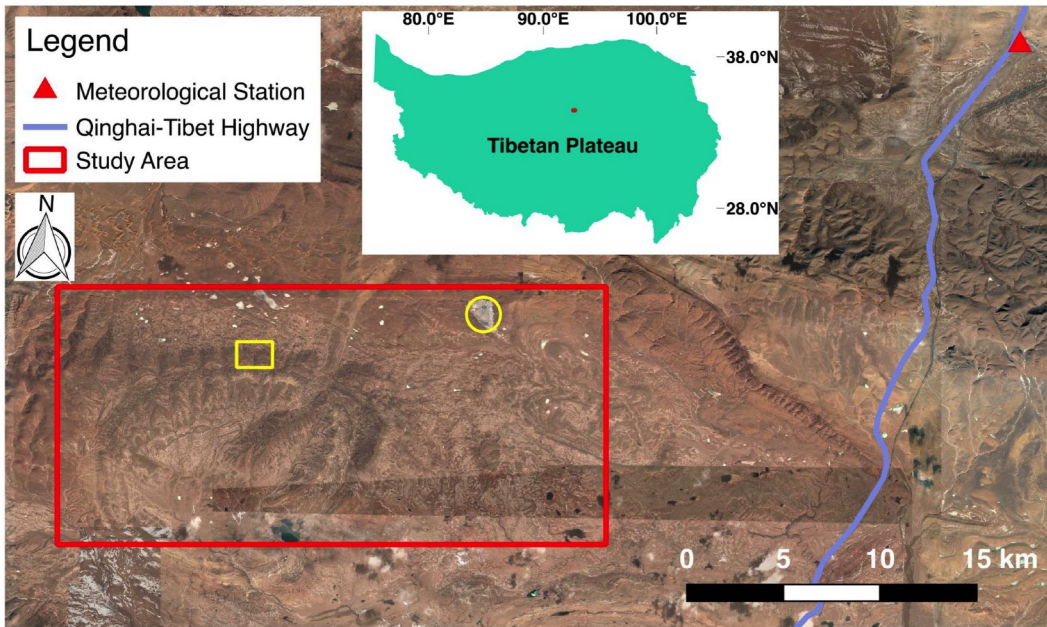


Figure 5.1: The red rectangle and triangle indicate the extent of our study area and the location of the nearest meteorological station (93.083°E , 35.217°N), respectively. The background is the Google image. The yellow rectangle and circle indicate the extent of Figure 5.2 and a lake that will be discussed in section 5.3, respectively.

Beiluhe region, respectively. The two-meter image was used as the reference image for co-registration. Figure 5.2 shows the example images of a small extent (the yellow rectangle in Figure 5.1 within which many RTSs developed). The spatial resolution of the SPOT images is 2.5 meters. The product level of the SPOT images is 1A, with a geolocation accuracy of 30 m.

The pre-processing steps for the images include reprojection, orthorectification, cropping, and co-registration. We reprojected and orthorectified the SPOT-5 images using NASA Ames Stereo Pipeline (github.com/NeoGeographyToolkit/StereoPipeline) and the SRTM DEM (Farr et al., 2007). All the images from Google Earth and SPOT-5 were reprojected to UTM 46N. To reduce the uncertainties due to image location accuracies, we applied co-registration to all the images. We chose the Google image acquired in 2010 as the reference image, then utilized scale invariant feature transform (SIFT) algorithm (Lowe, 2004) and the GPU implementation (github.com/pitzer/SiftGPU)

Table 5.1: List of high-resolution images in the order of acquisition dates

Source	Acquisition date	Resolution (m)	Remark
GeoEye-1	2010-03-27	1	
	2010-05-06		
	2010-10-14		snow cover
	2010-11-04		sparse snow cover
	2011-08-11		
	2011-12-14		
IKONOS-2	2012-11-16/2012-12-27	1	

to find tie-points between the reference image and other images. After extracting tie-points, we warped images by using GDAL with a first-order polynomial model.

5.2.3 Identifying the development of RTSs

We manually identified the RTS development using multi-temporal images (Table 5.1) in QGIS. Firstly, we delineated RTSs on the 2012 Google images using the method which is the same as the one for delineating ground truths in section 4.3.2. Secondly, we inspected the locations of delineated RTSs on multi-temporal images before 2012. We identified the presence of ALDs or RTSs on SPOT-5 images but did not delineate their boundaries because (1) two of SPOT-5 images present snow cover and (2) three SPOT-5 images without snow cover do not show significant changes in landforms when compared with the Google images. As shown in Figure 5.2, headwall shadow is the key feature to distinguish between an ALD and an RTS. Lastly, we categorized the location states in each year (i.e., 2010, 2011, and 2012) into six classes: ALD, ALD to RTS, undisturbed Slope, Slope to RTS, RTS, and Unknown. The criterion for the categorization is based on what presented on the multi-temporal images in each year. For example, if a location always presents ALD on the four 2010 images, we categorized its state as “ALD”. If the location presents ALD on the March or May images, but RTS in October or November, then we considered its state as “ALD to RTS”. If some

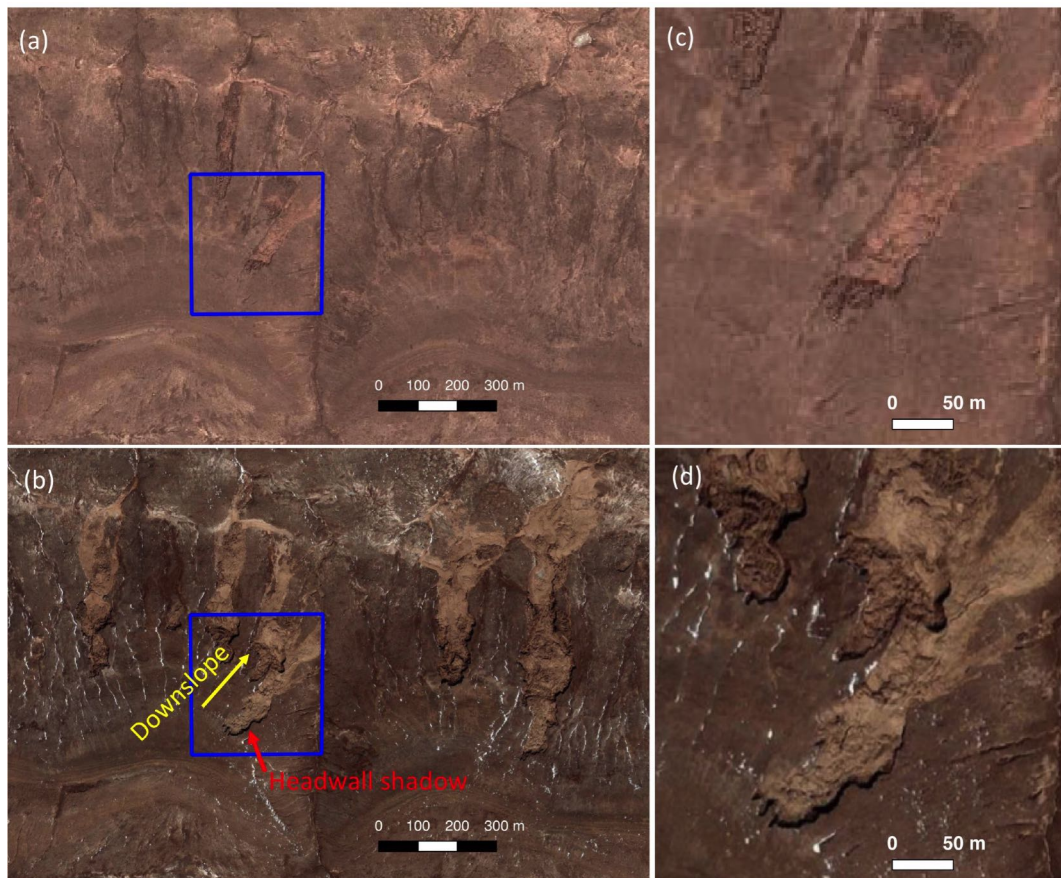


Figure 5.2: The comparison between Google images acquired on 2010-03-27 and 2012-11-16 shows that abrupt changes of non-lake thermokarst landforms. The red arrow indicates the headwall shadow. (c) and (d) zoom into the blue boxes in (a) and (b), respectively.

locations do not have sufficient information for categorization due to snow cover or cloud cover, then their states would be marked as “Unknown”. Furthermore, if the state of an RTS location is “ALD to RTS” or “Slope to RTS” in a specific year, we considered the RTS was initiated in that year.

5.2.4 MODIS snow cover products and meteorological data

We utilized MODIS daily snow cover products MOD10A1 and MYD10A1 at 500 m spatial resolution to calculate snow cover days (Hall and Riggs, 2016). We downloaded and pre-processed MODIS data using Google Earth Engine (Gorelick et al., 2017). We calculated snow cover days pixel by pixel and obtained images of snow cover days for each season spanning years from 2003 to 2012.

We analyzed the changes of air temperature and precipitation from 2002 to 2012 based on observations from the nearest meteorological station as shown in Figure 5.1. We also used least-squares regression to estimate the trend and seasonal cycles of the air temperature.

5.3 Preliminary results

In total, 78 RTSs were identified on the 2012 Google image (Figure 5.3). The inspection of 78 RTS locations on multi-temporal images shows that “ALD to RTS” or ”Slope to RTS” occurred at 63 of them, indicating that 63 of RTSs were initiated in 2010. Furthermore, 14 of RTSs were initiated in 2011, and one in 2012 as shown in Table 5.2. Table 5.3 shows that: (1) in 2010, 9 of the RTS locations presented ALDs, 6 were undisturbed slopes, 36 transformed from ALDs to RTSs, 27 newly developed RTSs; (2) in 2011, seven transformed from ALDs to RTSs, six transformed from slope to RTS, one was a undisturbed slope, one was undetermined due to the time gap of the available images.

Figures 5.4 and 5.5 show the daily mean air temperature, annual, and monthly pre-

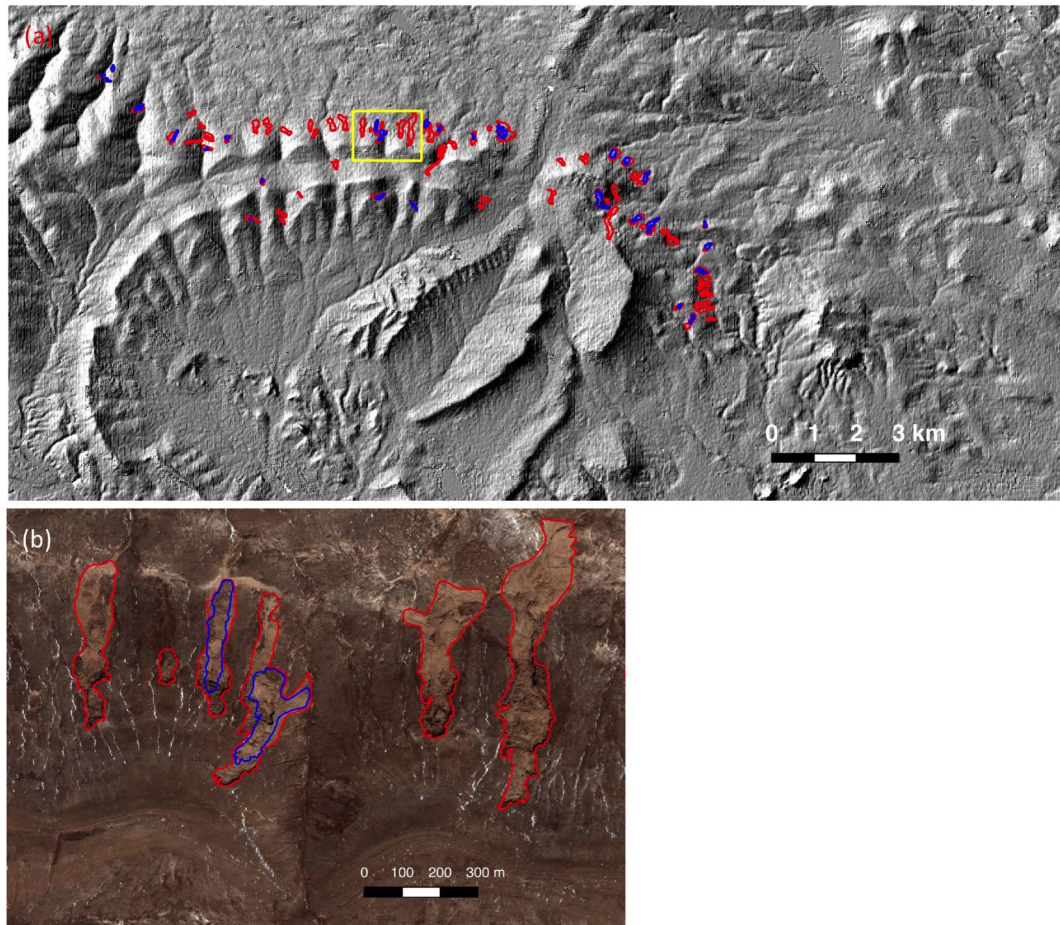


Figure 5.3: ALDs and RTSs in the study area. The red and blue polygons are RTS boundaries delineated using the 2012 Google image and ALD boundaries derived from the 2010 Google image, respectively. (a) and (b) show these boundaries on a hillshade image and on the 2012 Google image, respectively. The extent of (b) is marked by the yellow rectangle in (a).

Table 5.2: The number of RTS initiation in different years

	2010	2011	2012
Count	63	14	1

Table 5.3: The number of RTS development in different years.

Development	2010	2011	2012
	(images: 2010-03, 2010-05, 2010-11)	(images: 2011-08, 2011-12)	(images: 2012-11)
ALD	9	0	0
ALD to RTS	36	7	0
Undisturbed Slope	6	1	0
Slope to RTS	27	6	1
RTS	0	63	77
Unknown	0	1	0
Total	78	78	78

cipitation recorded from the nearest meteorological station. The mean air temperature increase by 0.8 °C from 2002 to 2012. Annual and monthly precipitations show that the precipitation during 2003–2007 was lower than the other years, and most of the precipitation occurred from May to September in each year.

From 2003 to 2012, snow cover occurred throughout the year but always peaked in October, November, and December as shown in Figure 5.6. From 2007 to 2010, snow cover lasted for more than 30 days in winter (October, November, and December). Particularly, it lasted for nearly two months in 2008.

Based on these results, we speculate that the longer-than-normal snow cover from 2007 to 2010, especially 2008, may possibly trigger the formation of many RTSs in 2010. Because of snow’s low thermal conductivity, it prevents ground from cooling in autumn or winter (Zhang, 2005). For example, the ground temperature can increase and decrease significantly (a few Celsius degrees) due to the change of snow cover timing by 10 days (Ling and Zhang, 2003). Most of the precipitation was in the summers, but there was no significant increase as shown in Figure 5.5. The air temperature records

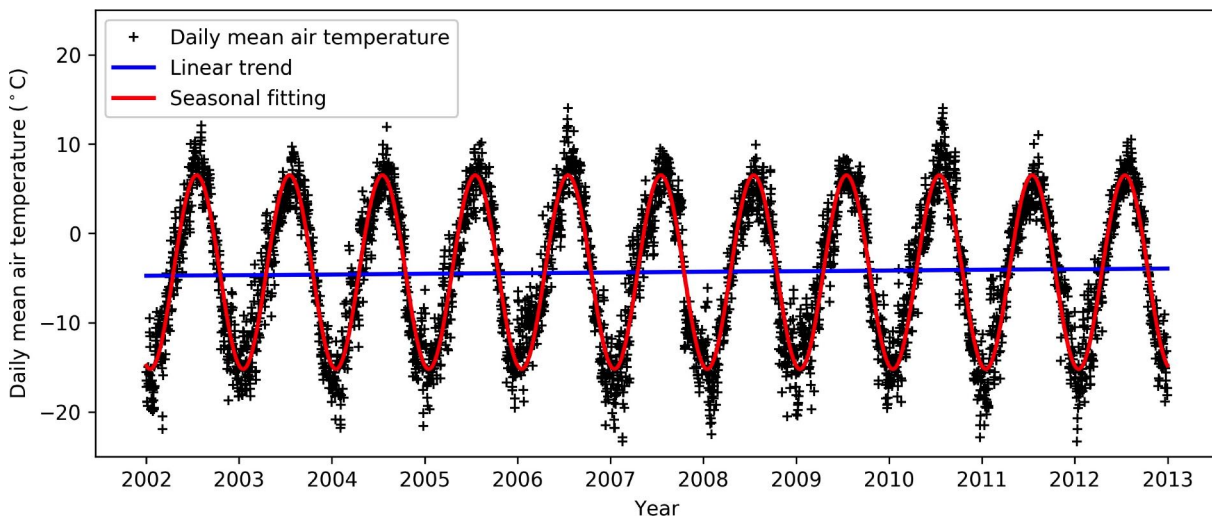


Figure 5.4: Mean daily air temperature at the meteorological station (as shown in Figure 5.1) from 2002 to 2012.

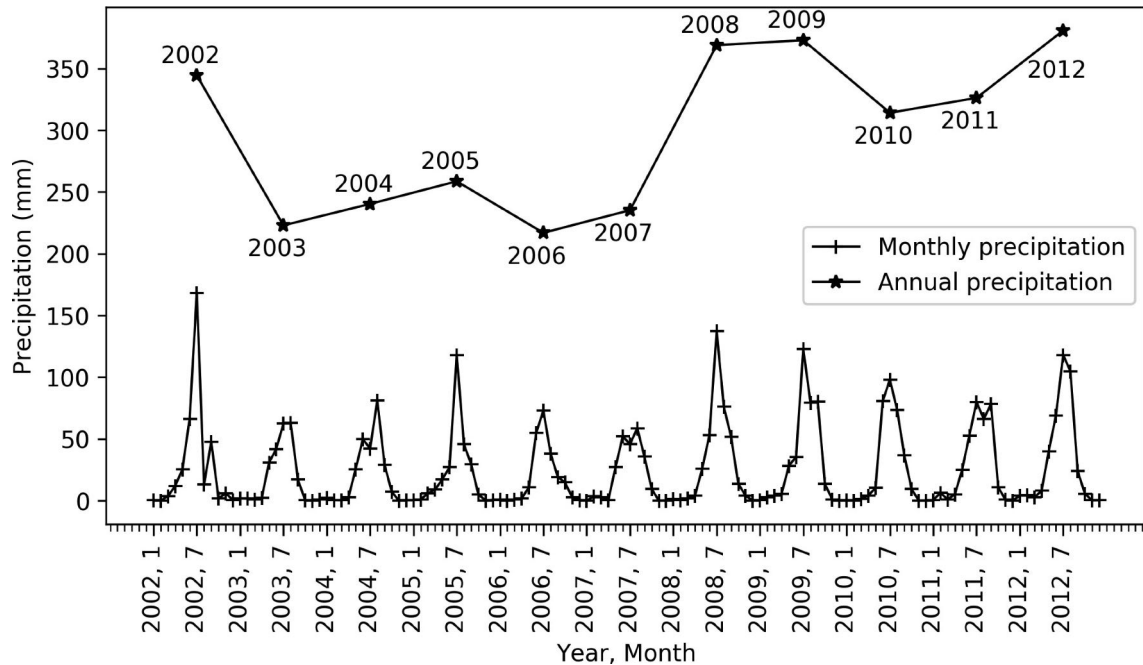


Figure 5.5: Annual and monthly precipitation at the meteorological station (as shown in Figure 5.1) from 2002 to 2012.

showed an increase from 2003 to 2012, which could be another external factor, but the link between RTS formation and the air temperature is not self-evident. For instance, in summer 2010, the air temperature exceeded 10 °C on many days, but a similar case occurred in 2006 as well.

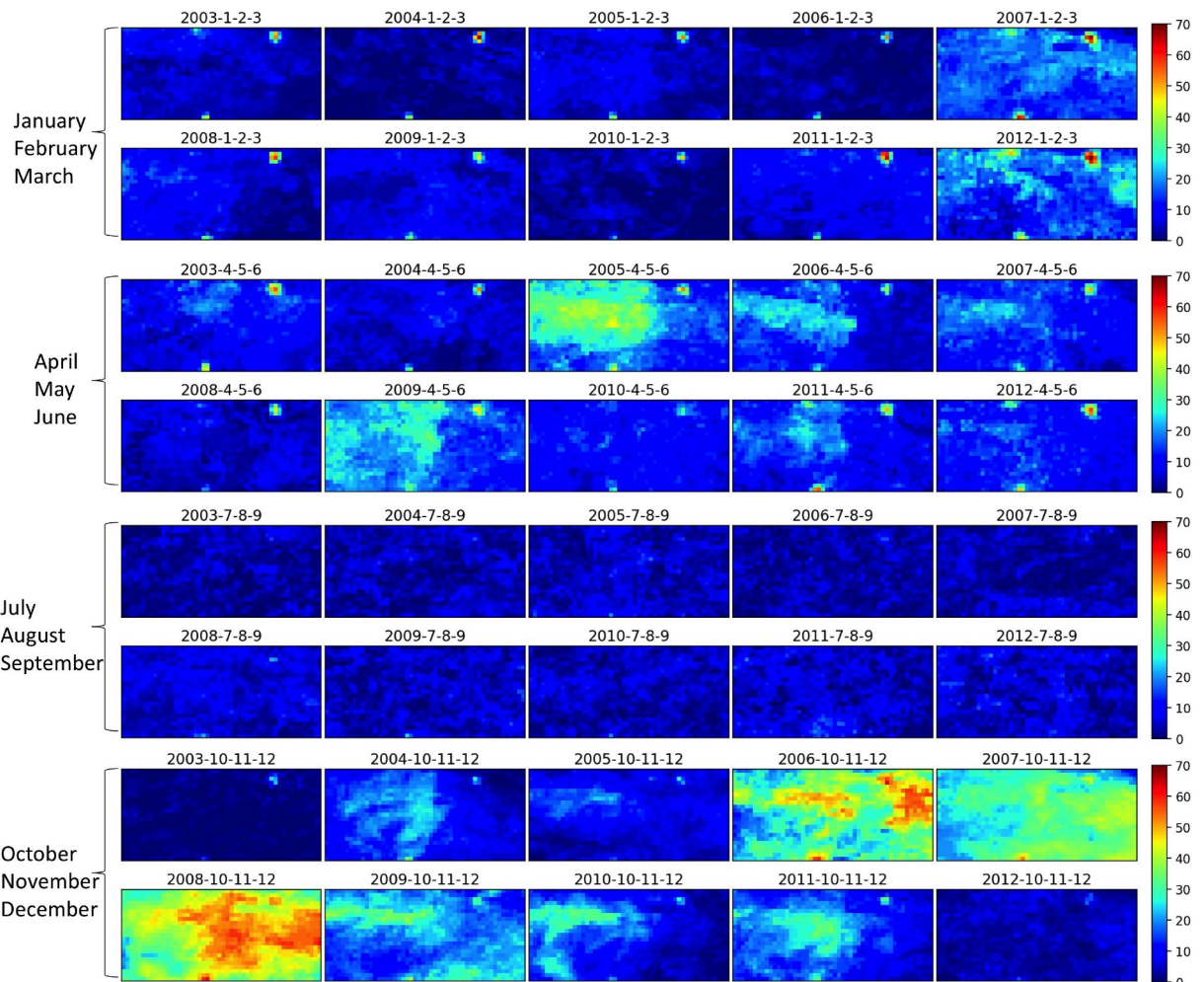


Figure 5.6: Seasonal snow cover days from 2002 to 2012. The hot spot in the northeastern of the study area is due to the misclassification of a lake (marked by the yellow circle in Figure 5.1) in MODIS snow products.

5.4 Summary and future work

This chapter describes the development of RTSs on multi-temporal high-resolution images covering the Beiluhe region. Around 80% of the RTSs were triggered in 2010 and 18% in 2011. Our simple analyses of meteorological data and snow cover products suggest the abnormal snow cover from 2007 to 2010, especially 2008 as the possible external factor.

This is a preliminary study, and many questions need to be addressed in the future: (1) what is the retreat rates of RTSs from 2010 to 2012 and after 2012? (2) what is the role of air temperature in the formation of RTSs? and (3) since most precipitation occurred in the summer (recorded by the meteorological station), what factors derived the abnormal snow cover from 2007 to 2010?

In the future, we will conduct a more quantitative investigation and further analysis. We will collect more high-resolution after 2012 and quantitatively investigate the development of RTSs. Then we will calculate the retreat rates of these thaw slumps. We will analyze the daily air temperature in more detailed and try to identify the possible link between air temperature and RTS development. Reanalysis data provide informative information on weather and climate changing over time. We can also integrate these data in our further work. Then we can conduct an in-depth analysis of external factors that activated the RTSs.

Chapter 6

Conclusions

6.1 Summary and conclusions

This dissertation presents the works of mapping non-lake thermokarst landforms (including thermo-erosion gullies, active layer detachments, and retrogressive thaw slumps) on Tibetan Plateau using high-resolution remote sensing images. These works include: (1) the application of GEOBIA to map thermo-erosion gullies on Eboling Mountain, (2) proposing a strategy which can utilize a cutting-edge deep learning algorithm (i.e., DeepLab) to map thermo-erosion gullies on UAV-based remote sensing images, (3) applying the same strategy with a newer version of DeepLab to Planet CubeSat images, then mapping retrogressive thaw slumps in the Beiluhe region, (4) conducting a large number of experiments to prove the robustness of the deep-learning-based mapping method, (5) quantifying the geometric characteristics and terrain variables of these landforms, and (6) identifying active layer detachments and retrogressive thaw slumps on multi-temporal remote sensing images and analyzing the triggering factors by integrating meteorological data and MODIS snow cover products.

The major conclusions of this dissertation are listed as follows.

- (1) The deep-learning-based mapping method outperforms GEOBIA-based one, and most of the results well match manual delineation.

- (2) The effectiveness, robustness, and transferability of the deep-learning-based mapping method are proved by well-designed experiments in two areas on the Tibetan Plateau, indicating that it can be potentially applied to larger areas.
- (3) Thermo-erosion gullies on Eboling Mountain are small and narrow, with areas < 0.21 ha, perimeters < 1000 m, and circularity indexes < 0.25 , and they preferentially develop on slopes gentler than 17° but steeper than 8° .
- (4) The spatial distribution of the thermo-erosion gullies is co-located with the simulated surface streams.
- (5) Retrogressive thaw slumps in the Beiluhe region are also small, with areas $<$ eight ha, perimeters < 2000 m, and they preferentially develop at locations with north-facing as well as gentle slopes ($4\text{--}8^\circ$) and areas lower than the surroundings.
- (6) The abrupt development of retrogressive thaw slumps between 2010 and 2012 may be attributed to the abnormal snow cover in the cooling season from 2007 to 2010.

6.2 Future directions

The future directions include two aspects: (1) extending the deep-learning-based mapping method to larger areas and (2) integrating more data to understand the development of non-lake thermokarst landforms.

To extend the study area to a large area such as the whole Tibetan Plateau, some challenges need to be overcome. Firstly, high-resolution remote sensing images over a large area are difficult to collect because they are usually available from commercial satellites, and also pose a challenge due to big data volume. A solution to this challenge is combining low-resolution (15–30 m) satellite images such as Landsat or Sentinel-2 images with high-resolution ones. The locations of non-lake thermokarst landforms can be detected from low-resolution images. Knowing their locations, the volume of high-resolution images can be reduced significantly, because these landforms scatter in permafrost areas. Secondly, the deep learning algorithm used in this dissertation

only accepts three bands as input data. We need to improve the current algorithm or adopt some new algorithms for fully utilizing image multi-band images. Multiple sources of satellite images would lead to image heterogeneity, which requires the high capability of deep learning algorithms and extensive training data. The high capability of DeepLab has been verified in many complex scenarios. However, preparing training data for larger areas may need extensive efforts.

The development and spatial distribution of non-lake thermokarst landforms are important for understanding permafrost degradation and the associated impacts. In the future, multi-temporal remote sensing images can be used to investigate the temporal changes of these landforms. To understand the controlling factors, many other data such as topography, vegetation, soil texture, and meteorological data are necessary for the analysis. For example, multivariate correlation analysis between the development of landforms (such as the retreat rate of RTSs) and air temperature may be able to identify connections between them.

Bibliography

- Åkerman, H.J., Johansson, M., 2008. Thawing Permafrost and Thicker Active Layers in Sub-Arctic Sweden. *Permafrost and Periglacial Processes* 19, 279–292.
- Altena, B., Kääb, A., 2017. Glacier Ice Loss Monitored Through the Planet Cubesat Constellation, in: 2017 9th International Workshop on the Analysis of Multitemporal Remote Sensing Images (MultiTemp), IEEE. pp. 1–4.
- Andresen, C.G., Lougheed, V.L., 2015. Disappearing Arctic Tundra Ponds: Fine-scale Analysis of Surface Hydrology in Drained Thaw Lake Basins over a 65 Year Period (1948–2013). *Journal of Geophysical Research: Biogeosciences* 120, 466–479.
- Aragon, B., Houborg, R., Tu, K., Fisher, J.B., McCabe, M., 2018. CubeSats Enable High Spatiotemporal Retrievals of Crop-Water Use for Precision Agriculture. *Remote Sensing* 10, 1867.
- Armstrong, L., Lacelle, D., Fraser, R.H., Kokelj, S., Knudby, A., 2018. Thaw Slump Activity Measured using Stationary Cameras in Time-Lapse and Structure-from-Motion Photogrammetry. *Arctic Science* 4, 827–845.
- Balser, A.W., Jones, J.B., Gens, R., 2014. Timing of Retrogressive Thaw Slump Initiation in the Noatak Basin, Northwest Alaska, USA. *Journal of Geophysical Research: Earth Surface* 119, 1106–1120.
- Belshe, E.F., Schuur, E.A.G., Grosse, G., 2013. Quantification of Upland Thermokarst

- Features With High Resolution Remote Sensing. *Environmental Research Letters* 8, 035016.
- Biskaborn, B.K., Smith, S.L., Noetzli, J., Matthes, H., Vieira, G., Streletskeiy, D.A., Schoeneich, P., Romanovsky, V.E., Lewkowicz, A.G., Abramov, A., et al., 2019. Permafrost Is Warming at a Global Scale. *Nature Communications* 10, 264.
- Blaschke, T., 2010. Object Based Image Analysis for Remote Sensing. *ISPRS Journal of Photogrammetry and Remote Sensing* 65, 2–16.
- Böhner, J., Antonić, O., 2009. Land-Surface Parameters Specific to Topo-Climatology. *Developments in Soil Science* 33, 195–226.
- Bowden, W.B., 2010. Climate Change in the Arctic–Permafrost, Thermokarst, and Why They Matter to the Non-arctic World. *Geography Compass* 4, 1553–1566.
- Brooker, A., 2014. Investigating Changes in Retrogressive Thaw Slumps in the Richardson Mountains (Northwest Territories, Canada) Based on Tasseled Cap Trend Analysis of Landsat Image Stacks.
- Brooker, A., Fraser, R.H., Olthof, I., Kokelj, S.V., Lacelle, D., 2014. Mapping the Activity and Evolution of Retrogressive Thaw Slumps by Tasselled Cap Trend Analysis of a Landsat Satellite Image Stack. *Permafrost and Periglacial Processes* 25, 243–256.
- Brown, J., Ferrians Jr, O., Heginbottom, J., Melnikov, E., 1997. Circum-Arctic Map of Permafrost and Ground-Ice Conditions. US Geological Survey Reston, VA.
- Burn, C., Friele, P., 1989. Geomorphology, Vegetation Succession, Soil Characteristics and Permafrost in Retrogressive Thaw Slumps Near Mayo, Yukon Territory. *Arctic*, 31–40.
- Burn, C., Lewkowicz, A., 1990. Canadian Landform Examples-17 Retrogressive Thaw Slumps. *Canadian Geographer/Le Géographe canadien* 34, 273–276.

- Cao, B., Gruber, S., Zhang, T., Li, L., Peng, X., Wang, K., Zheng, L., Shao, W., Guo, H., 2017. Spatial Variability of Active Layer Thickness Detected by Ground-Penetrating Radar in the Qilian Mountains, Western China. *Journal of Geophysical Research: Earth Surface* 122, 574–591.
- Cassidy, A.E., Christen, A., Henry, G.H., 2017. Impacts of Active Retrogressive Thaw Slumps on Vegetation, Soil, and Net Ecosystem Exchange of Carbon Dioxide in the Canadian High Arctic. *Arctic Science* 3, 179–202.
- Castelvecchi, D., 2016. Can We Open the Black Box of AI? *Nature News* 538, 20.
- Chen, G., Hay, G.J., Carvalho, L.M., Wulder, M.A., 2012. Object-Based Change Detection. *International Journal of Remote Sensing* 33, 4434–4457.
- Chen, L.C., Papandreou, G., Kokkinos, I., Murphy, K., Yuille, A.L., 2016. Deeplab: Semantic Image Segmentation With Deep Convolutional Nets, Atrous Convolution, and Fully Connected Crfs. *arXiv preprint arXiv:1606.00915* .
- Chen, L.C., Zhu, Y., Papandreou, G., Schroff, F., Adam, H., 2018. Encoder-Decoder With Atrous Separable Convolution for Semantic Image Segmentation. *arXiv preprint arXiv:1802.02611* .
- Chollet, F., 2017. Xception: Deep Learning With Depthwise Separable Convolutions, in: 2017 IEEE Conference on Computer Vision and Pattern Recognition (CVPR), Honolulu, Hawaii, United States. pp. 1800–1807.
- Comaniciu, D., Meer, P., 2002. Mean Shift: A Robust Approach Toward Feature Space Analysis. *IEEE Transactions on Pattern Analysis & Machine Intelligence* , 603–619.
- Conrad, O., Bechtel, B., Bock, M., Dietrich, H., Fischer, E., Gerlitz, L., Wehberg, J., Wichmann, V., Böhner, J., 2015. System for Automated Geoscientific Analyses (SAGA) V. 2.1. 4. *Geoscientific Model Development* 8, 1991–2007.

- Cooley, S., Smith, L., Stepan, L., Mascaro, J., 2017. Tracking Dynamic Northern Surface Water Changes With High-Frequency Planet CubeSat Imagery. *Remote Sensing* 9, 1306.
- Cooley, S.W., Smith, L.C., Ryan, J.C., Pitcher, L.H., Pavelsky, T.M., 2019. Arctic-Boreal Lake Dynamics Revealed Using CubeSat Imagery. *Geophysical Research Letters*.
- Cortes, C., Vapnik, V., 1995. Support-Vector Networks. *Machine learning* 20, 273–297.
- Council, N.R., 2014. Opportunities to Use Remote Sensing in Understanding Permafrost and Related Ecological Characteristics: Report of a Workshop. National Academies Press: Washington, DC, USA.
- Czudek, T., Demek, J., 1970. Thermokarst in Siberia and Its Influence on the Development of Lowland Relief. *Quaternary Research* 1, 103–120.
- Everingham, M., Eslami, S.A., Gool, L.V., Williams, C.K., Winn, J., Zisserman, A., 2015. The Pascal Visual Object Classes Challenge: A Retrospective. *International Journal of Computer Vision* 111, 98–136.
- Farr, T.G., Rosen, P.A., Caro, E., Crippen, R., Duren, R., Hensley, S., Kobrick, M., Paller, M., Rodriguez, E., Roth, L., et al., 2007. The Shuttle Radar Topography Mission. *Reviews of Geophysics* 45, 1–33.
- Fortier, D., Allard, M., Shur, Y., 2007. Observation of Rapid Drainage System Development by Thermal Erosion of Ice Wedges on Bylot Island, Canadian Arctic Archipelago. *Permafrost and Periglacial Processes* 18, 229–243.
- French, H.M., 2017. The Periglacial Environment. John Wiley & Sons.
- Godin, E., Fortier, D., 2010. Geomorphology of Thermo-Erosion Gullies—Case Study From Bylot Island, Nunavut, Canada, in: Proceedings of the 6th Canadian Per-

- mafrost Conference and 63rd Canadian Geotechnical Conference, Calgary, pp. 1540–1547.
- Godin, E., Fortier, D., 2012. Fine Scale Spatio-Temporal Monitoring of Multiple Thermo-Erosion Gullies Development on Bylot Island, Eastern Canadian Archipelago, in: Proceedings, Tenth International Conference on Permafrost (TICOP), Salekhard, Russia, pp. 1–7.
- Godin, E., Fortier, D., Coulombe, S., 2014. Effects of Thermo-Erosion Gullying on Hydrologic Flow Networks, Discharge and Soil Loss. *Environmental Research Letters* 9, 105010.
- Goodfellow, I., Bengio, Y., Courville, A., Bengio, Y., 2016. Deep Learning. volume 1. MIT press Cambridge.
- Gooseff, M.N., Balser, A., Bowden, W.B., Jones, J.B., 2009. Effects of Hillslope Thermokarst in Northern Alaska. *Eos, Transactions American Geophysical Union* 90, 29–30.
- Gorelick, N., Hancher, M., Dixon, M., Ilyushchenko, S., Thau, D., Moore, R., 2017. Google Earth Engine: Planetary-Scale Geospatial Analysis for Everyone. *Remote Sensing of Environment* 202, 18–27.
- Grosse, G., Harden, J., Turetsky, M., McGuire, A.D., Camill, P., Tarnocai, C., Frolking, S., Schuur, E.A., Jorgenson, T., Marchenko, S., 2011. Vulnerability of High-Latitude Soil Organic Carbon in North America to Disturbance. *Journal of Geophysical Research: Biogeosciences* 116.
- Guisan, A., Weiss, S.B., Weiss, A.D., 1999. GLM Versus CCA Spatial Modeling of Plant Species Distribution. *Plant Ecology* 143, 107–122.
- Guo, W., Yang, W., Zhang, H., Hua, G., 2018. Geospatial Object Detection in High

- Resolution Satellite Images Based on Multi-Scale Convolutional Neural Network. *Remote Sensing* 10, 131.
- Hall, D.K., Riggs, G.A., 2016. MODIS/Terra Snow Cover Daily L3 Global 500m SIN Grid, Version 6. Boulder, Colorado USA. NASA National Snow and Ice Data Center Distributed Active Archive Center. doi:<https://doi.org/10.5067/MODIS/MOD10A1.006>. [DateAccessed] .
- Harms, T.K., Abbott, B.W., Jones, J.B., 2014. Thermo-Erosion Gullies Increase Nitrogen Available for Hydrologic Export. *Biogeochemistry* 117, 299–311.
- Hay, G.J., Castilla, G., 2008. Geographic Object-Based Image Analysis (GEOBIA): A New Name for a New Discipline, in: Object-Based Image Analysis. Springer, pp. 75–89.
- Hjort, J., Karjalainen, O., Aalto, J., Westermann, S., Romanovsky, V.E., Nelson, F.E., Etzelmüller, B., Luoto, M., 2018. Degrading Permafrost Puts Arctic Infrastructure at Risk by Mid-Century. *Nature Communications* 9, 5147.
- Houborg, R., McCabe, M., 2016. High-Resolution NDVI From Planet's Constellation of Earth Observing Nano-Satellites: A New Data Source for Precision Agriculture. *Remote Sensing* 8, 768.
- Houborg, R., McCabe, M., 2018. Daily Retrieval of NDVI and LAI at 3 M Resolution via the Fusion of CubeSat, Landsat, and MODIS Data. *Remote Sensing* 10, 890.
- Hu, Z., Li, Q., Zou, Q., Zhang, Q., Wu, G., 2016. A Bilevel Scale-Sets Model for Hierarchical Representation of Large Remote Sensing Images. *IEEE Transactions on Geoscience and Remote Sensing* 54, 7366–7377.
- Huang, B., Zhao, B., Song, Y., 2018a. Urban Land-Use Mapping Using a Deep Convolutional Neural Network With High Spatial Resolution Multispectral Remote Sensing Imagery. *Remote Sensing of Environment* 214, 73–86.

- Huang, L., Liu, L., Jiang, L., Zhang, T., 2018b. Automatic Mapping of Thermokarst Landforms From Remote Sensing Images Using Deep Learning: A Case Study in the Northeastern Tibetan Plateau. *Remote Sensing* 10, 2067.
- Huang, L., Zhang, G., Zhou, C., Wang, Y., 2014. The Parallel Segmentation Algorithm Based on Pyramid Image for High Spatial Resolution Remote Sensing Image, in: *Remote Sensing of the Environment: 18th National Symposium on Remote Sensing of China, International Society for Optics and Photonics*. p. 915803.
- Huang, X., Zhang, L., Li, P., 2007. Classification and Extraction of Spatial Features in Urban Areas Using High-Resolution Multispectral Imagery. *IEEE Geoscience and Remote Sensing Letters* 4, 260–264.
- Inglada, J., Christophe, E., 2009. The Orfeo Toolbox Remote Sensing Image Processing Software, in: *2009 IEEE International Geoscience and Remote Sensing Symposium*, IEEE. pp. IV–733.
- Jean, N., Burke, M., Xie, M., Davis, W.M., Lobell, D.B., Ermon, S., 2016. Combining Satellite Imagery and Machine Learning to Predict Poverty. *Science* 353, 790–794.
- Jin, H., Li, S., Cheng, G., Shaoling, W., Li, X., 2000. Permafrost and Climatic Change in China. *Global and Planetary Change* 26, 387–404.
- Jones, M.K.W., Pollard, W.H., Jones, B.M., 2019. Rapid Initialization of Retrogressive Thaw Slumps in the Canadian High Arctic and Their Response to Climate and Terrain Factors. *Environmental Research Letters* 14, 055006.
- Jorgenson, M.T., 2013. Thermokarst Terrains. *Treatise on Geomorphology* 8, 313–324.
- Jorgenson, M.T., Osterkamp, T.E., 2005. Response of Boreal Ecosystems to Varying Modes of Permafrost Degradation. *Canadian Journal of Forest Research* 35, 2100–2111.

- Jorgenson, M.T., Shur, Y.L., Pullman, E.R., 2006. Abrupt Increase in Permafrost Degradation in Arctic Alaska. *Geophysical Research Letters* 33.
- Kokelj, S.V., Jorgenson, M., 2013. Advances in Thermokarst Research. *Permafrost and Periglacial Processes* 24, 108–119.
- Krieger, K.E., 2012. The Topographic Form and Evolution of Thermal Erosion Features: A First Analysis Using Airborne and Ground-Based LiDAR in Arctic Alaska. Ph.D. thesis. Idaho State University Pocatello, ID, USA.
- Krizhevsky, A., Sutskever, I., Hinton, G.E., 2012. Imagenet Classification With Deep Convolutional Neural Networks, in: Advances in neural information processing systems, Lake Tahoe, NY, USA, pp. 1097–1105.
- Lacelle, D., Bjornson, J., Lauriol, B., 2010. Climatic and Geomorphic Factors Affecting Contemporary (1950–2004) Activity of Retrogressive Thaw Slumps on the Aklavik Plateau, Richardson Mountains, NWT, Canada. *Permafrost and Periglacial Processes* 21, 1–15.
- Lacelle, D., Brooker, A., Fraser, R.H., Kokelj, S.V., 2015. Distribution and Growth of Thaw Slumps in the Richardson Mountains–Peel Plateau Region, Northwestern Canada. *Geomorphology* 235, 40–51.
- Lantuit, H., Pollard, W.H., 2008. Fifty Years of Coastal Erosion and Retrogressive Thaw Slump Activity on Herschel Island, Southern Beaufort Sea, Yukon Territory, Canada. *Geomorphology* 95, 84–102.
- Lantz, T.C., Kokelj, S.V., 2008. Increasing Rates of Retrogressive Thaw Slump Activity in the Mackenzie Delta Region, NWT, Canada. *Geophysical Research Letters* 35.
- LeCun, Y., Bengio, Y., Hinton, G., 2015. Deep Learning. *Nature* 521, 436–444.
- LeCun, Y., Bottou, L., Bengio, Y., Haffner, P., 1998. Gradient-Based Learning Applied to Document Recognition. *Proceedings of the IEEE* 86, 2278–2324.

- Leibman, M., Kizakov, A., Sulerzhitsky, L., Zaretskaia, N., 2003. Dynamics of Landslide Slopes and Their Development on Yamal Peninsula, in: Permafrost. Proceedings of the 8th international conference on permafrost. Swets and Zeitlinger, Lisse, pp. 651–656.
- Leibman, M.O., 1995. Cryogenic Landslides on the Yamal Peninsula, Russia: Preliminary Observations. *Permafrost and Periglacial Processes* 6, 259–264.
- Lewkowicz, A.G., 2007. Dynamics of Active-Layer Detachment Failures, Fosheim Peninsula, Ellesmere Island, Nunavut, Canada. *Permafrost and Periglacial Processes* 18, 89–103.
- Lewkowicz, A.G., Harris, C., 2005. Morphology and Geotechnique of Active-Layer Detachment Failures in Discontinuous and Continuous Permafrost, Northern Canada. *Geomorphology* 69, 275–297.
- Lewkowicz, A.G., Way, R.G., 2019. Extremes of Summer Climate Trigger Thousands of Thermokarst Landslides in a High Arctic Environment. *Nature Communications* 10, 1329.
- Lin, Z., Niu, F., Liu, H., Lu, J., 2011. Disturbance-Related Thawing of a Ditch and Its Influence on Roadbeds on Permafrost. *Cold Regions Science and Technology* 66, 105–114.
- Lin, Z., Niu, F., Xu, Z., Xu, J., Wang, P., 2010. Thermal Regime of a Thermokarst Lake and Its Influence on Permafrost, Beiluhe Basin, Qinghai-Tibet Plateau. *Permafrost and Periglacial Processes* 21, 315–324.
- Ling, F., Zhang, T., 2003. Impact of the Timing and Duration of Seasonal Snow Cover on the Active Layer and Permafrost in the Alaskan Arctic. *Permafrost and Periglacial Processes* 14, 141–150.

- Liu, F., Chen, L., Zhang, B., Wang, G., Qin, S., Yang, Y., 2018. Ultraviolet Radiation Rather Than Inorganic Nitrogen Increases Dissolved Organic Carbon Biodegradability in a Typical Thermo-Erosion Gully on the Tibetan Plateau. *Science of the Total Environment* 627, 1276–1284.
- Lowe, D.G., 2004. Distinctive Image Features From Scale-Invariant Keypoints. *International Journal of Computer Vision* 60, 91–110.
- Luo, J., Niu, F., Lin, Z., Liu, M., Yin, G., 2015. Thermokarst Lake Changes Between 1969 and 2010 in the Beilu River Basin, Qinghai-Tibet Plateau, China. *Science Bulletin* 60, 556–564.
- Matikainen, L., Karila, K., Hyppä, J., Litkey, P., Puttonen, E., Ahokas, E., 2017. Object-Based Analysis of Multispectral Airborne Laser Scanner Data for Land Cover Classification and Map Updating. *ISPRS Journal of Photogrammetry and Remote Sensing* 128, 298–313.
- McFeeters, S.K., 1996. The Use of the Normalized Difference Water Index (NDWI) in the Delineation of Open Water Features. *International Journal of Remote Sensing* 17, 1425–1432.
- McRoberts, E., Morgenstern, N.R., 1974a. Stability of Slopes in Frozen Soil, Mackenzie Valley, NWT. *Canadian Geotechnical Journal* 11, 554–573.
- McRoberts, E., Morgenstern, N.R., 1974b. The Stability of Thawing Slopes. *Canadian Geotechnical Journal* 11, 447–469.
- Miles, E., Watson, C., Brun, F., Berthier, E., Esteves, M., Quincey, D., Miles, K., Hubbard, B., Wagnon, P., 2018. Glacial and Geomorphic Effects of a Supraglacial Lake Drainage and Outburst Event, Everest Region, Nepal Himalaya. *The Cryosphere* 12, 3891–3905.

- Mu, C., Zhang, T., Cao, B., Wan, X., Peng, X., Cheng, G., 2013. Study of the Organic Carbon Storage in the Active Layer of the Permafrost Over the Eboling Mountain in the Upper Reaches of the Heihe River in the Eastern Qilian Mountains. *Journal of Glaciology and Geocryology* 35, 1–9.
- Mu, C., Zhang, T., Wu, Q., Cao, B., Zhang, X., Peng, X., Wan, X., Zheng, L., Wang, Q., Cheng, G., 2015. Carbon and Nitrogen Properties of Permafrost Over the Eboling Mountain in the Upper Reach of Heihe River Basin, Northwestern China. *Arctic, Antarctic, and Alpine Research* 47, 203–211.
- Mu, C., Zhang, T., Zhang, X., Cao, B., Peng, X., 2016a. Sensitivity of Soil Organic Matter Decomposition to Temperature at Different Depths in Permafrost Regions on the Northern Qinghai-Tibet Plateau. *European journal of soil science* 67, 773–781.
- Mu, C., Zhang, T., Zhang, X., Li, L., Guo, H., Zhao, Q., Cao, L., Wu, Q., Cheng, G., 2016b. Carbon Loss and Chemical Changes From Permafrost Collapse in the Northern Tibetan Plateau. *Journal of Geophysical Research: Biogeosciences* 121, 1781–1791.
- Nitze, I., Grosse, G., 2016. Detection of Landscape Dynamics in the Arctic Lena Delta With Temporally Dense Landsat Time-Series Stacks. *Remote Sensing of Environment* 181, 27–41.
- Nitze, I., Grosse, G., Jones, B.M., Arp, C.D., Ulrich, M., Fedorov, A., Veremeeva, A., 2017. Landsat-Based Trend Analysis of Lake Dynamics Across Northern Permafrost Regions. *Remote Sensing* 9, 640.
- Nitze, I., Grosse, G., Jones, B.M., Romanovsky, V.E., Boike, J., 2018. Remote Sensing Quantifies Widespread Abundance of Permafrost Region Disturbances Across the Arctic and Subarctic. *Nature Communications* 9, 5423.
- Niu, F., Cheng, G., Ni, W., Jin, D., 2005. Engineering-Related Slope Failure in Per-

- mafrost Regions of the Qinghai-Tibet Plateau. *Cold Regions Science and Technology* 42, 215–225.
- Niu, F., Lin, Z., Lu, J., Luo, J., Wang, H., 2015. Assessment of Terrain Susceptibility to Thermokarst Lake Development Along the Qinghai–Tibet Engineering Corridor, China. *Environmental Earth Sciences* 73, 5631–5642.
- Niu, F., Luo, J., Lin, Z., Fang, J., Liu, M., 2016. Thaw-Induced Slope Failures and Stability Analyses in Permafrost Regions of the Qinghai-Tibet Plateau, China. *Landslides* 13, 55–65.
- Niu, F., Luo, J., Lin, Z., Liu, M., Yin, G., 2014. Thaw-Induced Slope Failures and Susceptibility Mapping in Permafrost Regions of the Qinghai–Tibet Engineering Corridor, China. *Natural hazards* 74, 1667–1682.
- Niu, F., Luo, J., Lin, Z., Ma, W., Lu, J., 2012. Development and Thermal Regime of a Thaw Slump in the Qinghai–Tibet Plateau. *Cold Regions Science and Technology* 83, 131–138.
- Obu, J., Westermann, S., Bartsch, A., Berdnikov, N., Christiansen, H.H., Dashtseren, A., Delaloye, R., Elberling, B., Etzelmüller, B., Kholodov, A., et al., 2019. Northern Hemisphere Permafrost Map Based on TTOP Modelling for 2000–2016 at 1 km² Scale. *Earth-Science Reviews* 193, 299–316.
- Olefeldt, D., Goswami, S., Grosse, G., Hayes, D., Hugelius, G., Kuhry, P., McGuire, A.D., Romanovsky, V.E., Sannel, A.B.K., Schuur, E.A.G., 2016. Circumpolar Distribution and Carbon Storage of Thermokarst Landscapes. *Nature Communications* 7, 1–11.
- d’Oleire Oltmanns, S., Eisank, C., Drägut, L., Blaschke, T., 2013. An Object-Based Workflow to Extract Landforms at Multiple Scales From Two Distinct Data Types. *IEEE Geoscience and Remote Sensing Letters* 10, 947–951.

- Osterkamp, T.E., 2007. Characteristics of the Recent Warming of Permafrost in Alaska. *Journal of Geophysical Research: Earth Surface* 112.
- Patton, A.I., Rathburn, S.L., Capps, D.M., 2019. Landslide Response to Climate Change in Permafrost Regions. *Geomorphology* , 116–128.
- Pedregosa, F., Varoquaux, G., Gramfort, A., Michel, V., Thirion, B., Grisel, O., Blondel, M., Prettenhofer, P., Weiss, R., Dubourg, V., et al., 2011. Scikit-Learn: Machine Learning in Python. *Journal of machine learning research* 12, 2825–2830.
- Peng, X., Zhang, T., Pan, X., Wang, Q., Zhong, X., Wang, K., Mu, C., 2013. Spatial and Temporal Variations of Seasonally Frozen Ground Over the Heihe River Basin of Qilian Mountain in Western China. *Advances in Earth Science* 4, 008.
- Perez, L., Wang, J., 2017. The Effectiveness of Data Augmentation in Image Classification Using Deep Learning. *arXiv preprint arXiv:1712.04621* .
- Pierre, K.A.S., Zolkos, S., Shakil, S., Tank, S.E., St. Louis, V.L., Kokelj, S.V., 2018. Unprecedented Increases in Total and Methyl Mercury Concentrations Downstream of Retrogressive Thaw Slumps in the Western Canadian Arctic. *Environmental Science & Technology* 52, 14099–14109.
- Poesen, J., Nachtergaelie, J., Verstraeten, G., Valentin, C., 2003. Gully Erosion and Environmental Change: Importance and Research Needs. *Catena* 50, 91–133.
- Ramage, J.L., Irrgang, A.M., Herzschuh, U., Morgenstern, A., Couture, N., Lantuit, H., 2017. Terrain Controls on the Occurrence of Coastal Retrogressive Thaw Slumps Along the Yukon Coast, Canada. *Journal of Geophysical Research: Earth Surface* 122, 1619–1634.
- Ran, Y., Li, X., Cheng, G., 2018. Climate Warming Over the Past Half Century Has Led to Thermal Degradation of Permafrost on the Qinghai–Tibet Plateau. *The Cryosphere* 12, 595–608.

- Ran, Y., Li, X., Cheng, G., Zhang, T., Wu, Q., Jin, H., Jin, R., 2012. Distribution of Permafrost in China: An Overview of Existing Permafrost Maps. *Permafrost and Periglacial Processes* 23, 322–333.
- Reu, D.J., Bourgeois, J., Bats, M., Zwertvaegher, A., Gelorini, V., De Smedt, P., Chu, W., Antrop, M., De Maeyer, P., Finke, P., et al., 2013. Application of the Topographic Position Index to Heterogeneous Landscapes. *Geomorphology* 186, 39–49.
- Rouse Jr, J., Haas, R., Schell, J., Deering, D., 1974. Monitoring Vegetation Systems in the Great Plains With ERTS. *Proceedings of the 3rd ERTS Symposium* 1, 309–317.
- Rowland, J., Jones, C., Altmann, G., Bryan, R., Crosby, B., Hinzman, L., Kane, D., Lawrence, D., Mancino, A., Marsh, P., et al., 2010. Arctic Landscapes in Transition: Responses to Thawing Permafrost. *Eos, Transactions American Geophysical Union* 91, 229–230.
- Rudy, A.C., Lamoureux, S.F., Treitz, P., Collingwood, A., 2013. Identifying Permafrost Slope Disturbance Using Multi-Temporal Optical Satellite Images and Change Detection Techniques. *Cold Regions Science and Technology* 88, 37–49.
- Russakovsky, O., Deng, J., Su, H., Krause, J., Satheesh, S., Ma, S., Huang, Z., Karpathy, A., Khosla, A., Bernstein, M., et al., 2015. Imagenet Large Scale Visual Recognition Challenge. *International Journal of Computer Vision* 115, 211–252.
- Schölkopf, B., Smola, A.J., Bach, F., et al., 2002. Learning With Kernels: Support Vector Machines, Regularization, Optimization, and Beyond. MIT press.
- Schuster, P.F., Schaefer, K.M., Aiken, G.R., Antweiler, R.C., Dewild, J.F., Gryziec, J.D., Gusmeroli, A., Hugelius, G., Jafarov, E., Krabbenhoft, D.P., et al., 2018. Permafrost Stores a Globally Significant Amount of Mercury. *Geophysical Research Letters* 45, 1463–1471.

- Schuur, E.A.G., McGuire, A.D., Schdel, C., Grosse, G., Harden, J.W., Hayes, D.J., Hugelius, G., Koven, C.D., Kuhry, P., Lawrence, D.M., 2015. Climate Change and the Permafrost Carbon Feedback. *Nature* 520, 171–179.
- Segal, R.A., Lantz, T.C., Kokelj, S.V., 2016. Acceleration of Thaw Slump Activity in Glaciated Landscapes of the Western Canadian Arctic. *Environmental Research Letters* 11, 034025.
- Serikova, S., Pokrovsky, O., Laudon, H., Krickov, I., Lim, A., Manasypov, R., Karlsson, J., 2019. High Carbon Emissions From Thermokarst Lakes of Western Siberia. *Nature Communications* 10, 1552.
- Shackelford, A.K., Davis, C.H., 2003. A Hierarchical Fuzzy Classification Approach for High-Resolution Multispectral Data Over Urban Areas. *IEEE Transactions on Geoscience and Remote Sensing* 41, 1920–1932.
- Shruthi, R.B., Kerle, N., Jetten, V., 2011. Object-Based Gully Feature Extraction Using High Spatial Resolution Imagery. *Geomorphology* 134, 260–268.
- Silver, D., Schrittwieser, J., Simonyan, K., Antonoglou, I., Huang, A., Guez, A., Hubert, T., Baker, L., Lai, M., Bolton, A., 2017. Mastering the Game of Go Without Human Knowledge. *Nature* 550, 354–359.
- Smith, L.C., Sheng, Y., MacDonald, G., Hinzman, L., 2005. Disappearing Arctic Lakes. *Science* 308, 1429–1429.
- Stieglitz, M., Déry, S., Romanovsky, V., Osterkamp, T., 2003. The Role of Snow Cover in the Warming of Arctic Permafrost. *Geophysical Research Letters* 30.
- Sun, Z., Wang, Y., Sun, Y., Niu, F., Gao, Z., et al., 2017. Creep Characteristics and Process Analyses of a Thaw Slump in the Permafrost Region of the Qinghai-Tibet Plateau, China. *Geomorphology* 293, 1–10.

- Swanson, D., Nolan, M., 2018. Growth of Retrogressive Thaw Slumps in the Noatak Valley, Alaska, 2010–2016, Measured by Airborne Photogrammetry. *Remote Sensing* 10, 983.
- Tchebakova, N., Parfenova, E., Soja, A., 2009. The Effects of Climate, Permafrost and Fire on Vegetation Change in Siberia in a Changing Climate. *Environmental Research Letters* 4, 045013.
- Tong, C., Wu, Q., 1996. The Effect of Climate Warming on the Qinghai-Tibet Highway, China. *Cold Regions Science and Technology* 24, 101–106.
- Van Huissteden, J., Berrittella, C., Parmentier, F., Mi, Y., Maximov, T., Dolman, A., 2011. Methane Emissions From Permafrost Thaw Lakes Limited by Lake Drainage. *Nature Climate Change* 1, 119.
- Vonk, J.E., Tank, S.E., Bowden, W.B., Laurion, I., Vincent, W.F., Alekseychik, P., Amyot, M., Billet, M., Canario, J., Cory, R.M., et al., 2015. Reviews and Syntheses: Effects of Permafrost Thaw on Arctic Aquatic Ecosystems. *Biogeosciences* 12, 7129–7167.
- Wang, B., French, H.M., 1995. In Situ Creep of Frozen Soil, Fenghuo Shan, Tibet Plateau, China. *Canadian Geotechnical Journal* 32, 545–552.
- Wang, H., Liu, H., Ni, W., 2017. Factors Influencing Thermokarst Lake Development in Beiluhe Basin, the Qinghai–Tibet Plateau. *Environmental earth sciences* 76, 816.
- Wold, S., Esbensen, K., Geladi, P., 1987. Principal Component Analysis. *Chemometrics and intelligent laboratory systems* 2, 37–52.
- Wolfe, S., Kotler, E., Dallimore, S., 2001. Surficial Characteristics and the Distribution of Thaw Landforms (1970 to 1999), Shingle Point to Kay Point, Yukon Territory. Geological Survey of Canada, Open File 4088.

- Wu, J.c., Sheng, Y., Yu, H., Li, J.p., 2007. Permafrost in the Middle East Section of Qilian Mountains (I): Distribution of Permafrost. *Journal of Glaciology and Geocryology* 29, 418–425.
- Wu, Q., Hou, Y., Yun, H., Liu, Y., 2015. Changes in Active-Layer Thickness and Near-Surface Permafrost Between 2002 and 2012 in Alpine Ecosystems, Qinghai-Xizang (Tibet) Plateau, China. *Global and Planetary Change* 124, 149–155.
- Wu, Q., Zhang, T., 2008. Recent Permafrost Warming on the Qinghai-Tibetan Plateau. *Journal of Geophysical Research: Atmospheres* 113, 1–22.
- Wu, Q., Zhang, T., 2010. Changes in Active Layer Thickness Over the Qinghai-Tibetan Plateau From 1995 to 2007. *Journal of Geophysical Research: Atmospheres* 115, 1–12.
- Wu, Q., Zhang, T., Liu, Y., 2010. Permafrost Temperatures and Thickness on the Qinghai-Tibet Plateau. *Global and Planetary Change* 72, 32–38.
- Wu, T.F., Lin, C.J., Weng, R.C., 2004. Probability Estimates for Multi-Class Classification by Pairwise Coupling. *Journal of Machine Learning Research* 5, 975–1005.
- Yang, M., Nelson, F.E., Shiklomanov, N.I., Guo, D., Wan, G., 2010. Permafrost Degradation and its Environmental Effects on the Tibetan Plateau: A Review of Recent Research. *Earth-Science Reviews* 103, 31–44.
- Yin, G., Niu, F., Lin, Z., Luo, J., Liu, M., 2017. Effects of Local Factors and Climate on Permafrost Conditions and Distribution in Beiluhe Basin, Qinghai-Tibet Plateau, China. *Science of the Total Environment* 581, 472–485.
- Zeiler, M.D., Fergus, R., 2014. Visualizing and Understanding Convolutional Networks, in: European Conference on Computer Vision, Springer. pp. 818–833.
- Zhang, L., Huang, X., Huang, B., Li, P., 2006. A Pixel Shape Index Coupled With Spectral Information for Classification of High Spatial Resolution Remotely Sensed Imagery. *IEEE Transactions on Geoscience and Remote Sensing* 44, 2950–2961.

- Zhang, T., 2005. Influence of the Seasonal Snow Cover on the Ground Thermal Regime: An Overview. *Reviews of Geophysics* 43, 1–23.
- Zhang, T., Barry, R.G., Knowles, K., Heginbottom, J.A., Brown, J., 1999. Statistics and Characteristics of Permafrost and Ground-Ice Distribution in the Northern Hemisphere 1. *Polar Geography* 23, 132–154.
- Zhang, W., Witharana, C., Liljedahl, A., Kanevskiy, M., 2018. Deep Convolutional Neural Networks for Automated Characterization of Arctic Ice-Wedge Polygons in Very High Spatial Resolution Aerial Imagery. *Remote Sensing* 10, 1487.
- Zhao, L., Wu, Q., Marchenko, S.S., Sharkhuu, N., 2010. Thermal State of Permafrost and Active Layer in Central Asia During the International Polar Year. *Permafrost and Periglacial Processes* 21, 198–207.
- Zhou, Y., Guo, D., Qui, G., Cheng, G., Li, S., 2000. *Geocryology in China*. Science Press, Beijing.
- Zhu, X.X., Tuia, D., Mou, L., Xia, G.S., Zhang, L., Xu, F., Fraundorfer, F., 2017. Deep Learning in Remote Sensing: A Comprehensive Review and List of Resources. *IEEE Geoscience and Remote Sensing Magazine* 5, 8–36.
- Zou, D., Zhao, L., Yu, S., Chen, J., Hu, G., Wu, T., Wu, J., Xie, C., Wu, X., Pang, Q., et al., 2017. A New Map of Permafrost Distribution on the Tibetan Plateau. *The Cryosphere* 11, 2527.
- Zwieback, S., Kokelj, S.V., Günther, F., Boike, J., Grosse, G., Hajnsek, I., 2018. Sub-Seasonal Thaw Slump Mass Wasting Is Not Consistently Energy Limited at the Landscape Scale. *Cryosphere* 12, 549–564.

Appendix A

Supplementary tables for Chapter 4

Table A.1: Accuracies of the mapping results with different data augmentation methods. Options refer to Augmentation Methods. The meaning of each column is described in Table 4.1.

#	Options	AP	Neg	Pos	IOU	TP	FP	FN	Pre	Rec	F1
1	F	0.511	1268	1029	0.8 0.4 0	112 168 170	97 41 39	90 33 2	0.536 0.804 0.813	0.555 0.836 0.988	0.545 0.82 0.892
2	F, B	0.523	1268	1715	0.8 0.4 0	121 169 173	79 31 27	81 32 6	0.605 0.845 0.865	0.599 0.841 0.967	0.602 0.843 0.913
3	C	0.51	1268	1029	0.8 0.4 0	116 164 168	71 23 19	86 36 14	0.62 0.877 0.898	0.574 0.82 0.923	0.596 0.848 0.911
4	S	0.531	1268	1029	0.8 0.4 0	120 171 171	78 27 27	82 29 4	0.606 0.864 0.864	0.594 0.855 0.977	0.6 0.859 0.917
5	R	0.485	1268	1372	0.8 0.4 0	84 144 152	88 28 20	118 57 21	0.488 0.837 0.884	0.416 0.716 0.879	0.449 0.772 0.881
6	F, R	0.519	1268	2058	0.8 0.4 0	108 166 170	90 32 28	94 34 6	0.546 0.838 0.859	0.535 0.83 0.966	0.54 0.834 0.909
7	F, C	0.519	1268	1715	0.8	116	82	86	0.586	0.574	0.58

Continued on next page

Table A.1 – *Continued from previous page*

#	Options	AP	Neg	Pos	IOU	TP	FP	FN	Pre	Rec	F1
					0.4 0	171 173	27 25	28 6	0.864 0.874	0.859 0.967	0.862 0.918
8	F, S	0.51	1268	1715	0.8 0.4 0	113 169 171	88 32 30	89 32 6	0.562 0.841 0.851	0.559 0.841 0.966	0.561 0.841 0.905
9	B	0.493	1268	1029	0.8 0.4 0	107 157 161	76 26 22	95 43 17	0.585 0.858 0.88	0.53 0.785 0.905	0.556 0.82 0.892
10	B, C	0.519	1268	1715	0.8 0.4 0	123 163 167	59 19 15	79 36 15	0.676 0.896 0.918	0.609 0.819 0.918	0.641 0.856 0.918
11	B, S	0.5	1268	1715	0.8 0.4 0	112 164 165	79 27 26	90 35 12	0.586 0.859 0.864	0.555 0.824 0.932	0.57 0.841 0.897
12	B, R	0.5	1268	2058	0.8 0.4 0	99 155 160	86 30 25	103 45 13	0.535 0.838 0.865	0.49 0.775 0.925	0.512 0.805 0.894
13	C, S	0.521	1268	1715	0.8 0.4 0	131 175 176	76 32 31	71 25 5	0.633 0.845 0.85	0.649 0.875 0.972	0.641 0.86 0.907
14	C, R	0.506	1268	2058	0.8 0.4 0	108 164 167	83 27 24	94 36 12	0.565 0.859 0.874	0.535 0.82 0.933	0.55 0.839 0.903
15	S, R	0.512	1268	2058	0.8 0.4 0	111 170 170	93 34 34	91 30 4	0.544 0.833 0.833	0.55 0.85 0.977	0.547 0.842 0.9
16	F, B, C	0.536	1268	2401	0.8 0.4 0	130 172 175	66 24 21	72 27 7	0.663 0.878 0.893	0.644 0.864 0.962	0.653 0.871 0.926
17	F, B, S	0.518	1268	2401	0.8 0.4 0	125 170 172	81 36 34	77 30 4	0.607 0.825 0.835	0.619 0.85 0.977	0.613 0.837 0.901
18	F, B, R	0.509	1268	2744	0.8 0.4 0	113 169 171	86 30 28	89 30 8	0.568 0.849 0.859	0.559 0.849 0.955	0.564 0.849 0.905
19	F, C, S	0.512	1268	2401	0.8 0.4	131 173	84 42	71 27	0.609 0.805	0.649 0.865	0.628 0.834

Continued on next page

Table A.1 – *Continued from previous page*

#	Options	AP	Neg	Pos	IOU	TP	FP	FN	Pre	Rec	F1
					0	173	42	2	0.805	0.989	0.887
20	F, C, R	0.48	1268	2744	0.8 0.4 0	95 153 155	80 22 20	107 46 22	0.543 0.874 0.886	0.47 0.769 0.876	0.504 0.818 0.881
21	F, S, R	0.497	1268	2744	0.8 0.4 0	111 167 170	91 35 32	91 33 9	0.55 0.827 0.842	0.55 0.835 0.95	0.55 0.831 0.892
22	B, C, S	0.514	1268	2401	0.8 0.4 0	122 167 169	71 26 24	80 33 11	0.632 0.865 0.876	0.604 0.835 0.939	0.618 0.85 0.906
23	B, C, R	0.49	1268	2744	0.8 0.4 0	112 163 165	76 25 23	90 37 17	0.596 0.867 0.878	0.555 0.815 0.907	0.574 0.84 0.892
24	B, S, R	0.494	1268	2744	0.8 0.4 0	111 161 164	77 27 24	91 39 15	0.59 0.856 0.872	0.55 0.805 0.916	0.569 0.83 0.894
25	C, S, R	0.511	1268	2744	0.8 0.4 0	112 167 169	77 22 20	90 32 12	0.593 0.884 0.894	0.555 0.839 0.934	0.573 0.861 0.914
26	F, B, C, S	0.512	1268	3087	0.8 0.4 0	125 172 172	80 33 33	77 28 5	0.61 0.839 0.839	0.619 0.86 0.972	0.614 0.849 0.901
27	F, B, C, R	0.499	1268	3430	0.8 0.4 0	122 172 173	86 36 35	80 26 6	0.587 0.827 0.832	0.604 0.869 0.967	0.595 0.847 0.894
28	F, B, S, R	0.501	1268	3430	0.8 0.4 0	118 173 173	96 41 41	84 27 3	0.551 0.808 0.808	0.584 0.865 0.983	0.567 0.836 0.887
29	F, C, S, R	0.511	1268	3430	0.8 0.4 0	117 171 171	86 32 32	85 29 6	0.576 0.842 0.842	0.579 0.855 0.966	0.578 0.849 0.9
30	B, C, S, R	0.501	1268	3430	0.8 0.4 0	119 165 169	72 26 22	83 34 14	0.623 0.864 0.885	0.589 0.829 0.924	0.606 0.846 0.904
31	F, B, C, S, R	0.515	1268	4116	0.8 0.4 0	120 170 171	80 30 29	82 30 7	0.6 0.85 0.855	0.594 0.85 0.961	0.597 0.85 0.905

Table A.2: Accuracies of the mapping results without removing small polygons by applying different data augmentation methods. Options refer to Augmentation Methods. The meaning of each column is described in Table 4.1.

#	Options	AP	Neg	Pos	IOU	TP	FP	FN	Pre	Rec	F1
1	F	0.420	1268	1029	0.8	112	148	90	0.431	0.555	0.485
					0.4	170	90	31	0.654	0.846	0.738
					0	174	86	0	0.669	1.000	0.802
2	F, B	0.454	1268	1715	0.8	121	119	81	0.504	0.599	0.548
					0.4	170	70	31	0.708	0.846	0.771
					0	178	62	2	0.742	0.989	0.848
3	C	0.469	1268	1029	0.8	116	96	86	0.547	0.574	0.560
					0.4	165	47	35	0.778	0.825	0.801
					0	173	39	10	0.816	0.945	0.876
4	S	0.449	1268	1029	0.8	120	124	82	0.492	0.594	0.538
					0.4	174	70	26	0.713	0.870	0.784
					0	176	68	0	0.721	1.000	0.838
5	R	0.434	1268	1372	0.8	84	127	118	0.398	0.416	0.407
					0.4	144	67	57	0.683	0.716	0.699
					0	165	46	13	0.782	0.927	0.848
6	F, R	0.448	1268	2058	0.8	108	131	94	0.452	0.535	0.490
					0.4	168	71	32	0.703	0.840	0.765
					0	175	64	2	0.732	0.989	0.841
7	F, C	0.452	1268	1715	0.8	116	123	86	0.485	0.574	0.526
					0.4	171	68	28	0.716	0.859	0.781
					0	179	60	1	0.749	0.994	0.854
8	F, S	0.416	1268	1715	0.8	113	144	89	0.440	0.559	0.492
					0.4	171	86	30	0.665	0.851	0.747
					0	175	82	2	0.681	0.989	0.807
9	B	0.465	1268	1029	0.8	107	104	95	0.507	0.530	0.518
					0.4	159	52	41	0.754	0.795	0.774
					0	169	42	9	0.801	0.949	0.869
10	B, C	0.458	1268	1715	0.8	123	101	79	0.549	0.609	0.578
					0.4	165	59	34	0.737	0.829	0.780
					0	176	48	7	0.786	0.962	0.865
11	B, S	0.456	1268	1715	0.8	112	115	90	0.493	0.555	0.522
					0.4	164	63	35	0.723	0.824	0.770
					0	173	54	4	0.762	0.977	0.856
12	B, R	0.479	1268	2058	0.8	99	115	103	0.463	0.490	0.476

Continued on next page

Table A.2 – *Continued from previous page*

#	Options	AP	Neg	Pos	IOU	TP	FP	FN	Pre	Rec	F1
					0.4 0	155 170	59 44	45 3	0.724 0.794	0.775 0.983	0.749 0.879
13	C, S	0.443	1268	1715	0.8 0.4 0	131 177 181	122 76 72	71 23 1	0.518 0.700 0.715	0.649 0.885 0.995	0.576 0.782 0.832
14	C, R	0.465	1268	2058	0.8 0.4 0	108 166 176	120 62 52	94 34 3	0.474 0.728 0.772	0.535 0.830 0.983	0.502 0.776 0.865
15	S, R	0.423	1268	2058	0.8 0.4 0	111 172 174	146 85 83	91 28 0	0.432 0.669 0.677	0.550 0.860 1.000	0.484 0.753 0.807
16	F, B, C	0.477	1268	2401	0.8 0.4 0	130 175 181	104 59 53	72 24 1	0.556 0.748 0.774	0.644 0.879 0.995	0.596 0.808 0.870
17	F, B, S	0.424	1268	2401	0.8 0.4 0	125 172 176	137 90 86	77 28 0	0.477 0.657 0.672	0.619 0.860 1.000	0.539 0.745 0.804
18	F, B, R	0.423	1268	2744	0.8 0.4 0	113 170 180	141 84 74	89 29 2	0.445 0.669 0.709	0.559 0.854 0.989	0.496 0.751 0.826
19	F, C, S	0.410	1268	2401	0.8 0.4 0	131 175 176	143 99 98	71 25 0	0.478 0.639 0.642	0.649 0.875 1.000	0.550 0.738 0.782
20	F, C, R	0.441	1268	2744	0.8 0.4 0	95 155 162	111 51 44	107 44 15	0.461 0.752 0.786	0.470 0.779 0.915	0.466 0.765 0.846
21	F, S, R	0.442	1268	2744	0.8 0.4 0	111 168 177	128 71 62	91 32 4	0.464 0.703 0.741	0.550 0.840 0.978	0.503 0.765 0.843
22	B, C, S	0.470	1268	2401	0.8 0.4 0	122 169 175	100 53 47	80 31 6	0.550 0.761 0.788	0.604 0.845 0.967	0.576 0.801 0.869
23	B, C, R	0.462	1268	2744	0.8 0.4 0	112 163 176	108 57 44	90 37 7	0.509 0.741 0.800	0.555 0.815 0.962	0.531 0.776 0.873
24	B, S, R	0.460	1268	2744	0.8 0.4	111 162	104 53	91 38	0.516 0.754	0.550 0.810	0.532 0.781

Continued on next page

Table A.2 – *Continued from previous page*

#	Options	AP	Neg	Pos	IOU	TP	FP	FN	Pre	Rec	F1
					0	170	45	9	0.791	0.950	0.863
25	C, S, R	0.475	1268	2744	0.8 0.4 0	112 167 175	102 47 39	90 32 7	0.523 0.780 0.818	0.555 0.839 0.962	0.539 0.809 0.884
26	F, B, C, S	0.437	1268	3087	0.8 0.4 0	125 173 176	125 77 74	77 27 1	0.500 0.692 0.704	0.619 0.865 0.994	0.553 0.769 0.824
27	F, B, C, R	0.430	1268	3430	0.8 0.4 0	122 173 180	134 83 76	80 25 0	0.477 0.676 0.703	0.604 0.874 1.000	0.533 0.762 0.826
28	F, B, S, R	0.403	1268	3430	0.8 0.4 0	118 174 176	156 100 98	84 26 0	0.431 0.635 0.642	0.584 0.870 1.000	0.496 0.734 0.782
29	F, C, S, R	0.451	1268	3430	0.8 0.4 0	117 174 178	127 70 66	85 26 0	0.480 0.713 0.730	0.579 0.870 1.000	0.525 0.784 0.844
30	B, C, S, R	0.471	1268	3430	0.8 0.4 0	119 166 180	101 54 40	83 33 6	0.541 0.755 0.818	0.589 0.834 0.968	0.564 0.792 0.887
31	F, B, C, S, R	0.457	1268	4116	0.8 0.4 0	120 170 176	117 67 61	82 30 2	0.506 0.717 0.743	0.594 0.850 0.989	0.547 0.778 0.848

□ End of chapter.

Appendix B

Glossary of abbreviations

a.s.l.: Above sea level

ALD: Active layer detachment

AP: Average precision

AWS: Amazon web services

CNN: Convolutional neural networks

DEM: Digital elevation model

DOM: Digital orthophoto map

DSM: Digital surface model

FN: False negative

FP: False positive

GCP: Ground control point

GDAL: Geospatial data abstraction library

GEOBIA: Geographic object-based image analysis

GPS: Global positioning system

GPU: Graphics processing unit

GRASS: Geographic resources analysis support system

ha: Hectare

IOU: Intersection over union

MODIS: Moderate resolution imaging spectroradiometer

NDVI: Normalized difference vegetation index

NDWI: Normalized difference water index
OLS: Ordinary least squares regression
PCA: Principal component analysis
PISR: Potential incoming solar radiation
PSI: Pixel shape index
RGB: Red, blue, and green
RTK: Real-time kinematic
RTS: Retrogressive thaw slump
SAGA: System for automated geoscientific analyses
SFS: Structural feature set
SPOT: Satellite pour l'observation de la terre
SRTM: Shuttle radar topographic mission
SVC: Support vector classification
SVM: Support vector machine
TP: True positive
TPI: Topographic position index
UAV: Unmanned aerial vehicle

End of chapter.